Local Correlation Approaches and Coupled Cluster Linear Response Theory

Harley R. McAlexander

Dissertation submitted to the Faculty of the

Virginia Polytechnic Institute and State University

in partial fulfillment of the requirements for the degree of

Doctor of Philosophy

in

Chemistry

T. Daniel Crawford, Chair

John Morris

Diego Troya

Eduard Valeyev

April 30, 2015

Blacksburg, Virginia

Keywords: Coupled Cluster, Local Correlation, Response Properties

Local Correlation Approaches and Coupled Cluster Linear Response Theory

Harley R. McAlexander

(ABSTRACT)

Quantum mechanical methods are becoming increasingly useful and applicable tools to complement and support experiment. Nonetheless, some barriers to further applications of theoretical models still remain. A coupled cluster singles and doubles (CCSD) calculation, a reliable *ab initio* method, scales approximately on the order of $\mathcal{O}(N^6)$, where N is a measure of the system size. This unfortunately limits the use of such high-accuracy methods to relatively small systems.

Coupled cluster property calculations must be used in conjunction with reduced-scaling methods in order to broaden the range of applications to larger systems. In this work, we introduce some of the underlying theory behind such calculations and test the performance of several local correlation techniques for polarizabilities, optical rotations, and excited state

properties. In general, when the computational cost is significantly reduced, the necessary accuracy is lost. Polarizabilities are less sensitive to the truncation schemes than optical rotations, and the excitation data is often only in agreement with the canonical result for the first few excited states.

Additionally, we present a novel application of equation-of-motion coupled cluster singles and doubles to simulated circularly polarized luminescence spectra of eight chiral ketones. Both the absorption in the ground state and emission from the excited states were examined. Extensive geometry analyses were performed, revealing that optimized structures at the density functional theory were adequate for the calculation accurate coupled cluster excitation data.

This work was supported by grants from the U.S. National Science Foundation: CHE-0715185, CHE1058420, ACI-1147794; and a Multi-User Chemistry Research Instrumentation and Facility (CRIF-MU) award: CHE-0741927.

Acknowledgments

Several people deserve, at the very least, some recognition for helping me on my way down the path of life and graduate school. To name them all would take too long, unfortunately, but I would like to acknowledge the following:

- Charles and Kathie McAlexander for sticking with me always, even when I move far away.
- Max, Jack, and Sam - a faithful trio of friends for whom I am grateful and because of whom I am a better person.
- David Magers for introducing me to this particular niche of chemistry, and helping me make it to graduate school.
- Taylor (and Mandy) Mach, without whom my time at Virginia Tech would have been much less fufilling and interesting.
- Ashutosh Kumar for returning to VT after a summer internship and becoming an excellent collegue always up for a discussion.

- Other colleagues and friends in the theoretical chemistry groups including: Florian Bischoff, Rob Chapleski, Ryan Fortenberry, Drew Lewis, Fabijan Pavosevic, and Ben Pritchard, for contributing to a fun, productive environment and encouraging further educational ventures.

- Ms. Joli Huynh for keeping me on track to fulfill all my graduation requirements.

- Visiting summer students: Vibin Abraham, Ayush Asthana, Ayan Chatterjee, and Ruhee D'cunha, for giving me the chance to work with them, and from whom I gained much in return.

- Prof. T. Daniel Crawford for taking me on as a graduate student, investing his time and effort to further my graduate career, and not being afraid to share a chemistry pun. Only with his help has this work been possible.

Attribution

The work for Chapter 3 took place in 2011, and was published in 2012. The calculations and data collection and analysis were performed by myself. Further more, I implemented changes in the code for extending orbital domains by nearest-neighbors atoms. Taylor J. Mach wrote the necessary programming for the orbital optimized coupled cluster (OO-CCD) calculations in addition to serving as a mentor for the project.

Contents

List of Figures

List of Tables

Chapter 1

Introduction

Chiral molecules possess a handedness such that the system may not be superposed upon its mirror image. A molecule may have a chiral center, such as bromo-chloro-fluoro-methane, or exhibit a helical asymmetry resulting in axial chirality, as seen in dimethylallene (2,3-pentadiene). The different hands or enantiomers of a compound — while having identical mass, density, etc — can have tremendously different effects in chiral environments such as the human body. For instance, the drug thalidomide was originally prescribed as a sedative for pregnant women, but it was discovered its two enantiomeric forms have vastly different effects. The R enantiomer indeed functions as a sedative, while its S counterpart has been shown to cause birth defects; and further complications arise as, even in the case that only the R form is administered, the drug racemizes quickly in the body so that both enantiomers are still present.[1]

Figure 1.1: Chirality examples: (a) (*S*)-bromo-chloro-fluoro-methane and (b) (*P*)-dimethylallene.

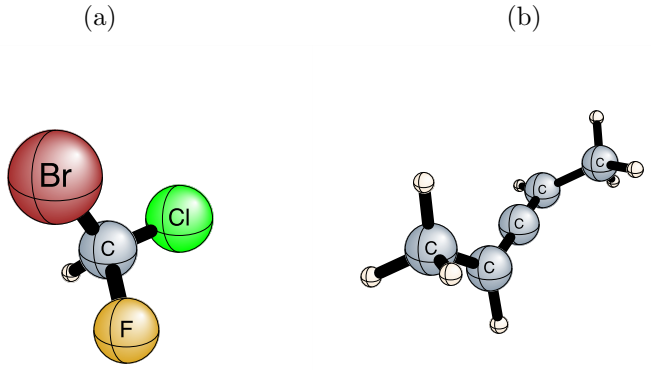

Fortunately, certain properties such as optical rotation and circular dichroism allow for the enantiomers of a compound to be distinguished through their differential interaction (refraction, absorption, emission, and scattering) with left- and right-hand circularly polarized light. In optical rotation, for instance, each enantiomer rotates plane polarized light, which can be thought of as an even combination of left and right circularly polarized light, by the same amount but in opposite directions due to different indices of refraction for the left and right-hand components. However, while the two stereoisomers may be distinguished via such experiments, assigning the correct enantiomer to the appropriate sign of the property must be determined separately. Unfortunately, the experimental determination of absolute configurations can be exceedingly difficult, often involving lengthy and challenging syntheses. Several theoretical models and approaches, however, are available for aiding in the prediction of chiroptical properties.[2–7]

A renewed interest in computational studies of chiroptical properties was sparked by the

work of Polavarapu[2] in which he applied time-dependent Hartree-Fock (TDHF) theory to the prediction of optical rotations. His initial results appeared promising - for all test cases the predicted sign of the optical rotation matched that of experiment. While providing support for further computational studies of chiroptical properties, several challenges still presented themselves. For instance, most optical rotations are measured in solution, whereas a calculation on a single molecule, as in Polavarapu's work, more closely simulates gas-phase optical rotations. Furthermore, more advanced methods needed to be tested for chiroptical properties.

Density functional theory (DFT) also offers a relatively inexpensive approach, but incorporates correlation effects unlike TDHF.[3,4] In a 2000 study, Cheeseman and co-workers studied basis set dependence of optical rotation along with origin dependence in both the electric-dipole, magnetic-dipole polarizability tensor and optical rotation values using DFT. Optical rotation calculations had typically been performed with field-independent atomic orbitals (FIAOs), which only make the electric-dipole, magnetic-dipole polarizability tensor origin independent in the complete basis set limit. Cheeseman and co-workers showed that using gauge-including atomic orbitals (GIAOs), also known as London orbitals, ensures origin independence in the tensor, and thus in the optical rotation as well, for HF and DFT calculations.

In their 1990 paper, Koch and Jørgensen helped open the door for the use of CC theory for chiroptical properties, laying forth both linear and quadratic response functions.[8] Following up on this work, Kobayashi et al. applied coupled-cluster singles and doubles linear

response (CCSDLR) to produce frequency dependent polarizabilities.[9] Ruud and co-workers took the next step, extending the coupled cluster linear response (CCLR) method for calculating optical rotations,[5] and they offered comparisons between HF, DFT, and CCLR with experimental values in a following study.[6]

Other properties beside optical rotation have been similarly examined via theoretical predictions.[10] The CCLR formalism[8,11] makes accessible the *ab initio* calculation of optical properties such as optical rotation and circular dichroism, as mentioned above, and also Raman optical activity and circularly polarized luminescence.[10,12] The methodology serves as an excellent tool for elucidating the absolute configuration of chiral compounds and making connections between structure and chirality.

Despite its relative success and potential for further application, however, CCLR methods suffer from key challenges: origin dependence of the property tensor, incorporating solvent effects for comparison to experiment, and the high-degree polynomial scaling of CC methods. The origin dependence is a consequence of the non-variational nature of the coupled cluster wavefunction. Unlike HF and DFT methods, properties such as optical rotation computed via CCLR are not origin independent even at the complete basis set limit, and the dependence cannot be resolved using GIAOs.[6] The modified velocity gauge formalism for the electric dipole operator has been developed to help address this issue. The velocity-gauge formalism, $\langle\langle \vec{\mathbf{p}}, \vec{\mathbf{L}} \rangle\rangle_\omega$, allows for the trace of the property tensor to be origin invariant. Here $\vec{\mathbf{p}}$ and $\vec{\mathbf{L}}$ are the electronic momentum and angular momentum operators, respectively, and $\langle\langle , \rangle\rangle_\omega$ represents the response function evaluated at frequency ω. However, without a complete basis

set, using the velocity gauge formalism results in unphysical behavior at zero frequency. To achieve the appropriate behavior, the value for the velocity gauge representation at the static limit (at zero frequency) is subtracted from the original expression, as shown in Equation 1.1.[13]

$$\langle\langle \vec{\mathbf{p}}, \vec{\mathbf{L}} \rangle\rangle_\omega \rightarrow \langle\langle \vec{\mathbf{p}}, \vec{\mathbf{L}} \rangle\rangle_\omega - \langle\langle \vec{\mathbf{p}}, \vec{\mathbf{L}} \rangle\rangle_0 \tag{1.1}$$

Alternatively, the underlying response theory can be reformulated to incorporate orbital rotation parameters explicitly to achieve origin invariance.[14,15]

For comparing theoretical results directly to experimental data, it is often necessary and desirable to take into account the influence that the solvent may have on the property of the system of interest, as many measurements are made in solution. Furthermore, solvents can have a powerful influence on molecular properties like optical rotation.[16] One method to tackle this problem has been to simulate the effect of the solvent with some sort of potential or force field, such as continuum solvation models.[17] Other techniques follow a more explicit approach by including solvent molecules in the calculation, but this can be further complicated by requiring large numbers of solvent molecules which greatly increases the cost of the calculation and by the need to average over several configurations.

Lastly, many compounds of interest are too large to be approached with coupled cluster methods.[18–24] In order to expand the scope of CCLR to larger systems — to approach the biochemical regime or to perform explicit solvation simulations with several solvent molecules — additional approximations and methods must be introduced. Numerous reduced-scaling

techniques have extended the range of molecules that may be treated at the coupled cluster level,[25–53] but their application to coupled cluster properties such as those mentioned above has been relatively limited.[54–60] In the following chapters, much focus is given to the performance of three of these approaches — the projected atomic orbitals (PAO),[25,61–63] pair natural orbitals (PNO),[43,44] and orbital specific virtuals (OSV)[49,50] — to molecular response properties.

The main focus of this work is applying local correlation techniques in the context of coupled cluster properties, assessing the computational savings and the error introduced as a result of the enforced truncation. Also, a project is featured that serves as an example where a robust reduced-scaling approach would be highly advantageous for extending the scope to larger systems. Chapter 2 introduces the CCLR formalism, and the essential equations are derived. Next, in Chapter 3, results are presented for the PAO local correlation technique applied to an orbital-optimized coupled cluster method. In addition to the PAO method, the PNO and OSV local approaches are tested for coupled cluster polarizabilities and rotations in Chapter 4. Using the equation-of-motion coupled-cluster (EOM-CC) method in Chapter 5, the same local techniques are applied to excitation data, including rotational and dipole transition strengths. In Chapter 6, the first circularly polarized luminescence data at the EOM-CC singles and doubles (EOM-CCSD) level are discussed. Finally, a brief summary and concluding remarks are given in Chapter 7.

Chapter 2

Coupled Cluster Linear Response Theory

Coupled cluster linear response theory[8,11] is a powerful model for computing optical properties of molecules. For chiral molecules, *ab initio* calculations of properties such as electronic circular dichroism, circularly polarized luminescence, optical rotation, and Raman optical activity are highly useful tools for elucidating the absolute configurations of chiral molecules.[10] In this chapter, we derive the basic working equations for coupled cluster linear response. To begin, we discuss briefly the underlying essential theory for the coupled cluster method. Next we solve the time-dependent Schrödinger equation and apply perturbation theory. Finally, we obtain expressions for the linear response function and make use of the Fourier transformation.

2.1 Coupled Cluster Fundamentals

In coupled cluster theory, a correlated wavefunction is generated from a reference determinant via an exponential ansatz.[64] Most often, the Hartree-Fock ground state is chosen as the reference, and the coupled cluster wavefunction takes the form

$$|\psi_{cc}\rangle = e^{T}|0\rangle, \tag{2.1}$$

where $|0\rangle$ is the reference state and T is the cluster excitation operator. The T operator,

$$T = \sum_{\mu} t_{\mu}\tau_{\mu} \tag{2.2}$$

when acting on the reference, generates a substituted determinant $|\mu\rangle$ via the excitation operator τ_{μ}, with an associated coefficient or amplitude, t_{μ}, and the sum over μ includes all single, double, triple and higher substitutions.

Inserting the coupled cluster wavefunction into the Schrödinger equation and left projecting by the reference gives the coupled cluster energy,

$$\langle 0|H|\psi_{cc}\rangle = E_{cc}\langle 0|\psi_{cc}\rangle \tag{2.3}$$

$$= E_{cc}, \tag{2.4}$$

where intermediate normalization has been assumed. The Hamiltonian may be similarity

transformed with the T operator, leaving the energy unchanged, as shown in Equations 2.5-2.8,

$$\langle 0|e^{-T}H|\psi_{cc}\rangle = \langle 0|e^{-T}He^{T}|0\rangle \tag{2.5}$$

$$= E_{cc}\langle 0|e^{-T}e^{T}|0\rangle \tag{2.6}$$

$$= E_{cc}\langle 0|0\rangle \tag{2.7}$$

$$= E_{cc}. \tag{2.8}$$

In order to arrive at expressions for the amplitudes, left-projecting with substituted determinants yields the defining equations

$$\langle \mu|e^{-T}He^{T}|0\rangle = \langle \mu|\bar{H}|0\rangle = 0, \tag{2.9}$$

where $\bar{H}$ is the similarity-transformed Hamiltonian.

However, the similarity-transformed Hamiltonian is not Hermitian, meaning the left-hand coupled cluster wavefunction is not the simple complex conjugate of the right-hand counterpart. The so-called lambda equations for the left-hand wavefunction arise naturally in analytic gradient theory.[65,66] The lambda amplitudes can also be considered the Lagrangian multipliers in a variational formulation of the coupled cluster wavefunction.[67]

The left-hand coupled cluster wavefunction is

$$\langle\tilde{\psi}_{cc}| = \langle 0| \left(1 + \Lambda\right) e^{-T}, \tag{2.10}$$

where the Λs are de-excitation cluster operators of the form

$$\Lambda = \sum_{\mu} \lambda_{\mu} \tau_{\mu}^{\dagger}. \tag{2.11}$$

To solve for the lambda amplitudes, the defining expressions involve projecting on the right by a substituted determinant

$$\langle 0| \left(1 + \Lambda\right) \left(\bar{H} - E_{cc}\right) |\mu\rangle = 0. \tag{2.12}$$

2.2 Time-Dependent Schrödinger Equation and Coupled Cluster Theory

In response theory, we are interested in the expectation value of a time-independent operator subject to a time-dependent perturbation. As a starting point, let us consider the time-dependent Schrödinger equations, shown in Equations 2.13-2.14.

$$\langle\Psi|H_t = -i\frac{d}{dt}\langle\Psi| \tag{2.13}$$

$$H_t|\Psi\rangle = i\frac{d}{dt}|\Psi\rangle \tag{2.14}$$

In the context of coupled cluster, we have

$$\langle\tilde{\psi}_{cc}(t)|H_t = -i\frac{d}{dt}\langle 0|(1+\Lambda(t))e^{-T(t)}e^{-i\epsilon(t)} \tag{2.15}$$

$$H_t|\psi_{cc}(t)\rangle = i\frac{d}{dt}e^{i\epsilon(t)}e^{T(t)}|0\rangle, \tag{2.16}$$

where it is clear we have distinct left and right-hand wavefunctions. Focusing on the right-hand equation, we get two terms — one involving the time-derivative of the T operator and the other the time-derivative of the phase factor $\epsilon(t)$ — shown in Equation 2.17,

$$H_t e^{i\epsilon(t)}e^{T(t)}|0\rangle = -e^{T(t)}|0\rangle e^{i\epsilon(t)}\frac{d\epsilon(t)}{t} + ie^{T(t)}\frac{dT(t)}{dt}|0\rangle e^{i\epsilon(t)} \tag{2.17}$$

and we are implicitly keeping the molecular orbitals fixed. We can eliminate the $e^{i\epsilon(t)}$ by multiplying each term by the inverse $e^{-i\epsilon(t)}$. A final simplification may be made by multiplying on the left by $e^{-T(t)}$. In Equations 2.18 - 2.19, we've introduced the notation $\overline{\overline{H_t}}$, which represents the time-dependent Hamiltonian similarity transformed with time-dependent cluster operators.

$$e^{-T(t)}H_t e^{T(t)}|0\rangle = \overline{\overline{H_t}}|0\rangle = ie^{-T(t)}e^{T(t)}\frac{dT(t)}{dt}|0\rangle - e^{-T(t)}e^{T(t)}|0\rangle\frac{d\epsilon(t)}{t} \tag{2.18}$$

$$\overline{\overline{H_t}}|0\rangle = i\frac{dT(t)}{dt}|0\rangle - |0\rangle\frac{d\epsilon(t)}{dt} \tag{2.19}$$

Projection on the left with the reference determinant gives us an expression for $\frac{d\epsilon(t)}{dt}$.

$$\langle 0|\overline{\overline{H_t}}|0\rangle = i\langle 0|\frac{dT(t)}{dt}|0\rangle - \langle 0|0\rangle\frac{d\epsilon(t)}{dt} \tag{2.20}$$

$$= -\frac{d\epsilon(t)}{dt} \tag{2.21}$$

We eliminate the first term on the right-hand side of Equation 2.20 by taking advantage of the fact that the derivative of the T operator is still an excitation operator

$$\frac{dT(t)}{dt} = \sum_{\mu}\frac{dt_\mu(t)}{dt}\tau_\mu, \tag{2.22}$$

creating a substituted determinant whose overlap with the reference state is zero.

2.2.1 Time-Dependent Amplitude Expressions

When we left-project with a substituted determinant, on the other hand, we arrive at the expression for $\frac{dt_\mu(t)}{dt}$

$$\langle \mu|\overline{\overline{H_t}}|0\rangle = i\langle \mu|\frac{dT(t)}{dt}|0\rangle - \langle \mu|0\rangle\frac{d\epsilon(t)}{dt} \tag{2.23}$$

$$= i\sum_{\nu}\frac{t_\nu(t)}{dt}\langle \mu|\nu\rangle \tag{2.24}$$

$$= i\sum_{\nu}\frac{t_\nu(t)}{dt}\delta_{\mu\nu} \tag{2.25}$$

$$= i\frac{t_\mu(t)}{dt}. \tag{2.26}$$

The second term in Equation 2.23 is zero for reasons discussed in Equations 2.20 - 2.21. Similarly the substituted determinants are orthogonal to each other, so that the only surviving term from the summation in Equation 2.24 is where $\nu = \mu$, as indicated by the Kronecker delta ($\delta_{\mu\nu}$) in Equation 2.25.

The evaluation of the left-hand Schrödinger equation is slightly more involved due to the appearance of three time-dependent quantities. Following similar simplification strategies as for the right-hand case, we have

$$\begin{aligned}\langle 0|(1+\Lambda(t))e^{-T(t)}H_t = &- i\langle 0|\frac{d\Lambda(t)}{dt}e^{-T(t)} + i\langle 0|(1+\Lambda(t))\frac{dT(t)}{dt}e^{-T(t)} \\ &- \langle 0|(1+\Lambda(t))e^{-T(t)}\frac{d\epsilon(t)}{dt}. \end{aligned} \tag{2.27}$$

Finally, introducing the similarity transformation again, our expression is

$$\langle 0|(1+\Lambda(t))\overline{\overline{H_t}} = -i\langle 0|\frac{d\Lambda(t)}{dt} + i\langle 0|(1+\Lambda(t))\frac{dT(t)}{dt} - \langle 0|(1+\Lambda(t))\frac{d\epsilon(t)}{dt}. \tag{2.28}$$

In order to arrive at a general expression for the $\frac{d\lambda_\mu(t)}{dt}$, we right-project by a substituted determinant

$$\begin{aligned}\langle 0|\left(1+\Lambda(t)\right)\overline{\overline{H_t}}|\mu\rangle = &- i\langle 0|\frac{d\Lambda(t)}{dt}|\mu\rangle + i\langle 0|\left(1+\Lambda(t)\right)\frac{dT(t)}{dt}|\mu\rangle \\ &- \frac{d\epsilon(t)}{dt}\langle 0|\left(1+\Lambda(t)\right)|\mu\rangle. \end{aligned} \tag{2.29}$$

In the third term of Equation 2.29, we can substitute $\langle 0|\overline{\overline{H_t}}|0\rangle$ for $-\frac{d\epsilon(t)}{dt}$ using Equation

2.21. After careful use of the resolution of the identity along with the introduction of a commutator, we ultimately get the much more compact expression

$$-i\frac{d\lambda_\mu(t)}{dt} = \langle 0|\left(1+\Lambda(t)\right)\left[\overline{\overline{H_t}},\tau_\mu\right]|0\rangle. \tag{2.30}$$

2.2.2 Partitioning H_t and Perturbation Expansions

With the expressions for time-dependent amplitudes in hand, we expand each equation in orders of perturbation. First, we partition the Hamiltonian into the time-independent Hamiltonian and a time-dependent perturbation, as shown in Equation 2.31.

$$H_t = H + V(t) \tag{2.31}$$

With this partition in mind, let us revisit $\overline{\overline{H_t}}$, where we also expand the cluster operators in orders of perturbations as well.

$$\overline{\overline{H_t}} = e^{-T^{(0)}}e^{-T^{(1)}(t)}e^{-T^{(2)}(t)}\ldots(H+V(t))e^{T^{(0)}}e^{T^{(1)}(t)}e^{T^{(2)}(t)}\ldots \tag{2.32}$$

$$= e^{-T^{(1)}(t)}e^{-T^{(2)}(t)}\ldots(\bar{H}+\bar{V}(t))e^{T^{(1)}(t)}e^{T^{(2)}(t)}\ldots \tag{2.33}$$

$$= \bar{H}+\bar{V}(t)+\left[\bar{H},T^{(1)}(t)\right]+\left[\bar{V}(t),T^{(1)}(t)\right]+\frac{1}{2}\left[\left[\bar{H},T^{(1)}(t)\right],T^{(1)}(t)\right]+\ldots \tag{2.34}$$

In Equations 2.33-2.34, a single overbar denotes similarity transformation with the zeroth order T operators. Finally, $\overline{\overline{H_t}}$ may be written as a series of commutators using the Baker-

Campbell-Hausdorf expansion,[68] which helps somewhat in collecting terms by order. Returning to Equation 2.26, we can easily identify the zeroth and first order $\frac{dt_\mu(t)}{dt}$ equations, shown in Equations 2.35 and 2.37, respectively.

$$\frac{dt_\mu^{(0)}}{dt} = -i\langle\mu|\bar{H}|0\rangle \tag{2.35}$$

$$\frac{dt_\mu^{(1)}(t)}{dt} = -i\langle\mu|\bar{V}(t)|0\rangle - i\langle\mu|\left[\bar{H}, T^{(1)}(t)\right]|0\rangle \tag{2.36}$$

$$= -i\langle\mu|\bar{V}(t)|0\rangle - i\sum_\nu t_\nu^{(1)}(t)\langle\mu|\left[\bar{H}, \tau_\nu\right]|0\rangle \tag{2.37}$$

However, the $t_\mu^{(0)}$ are the ground state amplitudes, and are independent of time; using Equation 2.9, we can see that Equation 2.35 is also equal to 0. Starting from similar perturbation expansions, an analogous expression for the first order left-hand time-derivative is derived:

$$-i\frac{d\lambda_\mu^{(1)}(t)}{dt} = \langle 0|\Lambda^{(1)}(t)\left[\bar{H}, \tau_\mu\right]|0\rangle + \langle 0|\left(1+\Lambda^{(0)}\right)\left[\bar{V}(t), \tau_\mu\right]|0\rangle + \langle 0|\left(1+\Lambda^{(0)}\right)\left[\left[\bar{H}, \tau_\mu\right], T^{(1)}(t)\right]|0\rangle. \tag{2.38}$$

2.3 Response Formalism

2.3.1 Linear Response

Now that we have working expressions involving first-order, time-dependent amplitudes, let us derive the linear response function. To generate response functions, we take the time-dependent expectation value of a time-independent operator, and expand in orders of perturbation. The general form for operator A is shown in Equation 2.39 for the coupled cluster wavefunction.

$$\langle\tilde{\psi}_{cc}(t)|A|\psi_{cc}(t)\rangle = \langle\tilde{\psi}_{cc}(t)|A|\psi_{cc}(t)\rangle^{(0)} + \langle\tilde{\psi}_{cc}(t)|A|\psi_{cc}(t)\rangle^{(1)} + \langle\tilde{\psi}_{cc}(t)|A|\psi_{cc}(t)\rangle^{(2)} + \ldots \tag{2.39}$$

In the notation of response theory, we have instead

$$\langle\tilde{\psi}_{cc}(t)|A|\psi_{cc}(t)\rangle = \langle\tilde{\psi}_{cc}(t)|A|\psi_{cc}(t)\rangle^{(0)} + \langle\langle A;V(t)\rangle\rangle + \langle\langle A;V(t);V(t)\rangle\rangle + \ldots. \tag{2.40}$$

The zeroth order component involves the usual ground state coupled cluster amplitudes,

$$\langle\tilde{\psi}_{cc}(t)|A|\psi_{cc}(t)\rangle^{(0)} = \langle 0|\left(1+\Lambda^{(0)}\right)e^{-T^{(0)}}Ae^{T^{(0)}}|0\rangle \tag{2.41}$$

$$= \langle 0|\left(1+\Lambda^{(0)}\right)\bar{A}|0\rangle, \tag{2.42}$$

where $\bar{A}$ indicates similarity transformation with $T^{(0)}$. The first order term, $\langle\langle A; V(t)\rangle\rangle$, is the linear response function. Inserting the definitions for the coupled cluster wavefunctions, Equations 2.1 and 2.10, and identifying the appropriate order components yields

$$\langle\langle A; V(t)\rangle\rangle = \langle\tilde{\psi}_{cc}(t)|A|\psi_{cc}(t)\rangle^{(1)} \tag{2.43}$$

$$= \langle 0|\Lambda^{(1)}(t)\bar{A}|0\rangle + \langle 0|\left(1+\Lambda^{(0)}\right)\left[\bar{A}, T^{(1)}(t)\right]|0\rangle \tag{2.44}$$

$$= \sum_{\mu}\lambda_{\mu}^{(1)}(t)\langle\mu|\bar{A}|0\rangle + \sum_{\mu} t_{\mu}^{(1)}(t)\langle 0|\left(1+\Lambda^{(0)}\right)\left[\bar{A}, \tau_{\mu}\right]|0\rangle \tag{2.45}$$

where in Equation 2.45 we have inserted the definitions of the T and Λ operators (Equations 2.2 and 2.11, respectively) to clearly indicate the time-dependent amplitudes.

2.3.2 Fourier Transformation

We are often interested in calculating a property at a particular frequency, in accordance with laboratory experiments. For the time-dependent terms, we may insert a Fourier-transformed equivalent to yield a frequency-dependent expression instead. Equations 2.46-2.47 show the form of the Fourier transformation for the first-order, time-dependent amplitudes and the perturbation operator.

$$t_{\mu}^{(1)}(t) = \int_{-\infty}^{\infty} d\omega X_{\mu}^{(1)}(\omega)e^{-i\omega t} \tag{2.46}$$

$$\lambda_{\mu}^{(1)}(t) = \int_{-\infty}^{\infty} d\omega Y_{\mu}^{(1)}(\omega)e^{-i\omega t} \tag{2.47}$$

$$\bar{V}(t) = \int_{-\infty}^{\infty} d\omega \bar{V}(\omega) e^{-i\omega t} \tag{2.48}$$

After inserting the Fourier transforms, the expression may be simplified by equating the integrands on both sides of the equation and dividing out the $e^{-i\omega t}$. The resulting frequency-dependent linear response function becomes

$$\langle\langle A; \bar{V}(\omega)\rangle\rangle = \sum_{\mu} Y_{\mu}^{(1)}(\omega)\langle\mu|\bar{A}|0\rangle + \sum_{\mu} X_{\mu}^{(1)}(\omega)\langle 0|\left(1+\Lambda^{(0)}\right)\left[\bar{A}, \tau_{\mu}\right]|0\rangle. \tag{2.49}$$

2.3.3 Frequency-Dependent Perturbed Amplitudes: Governing Equations

To solve for the perturbed amplitudes, $X_{\mu}^{(1)}(\omega)$ and $Y_{\mu}^{(1)}(\omega)$, we must also use the Fourier transformation in the defining equation for $\frac{dt_{\mu}^{(1)}(t)}{dt}$ (Equation 2.37) and $\frac{d\lambda_{\mu}^{(1)}(t)}{dt}$ (Equation 2.38). The only new Fourier transformations required involve the first-order derivatives terms. The end result, however, is an additional factor of $-i\omega$ as seen in Equation 2.50.

$$\frac{dt_{\mu}^{(1)}(t)}{dt} = -i\omega \int_{-\infty}^{\infty} d\omega X_{\mu}^{(1)}(\omega) e^{-i\omega t} \tag{2.50}$$

After eliminating the integrands and $e^{-i\omega t}$, the Fourier transformed version of Equation 2.37 is

$$\omega X_\mu^{(1)}(\omega) = \langle\mu|\bar{V}(\omega)|0\rangle + \sum_\nu X_\nu^{(1)}(\omega)\langle\mu|\left[\bar{H},\tau_\nu\right]|0\rangle. \tag{2.51}$$

Expanding the commutator in the second term and inserting the resolution of the identity gives

$$\omega X_\mu^{(1)}(\omega) = \langle\mu|\bar{V}(\omega)|0\rangle + \sum_\nu X_\nu^{(1)}(\omega)\langle\mu|\bar{H}|\nu\rangle - X_\mu^{(1)}(\omega)E_{cc} \tag{2.52}$$

$$(\omega + E_{cc})X_\mu^{(1)}(\omega) = \langle\mu|\bar{V}(\omega)|0\rangle + \sum_\nu X_\nu^{(1)}(\omega)\langle\mu|\bar{H}|\nu\rangle. \tag{2.53}$$

Furthermore, we can collect all terms involving $X_\mu^{(1)}(\omega)$ to one side

$$\sum_\nu \langle\mu|(\bar{H} - E_{cc} - \omega|\nu\rangle X_\mu^{(1)}(\omega) = -\langle\mu|\bar{V}(\omega)|0\rangle \tag{2.54}$$

leaving us with a simplified, convenient right-hand perturbed amplitudes expression. Similarly, for the left-hand perturbed amplitudes, the frequency-dependent equation is

$$-\sum_\mu Y_\mu^{(1)}(\omega)\langle\mu|(\bar{H} - E_{cc} + \omega)|\nu\rangle = \langle 0|\left(1 + \Lambda^{(0)}\right)[\bar{V}(\omega),\tau_\nu]|0\rangle + \sum_\mu F_{\nu\mu}X_\mu^{(1)}(\omega) \tag{2.55}$$

where $F_{\nu\mu}$ is defined as

$$F_{\nu\mu} = \langle 0|\left(1 + \Lambda^{(0)}\right)\left[[\bar{H},\tau_\nu],\tau_\mu\right]|0\rangle. \tag{2.56}$$

2.3.4 Final Simplifications

In terms of implementation, two sets of equations must be coded for the linear-response function in its current form. However, we can make a final simplification such that the response function is expressed in terms of the right-hand perturbed amplitudes only. To begin, we rewrite the defining equation for $X_\mu^{(1)}(\omega)$ (Equation 2.54), but change the sign of the frequency. For general operator A, the expression becomes

$$\langle \mu|\bar{A}|0\rangle = -\sum_\nu X_\nu^A(-\omega)\langle \mu|(\bar{H} - E_{cc} + \omega)|\nu\rangle \tag{2.57}$$

where the superscript A implies that the perturbed amplitude is computed for that particular operator. We can directly substitute Equation 2.57 into the first term of the linear response function (Equation 2.49) to get

$$\langle\langle A; V(\omega)\rangle\rangle = \sum_\mu Y_\mu^{(1)}(\omega)\langle \mu|\bar{A}|0\rangle + \sum_\mu X_\mu^{(1)}(\omega)\langle 0|(1+\Lambda^{(0)})[\bar{A},\tau_\mu]|0\rangle \tag{2.58}$$

$$= -\sum_\nu \sum_\mu Y_\mu^{(1)}(\omega)\langle \mu|(\bar{H} - E_{cc} + \omega)|\nu\rangle X_\nu^A(-\omega) + \sum_\mu X_\mu^{(1)}(\omega)\langle 0|(1+\Lambda^{(0)})[\bar{A},\tau_\mu]|0\rangle. \tag{2.59}$$

Now, we can replace $\sum_\mu Y_\mu^{(1)}(\omega)\langle\mu|(\bar{H} - E_{cc} + \omega)|\nu\rangle$ with the right-hand side of Equation 2.55

$$\langle\langle\bar{A}; V(\omega)\rangle\rangle = -\sum_\mu \Big(\langle 0|(1+\Lambda^{(0)})[\bar{V}(\omega), \tau_\mu]|0\rangle + \sum_\nu F_{\mu\nu} X_\nu^{(1)}(\omega)\Big) X_\mu^A(-\omega) \tag{2.60}$$
$$+ \sum_\mu X_\mu^{(1)}(\omega)\langle 0|(1+\Lambda^{(0)})[\bar{A}, \tau_\mu]|0\rangle.$$

The final form for the linear response function, Equation 2.60, has no computational advantages over the original form in Equation 2.49; it still remains necessary to solve for two sets of perturbed amplitudes. However, by using Equation 2.60 we are able to solve the same $X_\mu^{(1)}$ equations twice - once for the positive ω and once for the negative ω - rather than needing to implement separate equations for the left-hand perturbed amplitudes.

Chapter 3

Localized Optimized Orbitals, Coupled Cluster Theory, and Chiroptical Response Properties

H. R. McAlexander, T. J. Mach, and T. D. Crawford. *Phys. Chem. Chem. Phys.*, 14, 7830-7836. Reproduced by permission of the PCCP Owner Societies.

3.1 Introduction

First-principles simulations of the optical properties of chiral molecules[7,10,69–72] have seen tremendous advances in the last two decades. The two most widely used approaches, *viz.*,

density-functional theory (DFT)[73] and coupled cluster (CC) theory[21,74] have been extended to compute a variety of chiroptical responses, such as optical rotation,[6,75–77] electronic and vibrational circular dichroism spectra,[78–80] and Raman optical activity (ROA) spectra,[77,81–83] with the ultimate goal of providing computational tools for the assignment of absolute stereochemical configurations. Coupled cluster methods, in particular, have been shown to provide impressive accuracy, especially in the comparison to gas-phase experimental measurements.[7,72,77,84,85]

Two important complications associated with CC models of chiroptical response are gauge invariance and the high-degree polynomial scaling of the CC hierarchy of wave functions. The former arises due to the non-unique choice of representation of the electric-dipole operator in either the "length gauge", in which $\vec{\mu} = -\vec{r}$, or the "velocity gauge", where the linear momentum $-\vec{p}$ is used instead.[86] For fully variational quantum chemical methods such as Hartree-Fock self-consistent field (SCF), multiconfigurational SCF (MCSCF), or Kohn-Sham DFT, in which the electronic energy is stationary with respect to the molecular orbitals (MOs), both choices produce the same results in the limit of a complete atomic-orbital basis set. In conventional CC theory, on the other hand, where a fixed set of MOs is adopted, the length and velocity gauges yield different properties — sometimes dramatically different[87] — even in the complete-basis-set limit or when gauge-including atomic orbitals (GIAOs) are employed.[88–90] Gauge invariance (and the closely related property of origin independence) can be achieved in CC theory, however, through reformulation of the underlying response theory[91] coupled to variational optimization of the correlation energy

with respect to the MOs, known as the optimized orbital CC (OO-CC) approach.[86,87,92–94] Although a gauge-invariant OO-CC response-theory implementation has been reported for oscillator strengths,[15] the method has not yet been extended to chiroptical properties.

The Achilles' heel of conventional CC theory is its high-order scaling with molecular size [$\mathcal{O}(N^6)$ or worse]. This "polynomial scaling wall" prevents its routine application to larger, more chemically relevant molecules. The local correlation *ansatz* first suggested in the 1980s by Pulay and Saebø[25,95] provides one route to eliminating this problem and allowing for the development of linear scaling CC methods. The central assumption of this idea is that, by adopting well-localized forms of the MOs which are used to construct the determinantal expansion of the wave function, the parameters associated with interactions of electrons in spatially distant MOs should be negligible and may therefore be ignored. This approach has been utilized extensively by Werner, Schütz, and co-workers,[27,96] who have demonstrated that it is possible to obtain CC ground-state energies (including perturbative triple excitations) for chains of up to sixteen glycine molecules in a matter of hours using desktop workstations.[96] Alternative localization approaches have been proposed by Scuseria and Ayala,[97] Head-Gordon and co-workers,[98] Flocke and Bartlett,[99] Piecuch and co-workers.[39,100] and Neese and co-workers.[43,101] More recently, the local-CC (LCC) approach has been extended to electronically excited states[102–106] and molecular response properties.[55–58]

The goal of the present work is to combine the optimized-orbital and local-CC concepts in order to yield a reduced-scaling, yet high-accuracy method for simulations of the chiroptical response of large molecules. We focus specifically on optical rotations, in part because

of the existence of numerous previous studies of CC theory for this property. However, our general approach is not limited to optical rotations, and may be applied to numerous other properties as well. In the next section, we outline the theoretical underpinnings of both the OO-CC and LCC methods, as well as a new scheme for merging them together. We then apply the resulting pilot program to a number of paradigmatic chiral molecules, including [4]triangulane, 1-phenylethanol, and a series of fluoroalkanes to better understand the pitfalls and potential efficacy of a resulting locally correlated optimized orbital CC (LOO-CC) method.

3.2 Theoretical Approach

The goal is to compute with high accuracy the mixed electric-dipole/magnetic-dipole polarizability tensor,

$$\mathbf{G}'(\omega) = -\frac{2\omega}{\bar{H}} \sum_{j\neq 0} \frac{\mathrm{Im}(\langle\psi_0|\boldsymbol{\mu}|\psi_j\rangle\langle\psi_j|\mathbf{m}|\psi_0\rangle)}{\omega_{j0}^2 - \omega^2}, \tag{3.1}$$

also known as the Rosenfeld optical activity tensor,[69,107] using coupled cluster methods. In this expression, ω is the frequency of plane-polarized light, $\boldsymbol{\mu}$ and $\mathbf{m}$ are the electric- and magnetic-dipole operators respectively and the summation runs over the excited electronic (unperturbed) wave functions, ψ_j, each associated with an excitation frequency, ω_{j0}. The specific rotation is related to the trace of this tensor. The explicit summation over all electronically excited states in Eq. (3.1) is avoided in practice through the use of the formally equivalent and more efficient linear response approach.[11,108] This technique is utilized in

many quantum chemistry program suites including the PSI3 package, which was used in this work.[109]

Conventional CC theory typically makes use of a reference determinant, $|0\rangle$, comprised of Hartree-Fock SCF MOs as the starting point for the exponential expansion of the correlated wave function,

$$|\Psi_{\mathrm{CC}}\rangle = e^{\hat{T}}|0\rangle, \tag{3.2}$$

where the cluster operator, $\hat{T}$, generates substituted determinants according to a chosen truncation level [*e.g.*, $\hat{T} = \hat{T}_1 + \hat{T}_2$, which defines the CC singles and doubles (CCSD) model]. Unfortunately, as explained by Pedersen, Koch, and co-workers,[15,86,110] the use of non-optimized orbitals is directly related to the lack of invariance of the Rosenfeld tensor in Eq. (3.1) — and thus of computed properties such as optical rotation and circular dichroism rotational strengths — with respect to the choice of representation of the electric dipole operator. However, as shown in numerous previous studies,[92–94] the corresponding CC energy functional,[74]

$$E_{\mathrm{CC}} = \langle 0| \left(1 + \hat{\Lambda}\right) e^{-\hat{T}} \hat{H} e^{\hat{T}} |0\rangle, \tag{3.3}$$

may be variationally optimized with respect to first-order rotations, κ_{ai} among the occupied ($\{\phi_i\}$) and unoccupied ($\{\phi_a\}$) MOs to yield a set of stationary conditions,

$$\frac{\partial E_{\mathrm{CC}}}{\partial \kappa_{ai}} = 0. \tag{3.4}$$

The de-excitation cluster operator, $\hat{\Lambda}$, in the energy functional above may be viewed as a component of the left-hand CC wave function,

$$\langle \Psi_{\mathrm{CC}}| = \langle 0| \left(1 + \hat{\Lambda}\right) e^{-\hat{T}}. \tag{3.5}$$

The energy derivative with respect to orbital rotations in Eq. (3.4) appears as the inhomogeneous term in the linear Z-vector equations of Handy and Schaefer, and thus is properly viewed as the orbital Lagrangian[111] of CC analytic gradient theory.[66,93,112,113] Scuseria and Schaefer[93] first employed the Z-vector itself as the orbital rotation parameters, κ_{ai}, *via* a unitary transformation operator, $\exp(Z)$, and found that iterative optimization of the orbitals ultimately converges provided that the single-excitation contributions of $\hat{T}$ and $\hat{\Lambda}$ are excluded — yielding the OO-CCD approach — due to linear dependencies between the t_i^a and λ_a^i amplitudes and the κ_{ai} parameters.[93,94] However, as shown by Köhn and Olsen,[114] the exclusion of $\hat{T}_1$ and $\hat{\Lambda}_1$ implies that the OO-CC approach is not a formally exact method. Although the present OO-CC linear-response function implementation is not yet fully gauge invariant, neither it nor the more complete, gauge-invariant approach developed by Pedersen and Koch, suffers from unphysical second-order poles in the response function, which appear in Brueckner-orbital variants.[86]

In conventional CC theory, the MOs — whether Hartree-Fock, energy-optimized, or other choices — are typically delocalized, and the corresponding cluster amplitudes must be computed and stored for all occupied and unoccupied combinations. Localization schemes, such

as that devised by Pulay and Saebø and extended to CC theory by Werner, Schütz, and co-workers, take advantage of the short-range nature of electron correlation in molecules as well as the fact that unitary transformations of the active occupied or virtual MOs among themselves do not affect the wave function or its associated properties. Thus, the substitutions produced by the cluster operators, $\hat{T}$ and $\hat{\Lambda}$, may be limited only to those occupied/unoccupied MO groups that are spatially proximate, which are referred to as *domains*. For example, the double excitation cluster operator may be written in second quantized form as

$$\hat{T}_2 \approx \frac{1}{4} \sum_{ij} \sum_{ab \in [ij]} t_{ij}^{ab} a_a^\dagger a_b^\dagger a_j a_i \,, \tag{3.6}$$

where notation $ab \in [ij]$ indicates the summation over unoccupied orbitals, ϕ_a and ϕ_b is restricted to MOs near to the occupied pair ϕ_i and ϕ_j. As a result, vast numbers of wave function amplitudes may be neglected with little impact on the accuracy of the CC approach, as long as the correlation domains include all relevant orbital contributions.

The most widely used approach to domain selection was devised by Boughton and Pulay (BP),[115] who demonstrated that numerical comparison between occupied MOs constructed using subsets of the atomic orbital (AO) basis functions (centered at the nuclei) and the original localized MOs yields a useful "completeness check" for a given MO. Werner and Pflüger[116] reported that this approach (with various improvements, particularly for orbital pairs) produces correlation domains appropriate for computing, for example, reaction energies to high accuracy, that are relatively compact, typically involving only basis functions on bonded atoms, lone pairs, etc. However, in order to obtain robust predictions of molecular

response properties, such as dipole polarizability or optical rotations, the domains must be expanded considerably.[56,58] As discussed in earlier work, one approach to augmenting the domains is to consider the first-order perturbation of the Hartree-Fock MOs with respect to the germane external electric or magnetic fields. This scheme, referred to here as the coupled-perturbed Hartree-Fock (CPHF) approach, was demonstrated by Russ and Crawford[56,58] to produce extensions to the BP domains that respond to the applied fields. These domains are necessarily larger than those applicable to simple energy computations, but, in the test cases considered thus far, conserve the accuracy required of the CCLR model. In the computations described below, the CPHF scheme will be applied to domain selection in conjunction with localized optimized orbitals to determine if the expected accuracy of coupled cluster remains intact.

3.3 Computational Details

The purpose of the present work is to examine the impact of localized, optimized orbitals on the CCLR scheme as compared to our previously reported study, which was based on localized Hartree-Fock (HF) orbitals. In the LOO-CCD method developed here, the occupied HF MOs are localized using the Pipek-Mezey algorithm[117] and then re-localized in each iteration of the orbital optimization procedure. The virtual-orbital space is constructed following the recipe of Pulay and Saebø, i.e. projected atomic orbitals (PAOs).[95] Following each localization, the occupied orbital domains are recomputed to account for any changes

induced by orbital relaxation. For comparison to previous work,[58] single-excitation domains remain untruncated in the present pilot code, and all occupied-orbital pairs are included. This implies that the number of double-excitation amplitudes scales quadratically with the size of the molecular system in the present work, though techniques to differentiate between strong- and weak-pair contributions such as those utilized by Werner and co-workers, as well as distance cutoffs for the singles can be used in a production-level program to reduce the scaling to linear. Such a large-scale implementation is currently under development in our group. In addition, we have examined modifications in which the initial correlation domains are held fixed throughout the procedure, as well as simple modifications of the Boughton-Pulay domains to include the next neighbor of key atoms (*vide infra*). We have also considered alternate approaches to the application of the local-correlation concept to OO-CC, varying according to the point in the computation in which the occupied MOs are localized and whether the localization is constrained; but these variants hold no potential for significantly improved scaling. All calculations presented here were carried out using the open-source PSI suite of quantum chemical programs.[109]

Specific rotations were calculated for the molecules depicted in Fig. 3.1:(*P*)-[4]triangulane, and (*S*)-1-phenylethanol, and selected fluoroalkanes, using CCSD, LCCSD, OO-CCD, and LOO-CCD methods, as outlined above. All structures were optimized at the B3LYP/6-31G** level of theory,[118–120] as in previous studies.[58,121] Although the fluoroalkanes are not optically active due to conformational averaging, we have selected for each molecule a single asymmetric conformer with a negative optimized F-C_1-C_2-C_3 dihedral angle, as used in our

Figure 3.1: Chiral molecules used as test cases for the LOO-CCD model.

(a) 1-fluoropentane

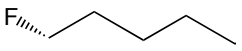

(b) 1-fluoroheptane

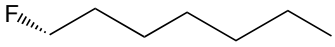

(c) (*P*)-[4]triangulane

(d) (*S*)-1-phenylethanol

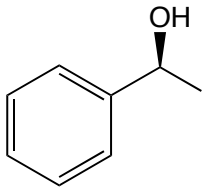

earlier work.[58]

Basis sets used for computing optical rotations include the 6-31+G* split valence basis of Pople and co-workers[122] and the aug-cc-pVDZ basis set of Dunning and co-workers.[123,124] The modified velocity gauge (MVG) representation of the electric-dipole operator was used to ensure origin-independent rotations.[13] Specific rotations were calculated at four wavelengths: 355 nm, 436 nm, 589 nm, and 633 nm. Both CPHF-based and BP orbital domains were used for the local calculations. For the CPHF-based domains, the cutoffs ranged from 0.05-0.2. Also, extended BP domains were tested for fluoroheptane in which neighboring atoms were included. Core orbitals were held frozen in all coupled cluster computations.

3.4 Results and Discussion

Specific optical rotations at 355 nm for fluoropentane are given for two basis sets in Table 3.1 for the Hartree-Fock-based CCSD and OO-CCD, as well as their localized variants. Ideally, we seek maximum localization errors of ca. 5%, obviously with retention of the sign of canonical rotation. Both local methods are in good agreement with their canonical counterparts, differing at most by about 5 deg dm^{-1} $(\mathrm{g/mL})^{-1}(3.5\%)$. Changes in the optical rotations are notable between the two basis sets, but the difference is comparable for both the canonical and local approaches. Given that the purpose of this analysis is only to consider the effectiveness of the localization schemes, the good comparison between the canonical and local approaches is noteworthy.

One measure of the efficacy of a local-correlation approach is the ratio of $\hat{T}_2$ amplitudes that must be computed and stored in the local algorithm to the number of such amplitudes in the canonical-MO algorithm, and this is reported for 1-fluoropentane in Table 3.1. For LOO-CCD, the $\hat{T}_2$ amplitudes and corresponding ratios are recomputed in each iteration of the orbital optimization because the correlation domains are allowed to change. Nevertheless, the $\hat{T}_2$ ratio is identical between LCCSD and LOO-CCD, indicating that the localization structure is equally effective with the optimized orbitals. All selected ratios for LOO-CCD are the "worst case scenario" for each method; the highest $\hat{T}_2$ ratios are given. As to be expected, the aug-cc-pVDZ basis set benefits more from the localization procedure, with $\hat{T}_2$ ratios roughly 40% less than that of the 6-31+G* basis. Also, better agreement between

CCSD and OO-CCD and between LCCSD and LOO-CCD is achieved with the augmented basis set.

Table 3.1: Specific Rotations (in deg dm^{-1} $(g/mL)^{-1}$) of 1-fluoropentane (MVG, 355 nm). A CPHF cutoff of 0.20 was used for all local-CC computations. Corresponding $\hat{T}_2$ ratios are given in parentheses.

Basis Set	CCSD	OO-CCD	LCCSD	LOO-CCD
6-31+G*	-167.5	-169.1	-163.4 (0.87)	-166.5 (0.87)
aug-cc-pVDZ	-152.7	-154.0	-148.2 (0.51)	-148.6 (0.52)

Specific rotations at 355 nm for fluoroheptane are given in Table 3.2 for the local-correlation methods. Compared to the canonical CCSD and OO-CCD rotations of -136.2 and -137.5 deg dm^{-1} $(g/mL)^{-1}$, respectively, the CPHF domains generally perform well, with only small differences between the Hartree-Fock-based localization and the optimized-orbital approaches. Interestingly, although the 0.05 CPHF cutoff naturally yields the best comparison with the canonical results (due to the minimally truncated domains), the larger 0.20 cutoff actually yields slightly better results than the 0.10 and 0.15 cutoffs, suggesting that a cancellation of errors is present. The 0.15 cutoff resulted in a failed convergence of the localized optimized orbitals in this case, due to oscillations of the local domains (discussed further below), which can be damped in a production-level implementation.

In Table 3.3, optical rotations for the larger fluorononane are given, and it is clearly seen that the scaling is more favorable compared to fluorheptane and fluoropentane. In particular, the 0.20 CPHF cutoff yields $\hat{T}_2$ ratios of only 0.56 for both LCCSD and 0.58 for LOO-CCD for fluorononane as compared to 0.71 for both methods for fluoroheptane. This ratio will

Table 3.2: Local-CC specific rotations for 1-fluoroheptane (MVG, 355 nm, 6-31+G*) using the Boughton-Pulay (BP) and various choices of cutoff for CPHF-based orbital domains. Corresponding $\hat{T}_2$ ratios are given in parentheses. The notation "n/c" indicates that the orbital optimization procedure did not converge. Note that the canonical CCSD and OO-CCD specific rotations are -136.2 and -137.5 deg dm^{-1} (g/mL)$^{-1}$, respectively.

Cutoff	LCCSD	LOO-CCD
BP	-105.0 (0.11)	-107.2 (0.11)
0.05	-135.7 (0.99)	-135.6 (0.99)
0.10	-131.6 (0.82)	-129.2 (0.82)
0.15	-131.6 (0.78)	n/c
0.20	-133.7 (0.71)	-132.2 (0.71)

continue to decrease for larger chains, as discussed in the work by Russ and Crawford.[58] Also, the relatively small sensitivity to domain sizes observed for fluoroheptane is also present in this case, as well as the apparent improvement in the comparison to the canonical CCSD and OO-CCD values with larger CPHF cutoffs.

Table 3.3: Specific Rotations (in deg dm^{-1} (g/mL)$^{-1}$) of 1-fluorononane (MVG, 355 nm, 6-31+G*) for both BP domains and CPHF domains using several choices of cutoff. Corresponding $\hat{T}_2$ ratios are given in parentheses. Note that the canonical CCSD and OO-CCD specific rotations are -111.2 and -112.3 deg dm^{-1} (g/mL)$^{-1}$, respectively.

Cutoff	LCCSD	LOO-CCD
BP	-83.7 (0.07)	-85.9 (0.07)
0.05	-106.3 (0.84)	-107.6 (0.84)
0.10	-105.5 (0.71)	-106.0 (0.71)
0.15	-107.2 (0.62)	-108.6 (0.62)
0.20	-108.1 (0.56)	-109.5 (0.58)

Localized and non-localized highest-occupied MOs for (*P*)-[4]triangulane and (*S*)-1-phenylethanol are presented in Figure 3.2. The non-localized forms are representative of the Hartree-Fock canonical MOs, and the OO-CCD optimized MOs, while the localized forms are relevant

Figure 3.2: Non-localized and localized HOMOs of (*P*)-[4]triangulane (a, b) and (*S*)-1-phenylethanol (c, d).

(a) Non-localized

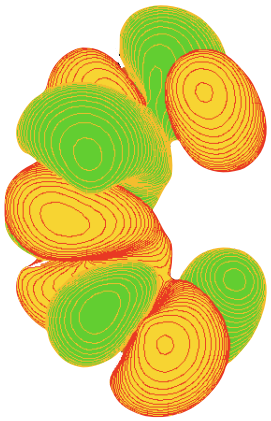

(b) Localized

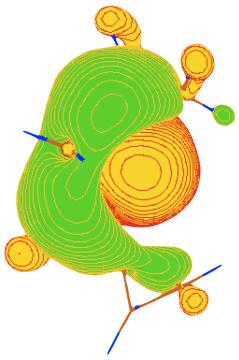

(c) Non-localized

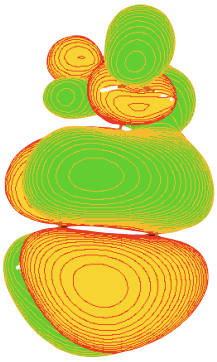

(d) Localized

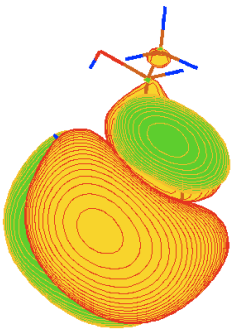

to the LCCSD and LOO-CCD approaches. In both molecules, the localization is less effective than observed in other systems,[27] due primarily to the strong conjugation occurring in the phenyl ring of 1-phenylethanol as well as the partial conjugation present in the twisted-propane chains of [4]triangulane. This leads naturally to larger domains in the local-correlation models. However, even the small degree of localizability yields some computational benefits for these relatively small molecules. As observed for the fluoroalkanes above and as discussed in earlier work,[58] as the size of the molecules increases, the localization of the MOs and thus the computational efficiency of the localized methods will naturally improve. The important question at hand is whether the LOO-CCD method yields comparable results to the LCCSD method.

Optical rotations for (*P*)-[4]triangulane, and (*S*)-1-phenylethanol with the largest CPHF cutoff (0.20) are given in Table 3.4. LOO-CCD performs well compared to LCCSD over a range of wavelengths, suggesting that the localization introduces little error over the dispersion curves. The 0.20 CPHF cutoff works reasonably well for each method for these two molecules (see Table 3.4). Localization errors arising from LOO-CCD are 9-10% for [4]triangulane, but much smaller — less than 2% — for 1-phenylethanol. This difference is partly due to the reduced natural localization in 1-phenylethanol, as observed in Fig. 3.2. However, in certain cases, the orbital optimization procedure failed to converge. Table 3.5 reports the specific rotations for each local method for several choices of domain cutoff for (*P*)-[4]triangulane and (*S*)-1-phenylethanol. For (*S*)-1-phenylethanol the LOO-CCD rotation with the 0.10 cutoff fails to converge, and for (*P*)-[4]-triangulane, the LOO-CCD MOs

fail to converge with both the BP domains and the CPHF cutoff of 0.15. In these cases, the orbital optimization procedure conflicts with the enforced localization in that the sizes of the orbital domains oscillate between iterations. This could be overcome, for example, by choosing static domain definitions at the beginning of the calculation. However, in systems where orbital relaxation is significant, static domains could perform very poorly by neglecting important changes in the orbital structures and domains. It would be possible, however, to continue to calculate the domains each iteration, updating them when necessary or perhaps only after some pre-selected number of iterations of the optimization procedure.

Table 3.4: Specific Rotations (deg dm^{-1} $(g/mL)^{-1}$) of (*P*)-[4]triangulane and (*S*)-1-phenylethanol (MVG, 6-31+G*). A CPHF cutoff of 0.20 was used for all local-CC computations.

Molecule	Wavelength	CCSD	OO-CCD	LCCSD	LOO-CCD
(*P*)-[4]triangulane	355 nm	617.1	617.9	655.6	672.1
	436 nm	360.3	361.2	387.7	395.4
	589 nm	177.7	178.3	190.5	196.2
	633 nm	151.3	151.9	162.4	167.3
(*S*)-1-phenylethanol	355 nm	-489.9	-493.6	-485.7	-485.9
	436 nm	-284.8	-287.1	-283.1	-283.3
	589 nm	-140.3	-141.4	-139.7	-139.8
	633 nm	-119.4	-120.4	-119.0	-119.1

We have also investigated an alternative domain-selection approach in which the BP domains are extended to nearest-neighbor atoms. This approach naturally gives rise to numerous variations, such as the inclusion only of bonded neighboring atoms, with or without attached hydrogen atoms, additional extensions for "special" atoms, such as those attached to stereogenic centers, etc. We have carried out such domain extensions for the fluoroheptane test

Table 3.5: Local-CC specific rotations for (*P*)-[4]triangulane and (*S*)-1-phenylethanol using the Boughton-Pulay (BP) and various choices of cutoff for CPHF-based orbital domains, with the 6-31+G* basis set. Corresponding $\hat{T}_2$ ratios are given in parentheses. The notation "n/c" indicates that the orbital optimization procedure did not converge.

Molecule	(*P*)-[4]triangulane		(*S*)-1-phenylethanol	
Cutoff	LCCSD	LOO-CCD	LCCSD	LOO-CCD
BP	634.8 (0.16)	641.7 (0.16)	-394.8 (0.37)	n/c
0.05	641.5 (1.13)	627.4 (1.13)	-491.3 (1.18)	-494.7 (1.18)
0.10	646.7 (1.01)	n/c	-484.2 (1.05)	-489.7 (1.05)
0.15	644.7 (0.89)	650.0 (0.90)	-488.6 (0.95)	n/c
0.20	655.6 (0.79)	672.1 (0.79)	-485.7 (0.89)	-485.9 (0.89)

case, the results of which are shown in Table 3.6. The traditional BP calculation yields a very attractive computational scaling, but, unsurprisingly, at a severe deterioration of the method's accuracy (about 20% in this case).[58] The $\hat{T}_2$ ratios for the BP domains with neighboring atoms included (BP:all) increase by a factor of 4, but are still less than the CPHF based domains. In addition, the BP:all computation reduces the localization error relative to the canonical CCSD and OO-CCD rotations to about 20 deg dm^{-1} $(\mathrm{g/mL})^{-1}$(14%). Including the neighbors' hydrogen atoms (BP:all+H) provides another boost to the accuracy with a modest decrease in efficiency compared to BP:all, with localization errors of 10 deg dm^{-1} $(\mathrm{g/mL})^{-1}$(7%). This is greater than the error desired (ca. 5%) and larger than that obtained with the CPHF domains for this test case (2%), but the efficiency of the BP:all+H domains is also higher, with a $\hat{T}_2$ ratio of 0.71 for the 0.20 CPHF domain compared to 0.58 for the BP:all+H. The advantage of the approach is its relative simplicity, but the question as to whether such domains are sufficient for different types of external-field perturbations remains open.

Table 3.6: Local-CC specific rotations for 1-fluoroheptane (MVG, 355 nm, 6-31+G*) using the Boughton-Pulay (BP) and extended BP orbital domains. Corresponding $\hat{T}_2$ ratios are given in parentheses. The BP:all and BP:all+H domains were obtained by including the next neighbor atoms and their hydrogens, respectively. For BP:F and BP:F+H, only domains including the fluorine atom were augmented. The notation "n/c" indicates that the orbital optimization procedure did not converge. Note that the canonical CCSD and OO-CCD specific rotations are -136.2 and -137.5 deg dm^{-1} $(g/mL)^{-1}$, respectively.

Domain	LCCSD	LOO-CCD
BP	-105.0 (0.11)	-107.2 (0.11)
BP:all	-117.3 (0.48)	-119.3 (0.48)
BP:all+H	-126.2 (0.58)	-129.0 (0.58)
BP:F	-105.7 (0.13)	-106.5 (0.13)
BP:F+H	-113.9 (0.14)	n/c

In a similar manner, we also tested just increasing the domains which included the fluorine atom, as this is the source of optical activity in the rigid fluoroheptane's structure (BP:F). Only a few domains contained the fluorine atom, and its only direct neighbor is the terminal carbon. For this approach, the $\hat{T}_2$ ratio is, of course, very similar to the original BP domains, but the localization errors remain unacceptably large. Alternatively, adding not only the fluorine-attached carbon atom but also its associated hydrogen atoms (BP:F+H) yields a somewhat larger reduction in the localization error, but the error is still larger than desired and the LOO-CCD scheme failed to converge with this approach.

3.5 Conclusions

We have examined the efficacy of MO localization on the OO-CCD approach as a starting point for the development of a robust, local gauge-invariant coupled cluster method for pre-

dicting the chiroptical properties of large molecules. In the LOO-CCD method examined here, the HF orbitals are localized at the beginning of the calculation, and then re-localized in each iteration of the MO optimization process (and the correlation domains re-computed). In this manner, locality — and thus the potential for notable computational savings — are maintained throughout the computation. The LOO-CCD method yields specific rotations that are reasoanbly close to canonical CCSD and OO-CCD calculations, though in select cases the orbital optimization procedure failed to converge due to oscillations in the definitions of the orbital domains. Most importantly, however, the LOO-CCD approach is nearly identical in its performance to the LCCSD method, indicating that the optimization of the MOs does not hinder their subsequent localization. Augmentation of the BP domains by nearest-neighbor atoms for the entire system or select atoms or fragments could improve efficiency and potentially circumvent issues with changes in domain sizes, but the domain selection to achieve accurate results is not necessarily automatic when focusing on certain chemical components of a structure. Overall, LOO-CCD produces values comparable to canonical CC and maintains the scaling benefits of LCCSD. This demonstrates the potential usefulness of a locally correlated OO-CCD approach that will provide both robust gauge invariance as well as high accuracy for large, chiral molecules.

Chapter 4

A Comparison of Three Approaches to the Reduced-Scaling Coupled Cluster Treatment of Non-Resonant Molecular Response Properties

4.1 Introduction

Theoretical chemistry is an essential tool of scientific investigation, standing as "a full partner with experiment" in discovery.[125–128] Unfortunately, the most robust and reliable theoretical methods also come with a steep computational price, and accurate methods such as coupled

cluster theory rapidly become impractical for use for large chemical systems.[18–24] The coupled cluster singles and doubles (CCSD) method, for example, scales as $\mathcal{O}(N^6)$ (iterative), where N represents the size of the molecular system, while the most popular perturbational correction for connected triples, (T), scales as $\mathcal{O}(N^7)$ (non-iterative). In the effort to reduce these high-degree polynomial scalings, a number of techniques have been developed to introduce greater sparsity in the coupled cluster wave function, including methods based on orbital localization, fragment, or other techniques,[25–53] with varying degrees of success.

Among these, one of the most widely used is the projected-atomic-orbital (PAO) approach pioneered by Pulay and Sæbø[25,61,62,95] and has been greatly advanced within coupled cluster theory by Werner, Schütz, and co-workers.[27,29–33,129,130] For properties related to ground-state energies, e.g., reaction enthalpies and other thermodynamic constants, for which the response or derivative of the wavefunction is not needed,[27,29–33,62,95,129,130] such methods have proven to be invaluable for treating large systems with little loss of accuracy compared to canonical approaches. Even for properties such as excitation energies, much progress has been made, and a number of reduced-scaling schemes have been introduced.[102–105,131–133] However, the application of localization methods to higher-order response properties — e.g. (hyper)polarizabilities, magnetizabilities, and chiroptical response — has been much more limited.[54–60]

One of the first examinations of the performance of local coupled cluster methods for field-dependent response properties was reported by Korona and Werner[55] where they considered dipole moments and static polarizabilities with the local coupled cluster singles and doubles

(LCCSD) approach.[55] Using the PAO recipe, they found that such electric-field-dependent properties were much more sensitive to orbital relaxation effects compared to untruncated calculations, but nonetheless the average error for their test set remained small. They also showed that they could further reduce such errors by extending the virtual space for significant pairs beyond the standard domains that would otherwise have been sufficient for ground-state energy calculations.

Russ and Crawford also applied the PAO approach to both static and dynamic dipole-polarizabilities using coupled cluster theory.[56,58] In their first work, they introduced a new orbital-domain selection scheme based on the first-order response of the ground-state molecular orbitals to the external electric field as determined via the coupled-perturbed Hartree Fock (CPHF) equations.[56] This approach naturally led to larger orbital domains than those required for ground-state energies, in agreement with the findings of Korona and Werner. They later extended this work to dynamic response properties, including frequency-dependent polarizabilities and mixed electric-/magnetic-field-dependent properties such as optical rotations of chiral compounds.[58] They found that such methods exhibited localization errors of only a few percent compared to the canonical approach for (pseudo)linear molecular structures. However, two- and three-dimensional structures such as the cage-like compound (1*R*,4*R*)-norbornenone required significantly larger domains — and thus much greater computational demands — for similarly accurate optical rotations.[134]

This work was later extended by McAlexander *et al.* to the optimized-orbital coupled cluster (OO-CC) method[59] in an effort to develop a reduced-scaling coupled cluster model that

was also gauge invariant for magnetic-field-dependent properties. One of the drawbacks to conventional (truncated) coupled cluster methods when applied to chiroptical properties, such as optical rotations, is that the computed property depends on the choice of length vs. velocity representation of operators such as the electric dipole operator.[69] As shown by Pedersen and Koch,[15,86] variational optimization of the underlying molecular orbitals, in conjunction with large one-electron basis sets and/or gauge-including atomic orbitals (GIAOs),[89,135] can overcome this inadequacy. McAlexander and co-workers applied the PAO-LCC approach to the OO-CC formalism to determine if such optimization impacted the scaling of the method.[59] In order to maintain a strongly sparse wave function structure, the molecular orbitals were relocalized in each iteration of the orbital optimization. They found that, in some instances, oscillations in the domains sizes caused the orbital optimization to fail, but, in general, the accuracy of the local orbital-optimized coupled-cluster doubles (LOO-CCD) calculations were similar in accuracy to the LCCSD calculations.

Most recently, Friedrich *et al.* applied the incremental scheme to CCSD frequency-dependent dipole polarizabilities. Compared to the PAO approach, the incremental scheme[26,41,42] employs a fragmentation-like, N-body structure to reduce the computational cost. At the second-order level, they achieved results with an average error of 0.6% for a 47-molecule test set. Furthermore, similar to Crawford and Russ,[58] they noted the increased error for complex, three-dimensional systems where the number of important interactions is larger than for simple, (pseudo)linear structures.

While the PAO approach has been the most heavily applied reduced-scaling coupled cluster

method, two other schemes have seen significant development in the last several years: the local pair natural orbital (LPNO) approach resurrected by Neese and co-workers,[43,44] and the orbital-specific virtual (OSV) approach by Chan and co-workers.[49,50] Given the poorer scaling exhibited by the PAO-based LCC approach as noted above for the response properties of three-dimensional structures, a natural question arises as to the efficacy of these newly emerging local correlation approaches for such properties.

Herein we report the first application of the LPNO and OSV schemes to the calculation of coupled cluster non-resonant response properties,[8,10,11] particularly dynamic polarizabilities and specific optical rotations. We choose as our benchmark systems a set of pseudo-linear, two-dimensional, and three-dimensional molecular structures. We consider the impact of various truncation schemes, including those limited only to the double excitation components of the wave function vs. truncation of both singles and doubles, as well as exclusion of so-called weak pairs. The relative performance of each method is compared to both conventional coupled cluster methods and the PAO approach.

4.2 Theory

4.2.1 Response Theory

Coupled cluster linear response (CCLR) theory[8,11] has proven to be an effective and useful tool for calculating various properties of small molecules.[10] The linear response function may

be derived as the second derivative of a time-averaged Lagrangian (quasi-energy) with respect to external perturbations $\vec{A}$ and $\vec{B}$. Within coupled cluster theory, the general expression is

$$\begin{aligned}\left\langle\left\langle \vec{A};\vec{B} \right\rangle\right\rangle_{\omega} &= \frac{\mathrm{d}^2\{L_{CC}\}_t}{\mathrm{d}\vec{A}\mathrm{d}\vec{B}} \\ &= \frac{1}{2}\hat{C}^{\pm\omega}\hat{P}[A(-\omega),B(+\omega)] \\ &\times\left[\langle\phi_0|\Lambda[\bar{A},X^B_{\omega}]|\phi_0\rangle + \frac{1}{2}\langle\phi_0|\Lambda[[\bar{H},X^A_{-\omega}],X^B_{\omega}]|\phi_0\rangle\right] \end{aligned} \tag{4.1}$$

where ϕ_0 is the reference wavefunction, Λ is the de-excitation operator associated with the left-hand wavefunction amplitudes, $\hat{C}$ is a symmetrizer with respect to interchanging the sign and taking the complex conjugate of the frequency, and $\hat{P}$ symmetrizes the perturbation operators. Quantities with an overbar have been similarity transformed with the ground state coupled cluster exponential operator,

$$\bar{H} = e^{-T}He^{T}. \tag{4.2}$$

To obtain the perturbed amplitudes, X^A and X^B, the linear systems of equations must be solved:

$$\langle\phi|(\bar{H}-\omega)X^A_{\omega}|\phi_0\rangle = -\langle\phi|\bar{A}|\phi_0\rangle. \tag{4.3}$$

In the case of polarizabilities, where the perturbation operator is the electric dipole operator, only a single set of perturbed amplitudes (at both the positive and negative of the frequency) need be solved for. For optical rotations, on the other hand, we must obtain perturbed

wavefunction parameters for both the electric and magnetic dipole operators, $\boldsymbol{\mu}$ and $\mathbf{m}$. The linear response function then takes on the form

$$-\langle\langle \boldsymbol{\mu}; \mathbf{m} \rangle\rangle_{\omega} = -\mathrm{Im}\Big\{ \hat{C}^{\pm\omega} \hat{P} \left(\boldsymbol{\mu}_{-\omega}, \mathbf{m}_{\omega}\right) \Big[\langle \phi_0 | \hat{\Lambda}[\boldsymbol{\mu}, \hat{X}^{\omega}_{m}] | \phi_0 \rangle + \frac{1}{2} \langle \phi_0 | \hat{\Lambda}[[\bar{H}, \hat{X}^{\omega}_{\mu}], \hat{X}^{-\omega}_{m}] | \phi_0 \rangle \Big] \Big\}. \tag{4.4}$$

A CCLR optical rotation calculation is at the very least costly in terms of the number of perturbed amplitudes which must be obtained. This is, of course, also true for polarizability calculations. Even when dealing with only one perturbation operator, it is still necessary to solve for the x, y, and z components at both the positive and negative frequency. An accurate, robust local method would go a long a way to reduce the high cost of such calculations. However, it is unclear whether the perturbed amplitudes are insensitive enough to local correlation techniques to undergo the sufficient truncation for favorable scaling. Property calculations could possibly suffer from a double dose of truncation error - both ground state and perturbed amplitudes are truncated - and may be less amenable to local methods from the start. Alternatively, the properties may be intrinsically sensitive only to the truncation of the perturbation operator and/or perturbed amplitudes. As a step toward answering these questions, we test three local correlation techniques applied to coupled cluster calculations of frequency dependent polarizabilities and optical rotations.

4.2.2 Local Correlation Approaches

The rationale that underlies these three local correlation techniques is to transform the virtual orbitals into a basis that is local in nature. This locality may manifest in some physical sense such that the virtual orbitals can be associated with certain areas or domains, or that the new orbitals are intrinsically sparse and may be reduced/truncated in some systematic, logical manner. Hopefully, the most important information contained in the wavefunction may be compressed into the smallest possible virtual space, while still retaining very high accuracy upon truncation.

A key difference in the formulation in each of these methods is the nature of the new virtual space. While the PAO approach defines a single new virtual space that is used (at least partially) for all occupied orbitals/orbital pairs, the OSV and PNO methods provide for a unique virtual orbital space for each occupied orbital and occupied orbital pair, respectively. Technically speaking, the PNO space is the largest since, in the case of zero truncation, the virtual space is $N_{occ}^{pairs}v$, where N_{occ}^{pairs} is the number of unique occupied orbital pairs and v is the size of the canonical virtual space. The total number of OSVs is in between that of PNOs and PAO, being only $N_{occ}v$. Lastly, the number of PAOS will be no larger than the number of atomic orbitals. As a general statement of the relative sizes, we have

$$N_{PAO} < N_{OSV} < N_{PNO}. \tag{4.5}$$

In practice, though, these types of calculations are always truncated so that savings are

achieved, and these worst case scenarios are never encountered.

The orbital conventions used in this paper are as follows: $\mu, \nu, \lambda, \ldots$ pertain to atomic orbitals, $i, j, k, \ldots$ for localized, occupied orbitals, $a, b, c, \ldots$ for canonical virtual molecular orbitals, $\bar{\mu}, \bar{\nu}, \bar{\lambda}, \ldots$ for projected atomic orbitals, and finally $\bar{a}_{ij]}, \bar{b}_{ij}, \bar{c}_{ij}, \ldots$ for virtual orbitals in the PNO or OSV basis where the subscript denotes the pair/orbital-specific basis to which the orbital belongs. Additionally, quantities with an overbar are in the PNO/OSV basis, while quantities with a hat are in the pair/orbital-specific semicanonical basis.

PAOs

In the PAO approach, the occupied orbitals are subjected to the desired localization scheme, such as the Boys[136] or Pipek-Mezey[117] procedures, after the initial Hartree Fock calculation. The virtual space, on the other hand, is transformed to a projected-orbital basis. The canonical virtual orbitals have been back expanded in terms of atomic orbitals where contributions from occupied orbitals are removed. The projection operator illustrates this clearly:

$$|\chi_{\bar{\mu}}\rangle = \left(1 - \sum_i |\chi_i\rangle\langle\chi_i|\right)|\chi_\mu\rangle. \tag{4.6}$$

The essence of the projected-atomic orbital approach arises from the construction of occupied orbital domains, such that the virtual space for a given occupied orbital is a certain subset of the full PAO virtual space. In the first step, atoms are assigned to localized occupied orbitals on some basis, such as Mulliken orbital charges. The PAOs associated with these

atoms then become the domain of that particular occupied orbital:

$$\chi_{\bar{\mu}} \in A \in \chi_i. \tag{4.7}$$

While the local PAOs come at the cost of non-orthogonality among themselves, they remain orthogonal to the occupied space. To ensure the domains are appropriately constructed, two different checks have been developed. The first is that of Boughton and Pulay[115], which serves as an automatic check for the completeness of an orbital domain:

$$f_i(\acute{\mathbf{C}}) = min\left[\int(\chi_i - \acute{\chi}_i)^2 d\tau\right] = 1 = \sum_{\mu\in[i]}\sum_{\nu}\acute{C}^i_\mu S_{\mu\nu} C^i_\nu \tag{4.8}$$

where the $\acute{\chi}_i$, with the corresponding MO coefficients $\acute{C}^i_\mu$, is the approximation to χ_i constructed from the current set of domain-included PAOs.

Alternate domain schemes have been designed to take into account magnetic and/or electric perturbations through the coupled-perturbed Hartree-Fock (CPHF) equations.[56,58] The HF property tensor contributions are are decomposed on an atom by atom basis in a manner similar to the original domain scheme. For electric perturbations, for example

$$\alpha_{xy} = \sum_{occ}^{i}\sum_{a}^{vir} U^x_{ai}\mu^y_{ai} \tag{4.9}$$

$$= \sum_{occ}^{i}\sum_{\rho}^{AO} U^x_{\rho i}\mu^y_{\rho i}, \tag{4.10}$$

where in the second line we have back-expanded the sum over virtuals to a sum over atomic

orbitals (denoted by ρ). For a single orbital, we have

$$\alpha_{xy}^{iA} = \sum_{\rho \in A}^{AO} U_{\rho i}^{x} \mu_{\rho i}^{y}. \tag{4.11}$$

Directly analogous expressions may be derived for other perturbations. Keeping in mind that contributions may have both negative and positive signs, a completeness check has been proposed as

$$\varepsilon_{xy}^{i} = \sum_{\rho}^{AO} |U_{\rho i}^{x} \mu_{\rho i}^{y}| - \sum_{\rho \in [i]}^{AO} |U_{\rho i}^{x} \mu_{\rho i}^{y}|. \tag{4.12}$$

PNOs and OSVs

Similarly, the OSV and PNO techniques make use of localized occupied orbitals. Using the approximate MP2 amplitudes,

$$T_{ab}^{ij} = \frac{\langle ab|ij\rangle}{f_{ii} - f_{jj} + \epsilon_a + \epsilon_b} \tag{4.13}$$

a pair specific (each ij) or orbital specific (each ii) virtual density may be constructed:

$$\mathbf{D}^{ij} = \frac{2}{1 + \delta_{ij}} \left(\mathbf{T}^{ij} \tilde{\mathbf{T}}^{ij\dagger} + \mathbf{T}^{ij\dagger} \tilde{\mathbf{T}}^{ij} \right) \tag{4.14}$$

with

$$\tilde{\mathbf{T}}^{ij} = 2\mathbf{T}^{ij} - \mathbf{T}^{ij\dagger}. \tag{4.15}$$

Diagonalization of the density yields the PNOs or OSVs for a given pair or orbital, with associated occupation numbers. Orbitals in each basis with occupation numbers below a given threshold are neglected:

$$\mathbf{D}^{ij}\mathbf{Q}^{ij} = \mathbf{Q}^{ij}\mathbf{n}^{ij} \tag{4.16}$$

$$\mathbf{Q}^{ij} \approx \sum_{a} \sum_{\bar{a}_{ij} \in [ij]} Q^{ij}_{a\bar{a}_{ij}} \tag{4.17}$$

where

$$\bar{a}_{ij} \in [ij] \text{ such that } n^{ij}_{\bar{a}^{ij}} > \text{cutoff.} \tag{4.18}$$

For the OSV approach, the non-diagonal transformation matrix is formed by concatenating the transforms for pair ii and jj.

$$\mathbf{Q}^{ij} \equiv \mathbf{Q}^{ii}\mathbf{Q}^{jj} \quad \text{(OSV)}. \tag{4.19}$$

Unlike the PAO approach, PNOs or OSVs are orthogonal for a given pair, but non-orthogonal between different pairs, yielding an overlap

$$\mathbf{S}^{ij,kl} = \mathbf{Q}^{ij\dagger}\mathbf{Q}^{kl}. \tag{4.20}$$

Pair Truncations

In order to approach truly linear scaling in calculations, truncating only the virtual space is not sufficient - additional approximations must be introduced. One of the most common techniques is to categorize the various occupied pairs such that only a subset are treated in the full manner, while the other set or sets are neglected or treated in a less costly way. In PAO calculations, the pair-rankings can straightforwardly be based on the number of common PAOs between the domains of two occupied orbitals.[27] For instance, an occupied pair with no shared PAOs may be labeled as "very weak" and neglected. Also, the pair hierarchy may be defined using distance cutoffs as well.

For the OSV and PAO approaches, since the virtual space for each occupied pair is distinct a new pair truncation scheme must be employed. The typical way to truncate pairs for these methods is based on the approximate MP2 pair energies.[43] If the pair energy is below a threshold, it may be dropped or treated in a more approximate manner.

4.2.3 Implementation: Local Filter Technique

In order to evaluate the efficacy of these new techniques on coupled cluster linear response properties, a simulation code was developed inside the PSI4[137] programming package. While no computational savings are achieved, the simulation code allows for quick testing of the local correlation techniques without the need to implement production level local response code. The same approach is highlighted also by others.[27,58,59,62,102] Once the appropriate

transformation matrices are acquired, the simulation code works similarly for all three methods.

In each iteration, the coupled cluster amplitude residuals are transformed from the canonical MO basis to the local basis, then to a semicanonical pair- or orbital-specific basis where the virtual block of the Fock matrix is diagonal.

$$\overline{\mathbf{R}}^{ij} = \mathbf{Q}^{ij\dagger}\mathbf{R}^{ij}\mathbf{Q}^{ij} \tag{4.21}$$

$$\hat{\mathbf{R}}^{ij} = \mathbf{L}^{ij\dagger}\overline{\mathbf{R}}^{ij}\mathbf{L}^{ij} \tag{4.22}$$

Diagonalizing the virtual Fock block in the local basis provides the pair/orbital specific semicanonical basis:

$$\overline{\mathbf{F}}_V^{ij}\mathbf{L}^{ij} = \mathbf{L}^{ij}\hat{\mathbf{F}}_V^{ij} \tag{4.23}$$

where $\hat{\mathbf{F}}_V^{ij}$ is a diagonal matrix with entries $\hat{\epsilon}_a^{ij}$, $\hat{\epsilon}_b^{ij}$, $\ldots$, . Next, the energy denominators are applied, where the occupied energies are the diagonal elements of the occupied block of the fock matrix, and the virtual energies are in the specific pair/orbital semicanonical basis.

$$\hat{\Delta}_{ab}^{ij} = \frac{\hat{R}_{ab}^{ij}}{f_{ii} + f_{jj} - \hat{\epsilon}_a^{ij} - \hat{\epsilon}_b^{ij}} \tag{4.24}$$

The update in the semicanonical basis may then be backtransformed to the canonical basis

and the new amplitudes computed in the usual manner:

$$\mathbf{\Delta}^{ij} = \mathbf{Q}^{ij}\mathbf{L}^{ij}\hat{\mathbf{\Delta}}^{ij}\mathbf{L}^{ij\dagger}\mathbf{Q}^{ij\dagger} \tag{4.25}$$

$$\mathbf{T}^{ij}_{new} = \mathbf{T}^{ij}_{old} + \mathbf{\Delta}^{ij} \tag{4.26}$$

The local filter technique may be applied to singles,

$$\mathbf{\Delta}^{i} = \mathbf{Q}^{ii}\mathbf{L}^{ii}\hat{\mathbf{\Delta}}^{i}\mathbf{L}^{ii\dagger}\mathbf{Q}^{ii\dagger} \tag{4.27}$$

$$\mathbf{t}^{i}_{new} = \mathbf{t}^{i}_{old} + \mathbf{\Delta}^{i}, \tag{4.28}$$

and furthermore extended to the lambda and perturbed amplitude equations.

4.2.4 Computational Details

We present results that illustrate the performance of the OSV and PNO local correlation methods with coupled cluster linear response theory. Our test set includes a series of chiral hydrogen helices, fluoroalkanes, *S*-1-phenylethanol, (1*R*,4*R*)-norbornenone, and (1*R*,5*R*)-β-pinene. For some systems we also calculated results for the PAO approach for comparison. For the latter three molecules, we employed the CC2 method[138] while for the two series we used CCSD. For the polarizability and optical rotation calculations, the aug-cc-pVDZ basis set[123,139] was used.

To assess the extent of truncation in the local correlation calculations, we compare the

T_2 ratios between methods. These ratios are simply the number of doubles amplitudes in the truncated, local basis compared to the number of doubles amplitudes in the canonical molecular orbital basis.

For the OSV and PNO approaches, several occupation thresholds were tested. We used both the Boughton-Pulay domains[115] and coupled-perturbed Hartree Fock based domains[58] for the PAO results. All property values are calculated using the modified-velocity gauge[13] representation of the electric dipole operator. Additionally, three different types of truncation were examined. We explored the effects of truncating only the doubles (D) amplitudes, doubles and singles (D+S), and doubles with neglecting weak pairs (D+WP) where occupied pairs with an MP2 pair energy less than 1×10^{-4} E_h are dropped. For the sparsity tests, *vide infra*, the 6-31+G* split-valence basis set was selected.[122]

4.3 Results and Discussion

4.3.1 Sparsity: Simple Alkanes

In exploring and comparing the local correlation techniques, we desired to examine the relative sparsity of each local basis in addition to their performance in property calculations. For a set of four simple alkanes, we transformed their amplitudes into each local basis, examining them element by element to get a sense of the distribution of the amplitudes in each basis. The ground state or unperturbed amplitudes are obtained through the usual

projection equations,

$$\langle \phi | \bar{H} | \phi_0 \rangle = 0, \tag{4.29}$$

where ϕ is an excited determinant and $\bar{H}$ is the similarity transformed Hamiltonian. The perturbed amplitudes, also transformed to each local basis, are solved for via Eq. 4.3.

The four plots in Figure 4.1 present the distribution of the untruncated, converged unperturbed and perturbed amplitudes in each basis for ethane, butane, hexane and octane. As the alkane chain length increases, the distribution curves become smoother, which is to be expected as the number of amplitudes increases with the size of the molecule. In general, the perturbed amplitudes are less sparse than their ground state counterparts. For the PAO and OSV bases, the peak positions for the perturbed amplitude distributions are about an order of magnitude larger than the unperturbed case. For instance, the peaks for the OSV curves for hexane are around 10^{-5} and 10^{-4} for the unperturbed and perturbed amplitudes, respectively. Despite the similar degree of sparsity, the PAO curves are relatively flat compared to the OSV distributions. Again using hexane as an example, the perturbed PAO curve ranges from 10^{-8} to 10^{-2}, but the perturbed OSV distribution only goes from 10^{-6} to 10^{-2}.

For the PNO distributions, the peak shift between unperturbed and perturbed amplitudes is greater than for the OSV or PAO basis. The perturbed amplitudes are approximately two orders of magnitude less sparse than the ground state amplitudes (versus one order of magnitude for OSVs or PNOs). The peak position for the perturbed PNO curve for hexane,

for instance, is close to 10^{-5} compared to 10^{-7} for unperturbed PNO amplitudes. Also, both PNO distributions are shifted to the left relative to their OSV and PAO analogues. The peak positions for the perturbed PNO amplitudes for hexane are on par with the unperturbed amplitudes in the OSV and PAO bases at around 10^{-5}.

Figure 4.1: Wavefunction sparsity for a series of alkane chains: (a) ethane, (b) butane, (c) hexane, (d) octane.

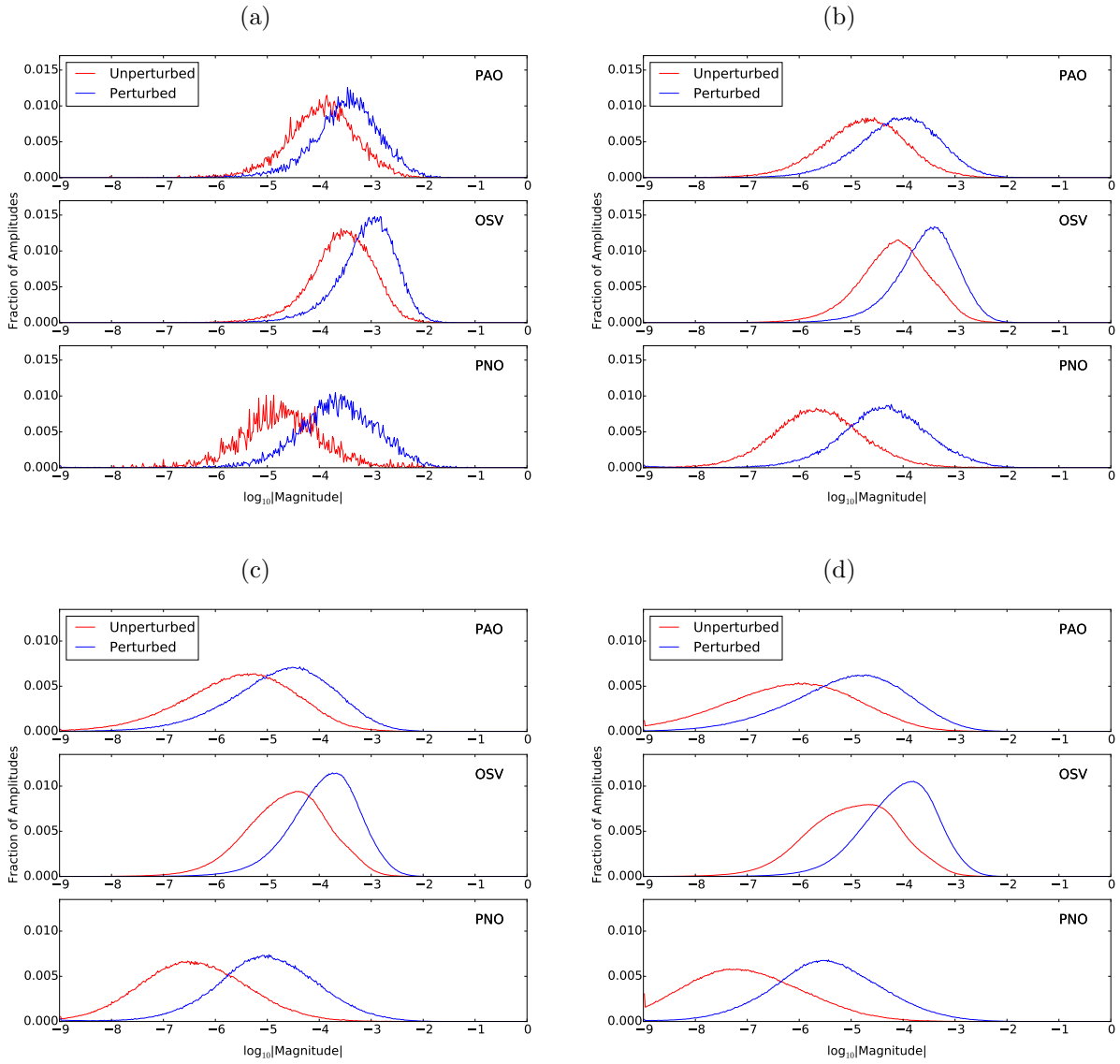

4.3.2 (P)-$(H_2)_n$ Helices

For the initial performance testing, we selected a simple and straightforward test set - (P)-$(H_2)_n$ helices. These hypothetical systems have been used previously in probing local correlation techniques,[58] but only the PAO approach has been tested. The weak, non-bonding interactions between hydrogen dimers make these chains easy to treat via local correlation techniques. Furthermore, a relatively large helix length may be tested easily due to the small size of the molecules (H!), and these systems should be a best case scenario for the local methods.

Figure 4.2 contains a series of plots with polarizabilities, optical rotations, and T_2 ratios for the hydrogen helices $(H_2)_2$ and $(H_2)_7$ computed at the CCSD level with the aug-cc-pVDZ basis set. As in other cases, *vide infra*, the convergence of the OSV and PNO polarizabilities is well-behaved (does not oscillate or cross canonical value) as we tighten the truncation threshold. The optical rotations, on the other hand, appear oscillatory but do converge to the canonical result as we approach the full virtual space. For $(H_2)_2$, the OSV and PNO curves cross the canonical result several times, but the curves for the longer helix $(H_2)_7$ only cross twice. This oscillating behavior is a result of positive and negative contributions inherent in the optical rotation tensor. As a result, fortuitous error cancellation arises for these ideal systems at looser thresholds. For $(H_2)_2$, the rotations are more accurate at 10^{-6} than the 10^{-8} threshold, and a similar scenario is seen for $(H_2)_7$ for the 10^{-4} and 10^{-5} cutoffs.

Additionally, dispersion curves have been generated for $(H_2)_7$ with values calculated at 355, 436, 589, and 633 nm, shown in Figure 4.3. For all the cutoffs, it is apparent that neither of

Figure 4.2: $(H_2)_n$ - Ideal test cases. Polarizabilities, optical rotations, and T_2 ratios for two hydrogen dimer helices are plotted against the $-log$(occupation threshold) used in the local calculations. The property values for the canonical, untruncated calculation (CANON) are plotted in yellow.

(a)

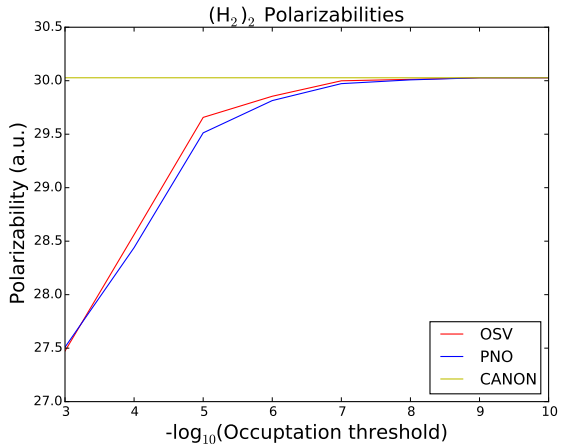

(b)

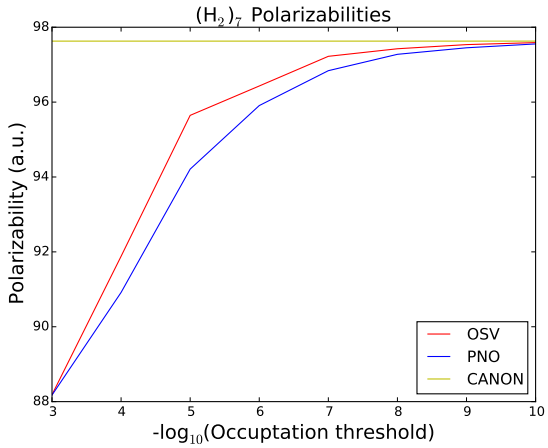

(c)

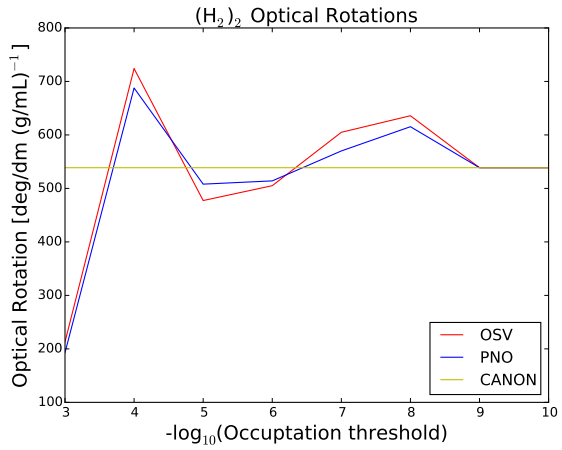

(d)

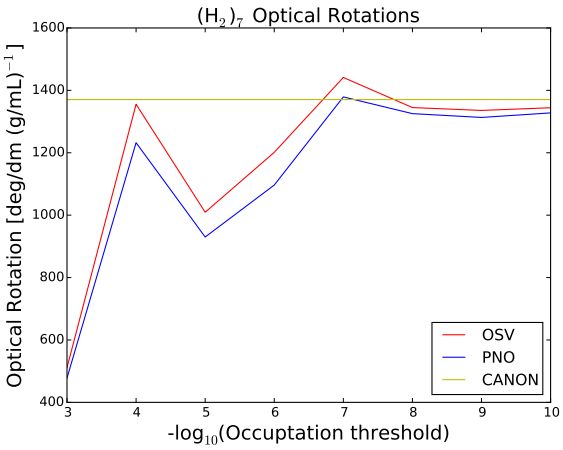

Figure 4.2: $(H_2)_n$ - Ideal test cases. Polarizabilities, optical rotations, and T_2 ratios for two hydrogen dimer helices are plotted against the $-log$(occupation threshold) used in the local calculations. The property values for the canonical, untruncated calculation (CANON) are plotted in yellow.

(e) (f)

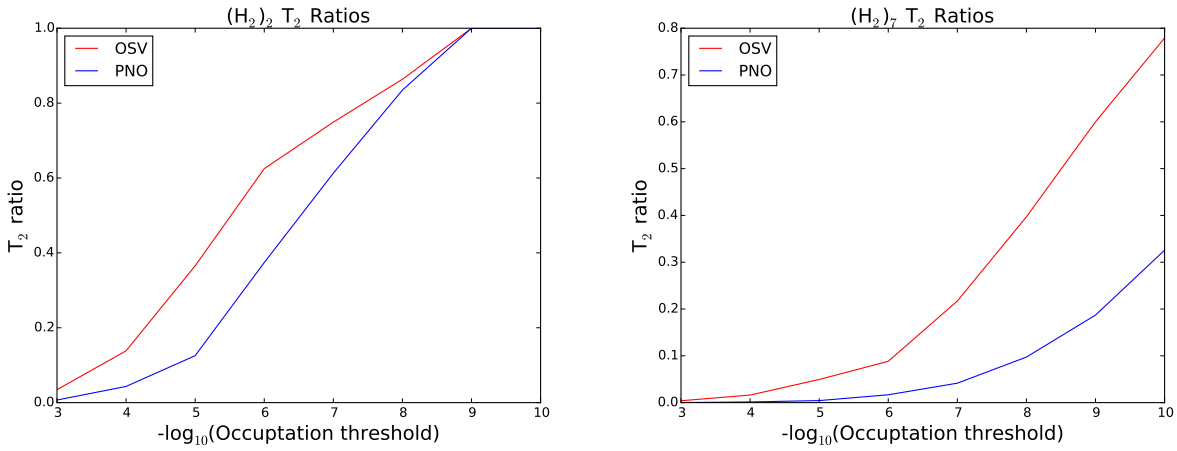

the local methods deteriorates drastically across the range of these wavelengths; although, at higher-energy wavelengths, the local methods tend to perform slightly worse.

4.3.3 (M)-1-fluoroalkanes

The linear, chainlike fluoroalkanes serve as a next step in testing local correlation methods. Like the hydrogen dimer helices, these molecules have a one-dimensional structure, but are much larger and more complex. In addition, we have moved from non-bonding to bonding interactions. However, the intramolecular interactions are limited by the structure and increase only linearly, making them prime candidates for taking advantage of local correlation techniques. As noted in previous studies,[58,59] while these systems have zero optical rotation

Figure 4.3: $(H_2)_7$ - Dispersion curves for various truncation thresholds. The number N in parentheses represents the occupation cutoff 10^{-N}.

(a)

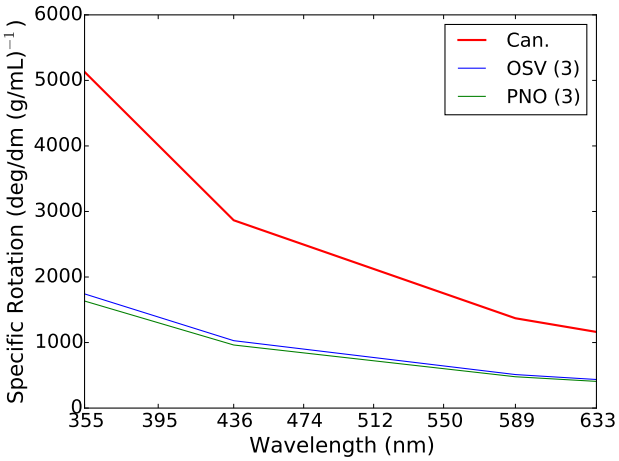

(b)

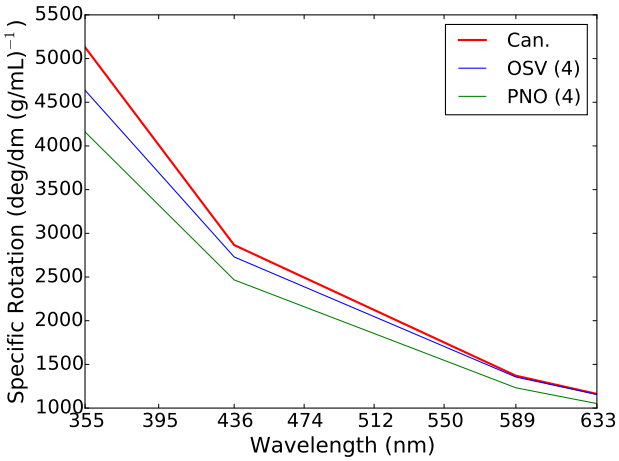

(c)

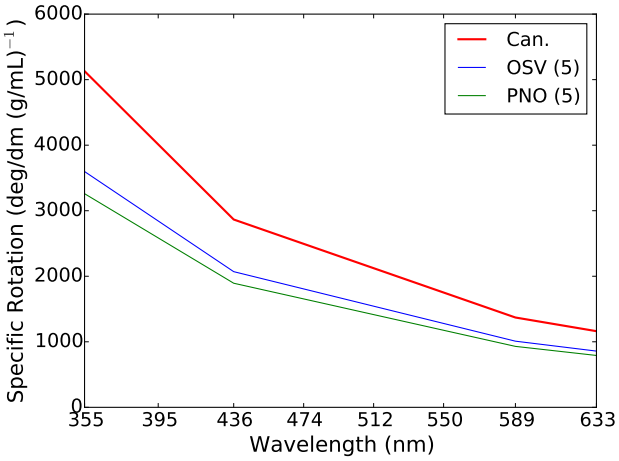

(d)

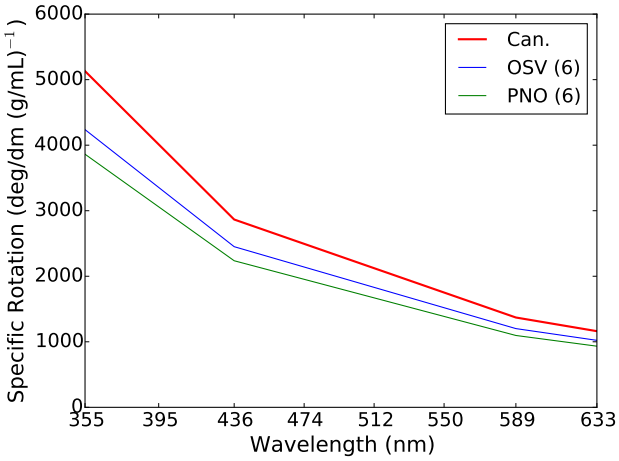

Figure 4.3: $(H_2)_7$ - Dispersion curves for various truncation thresholds. The number N in parentheses represents the occupation cutoff 10^{-N}.

(e)

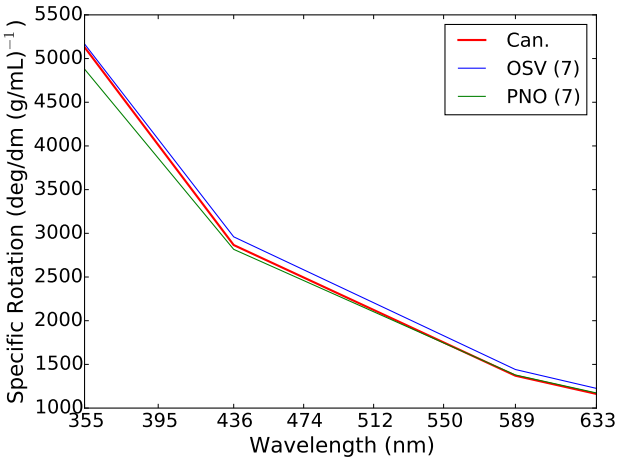

(f)

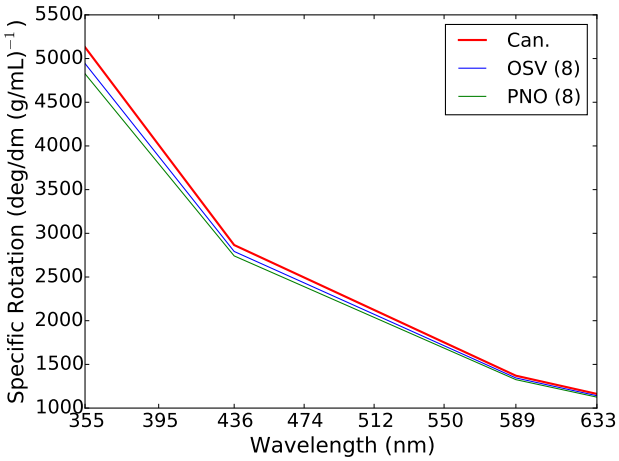

(g)

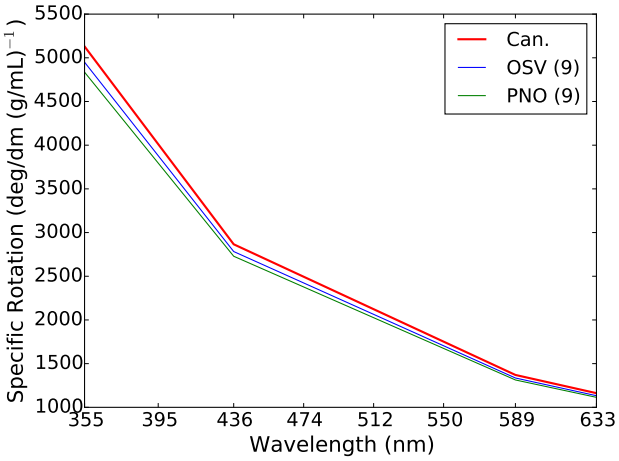

(h)

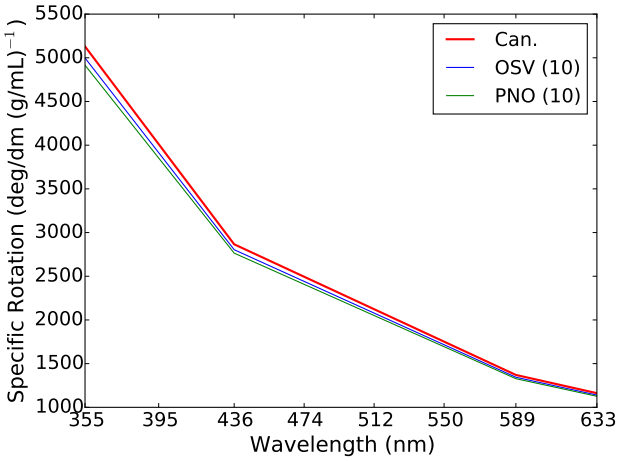

due to conformational averaging, we select a single, optically active conformer with a negative F-C_1-C_2-C_3 dihedral angle. The fluoroalkanes may be assigned as having (M) axial chirality by looking straight down the bond axis of C1 and C2; moving counter-clockwise we encounter first the fluorine atom, then the third carbon atom (C3) in the chain, resulting in (M)-fluoroalkanes. Unlike earlier works featuring this test set, we limit our investigation to the aug-cc-pVDZ basis set only. While basis set effects are considerable in response calculations, diffuse functions have been shown to be essential for accurate results.[3] Also, for fluoropentane, the 6-31+G* and aug-cc-pVDZ basis sets yielded similar localization errors in a previous study.[59]

Table 4.1: CCSD/aug-cc-pVDZ polarizabilities for a series of (M)-fluoroalkanes at 589 nm. Atomic units are used.

		OSV				PNO				PAO			
	Canonical	10^{-6}		10^{-7}		10^{-6}		10^{-7}		BP		CPHF (0.10)	
Molecule	α	α	T_2 Ratio	α	T_2 Ratio	α	T_2 Ratio	α	T_2 Ratio	α	T_2 Ratio	α	T_2 Ratio
1-fluoropropane	121.9	118.6	0.107	120.2	0.218	116.6	0.0180	119.1	0.0559	120.0	0.182	121.9	1.22
1-fluoropentane	195.8	190.0	0.0497	192.7	0.105	186.6	0.00594	190.8	0.0198	192.3	0.0901	195.8	1.10
1-fluoroheptane	271.0	262.4	0.0284	266.4	0.0628	257.4	0.00264	263.7	0.00910	265.7	0.0534	271.0	1.01

Table 4.2: CCSD/aug-cc-pVDZ optical rotations for a series of (M)-fluoroalkanes at 589 nm. Units are in deg dm^{-1} (g/mL)$^{-1}$.

		OSV				PNO				PAO			
	Canonical	10^{-6}		10^{-7}		10^{-6}		10^{-7}		BP		CPHF (0.10)	
Molecule	$[\alpha]_D$	$[\alpha]_D$	T_2 Ratio	$[\alpha]_D$	T_2 Ratio	$[\alpha]_D$	T_2 Ratio	$[\alpha]_D$	T_2 Ratio	$[\alpha]_D$	T_2 Ratio	$[\alpha]_D$	T_2 Ratio
1-fluoropropane	-60.8	-53.6	0.107	-55.4	0.218	-49.1	0.0180	-55.3	0.0559	-44.3	0.182	-60.6	1.23
1-fluoropentane	-50.2	-45.2	0.0497	-46.1	0.105	-41.0	0.00594	-44.5	0.0198	-39.8	0.0901	-50.1	1.10
1-fluoroheptane	-40.5	-36.5	0.0284	-37.0	0.0628	-32.6	0.00264	-35.7	0.00910	-32.4	0.0534	-40.5	1.06

Tables 4.1-4.2 show data at 589 nm for polarizabilities and optical rotations, respectively, of the three fluoroalkanes. For the polarizabilities, the highest magnitude error arises for fluoroheptane with the PNO method with an occupation threshold of 10^{-6} - around 5%. However, the fraction of local T_2 amplitudes relative to canonical amplitudes is quite small at around 0.003. The LOSV and LPNO results appear to be more accurate at a given cutoff for fluoropropane and fluoropentane than for fluoroheptane. However, the virtual space for the shorter fluoroalkanes is less truncated compared to fluoroheptane, resulting in smaller localization errors. For instance, the T_2 ratio for fluoropropane with OSV (10^{-6}) is 0.107, while for fluoroheptane at the same method and cutoff is 0.0284. For these systems, the PAO approach yields accurate (around 2% error) polarizabilities with favorable T_2 ratios for the BP domains. The CPHF-based domains return the entire virtual space, and agree exactly with the canonical result. The T_2 ratios for the CPHF domains are larger than 1, which may be explained by the fact that the full PAO virtual space is the same as the number of atomic orbitals. Since the number of atomic orbitals exceeds the number of canonical virtuals, the T_2 ratios will be larger than 1 when the full PAO virtual space is retained.

The relative errors for the optical rotations for the fluoroalkanes are an order of magnitude larger than for polarizabilities. While the local polarizabilities were within a few percent of the canonical result, the errors for the local rotations range from around 10%-30% (excluding results for the PAO approach with CPHF-based domains). Also, the OSV and PNO methods outperform the PAO method with BP domains. At both occupation thresholds, the OSV and PNO rotations more closely agree with the canonical result with smaller T_2 ratios than

the PAO/BP values.

4.3.4 *S*-1-phenylethanol

Stepping away from linear structures, we next examined the aromatic compound *S*-1-phenylethanol, which features delocalized interactions because of the presence of the phenyl ring. For this system, we also tabulated results incorporating additional truncation measures, which of course would become necessary for a significantly reduced-scaling method. The three data sets for *S*-1-phenylethanol include results where only the doubles amplitudes have been truncated (D), doubles truncated and weak pairs neglected (D+WP), and lastly both doubles and singles truncated (D+S).

Local CC2 polarizabilities for *S*-1-phenylethanol are given in Table 4.3. For the doubles-only truncation, the OSV (10^{-8}) and PNO (10^{-10}) methods give encouraging results. Both have errors of less than 2% with very reasonable T_2 ratios: 0.236 for OSV and 0.248 for PNO. The polarizabilities for *S*-1-phenylethanol seem especially sensitive to truncation of the singles amplitudes. While the D+S results for both methods converge to the canonical result as we tighten the occupation threshold, at the loosest cutoff they are nearly half (in magnitude) of the canonical result.

The D+WP polarizability for the OSV method at the tightest cutoff, 10^{-12}, is comparable to the OSV(D) value at 10^{-8}, yielding 320.2 and 320.5 a.u., respectively. However, the T_2 ratio is approximately doubled, 0.593 for D+WP vs. 0.236 for D only. This higher ratio

is expected because of the tighter threshold, but the closeness in polarizabilities seems to suggest that the OSVs may yield equivalent results at a looser threshold if weak pairs are not neglected. Nonetheless, the difference in these two values amounts to less than a percent, and both the OSV/D and D+WP at the tighter three cutoffs have very little error. Similar conclusions may be drawn for the PNO method.

Table 4.3: CC2/aug-cc-pVDZ polarizabilities for *S*-1-phenylethanol at 589 nm. Atomic units are used.

	OSV						PNO					
	D		D+WP		D+S		D		D+WP		D+S	
Cutoff	α	T_2 Ratio	α	T_2 Ratio	α	T_2 Ratio	α	T_2 Ratio	α	T_2 Ratio	α	T_2 Ratio
10^{-4}	274.3	0.00330	278.9	0.00204	160.5	0.00330	265.3	0.000239	270.1	0.000239	155.3	0.000239
10^{-6}	307.0	0.0442	304.1	0.0288	258.7	0.0442	297.3	0.00574	295.4	0.00550	252.8	0.00574
10^{-8}	320.5	0.236	316.2	0.160	303.7	0.236	316.0	0.0535	312.3	0.0465	301.1	0.0535
10^{-10}	324.4	0.728	319.6	0.467	320.0	0.728	322.8	0.248	318.3	0.181	319.1	0.248
10^{-12}	325.0	0.974	320.2	0.593	324.1	0.974	324.7	0.644	319.9	0.415	323.9	0.644
Canonical	325.1											

For the specific rotations, collected in Table 4.4, the errors are larger than for polarizabilities. For example, at the 10^{-6} cutoff, the PNO(D) polarizability is in error by about 9%, but the PNO(D) rotation is off by nearly 39%. Neglecting weak pairs in the rotation calculations has a noticeable effect. The D+WP results compare very poorly to the canonical result for both LOSV and LPNO. Even at a moderate threshold, 10^{-8}, the D+WP values overshoot (in magnitude) the canonical rotation. Due to cancellation of error, the OSV(D+WP) and PNO(D+WP) are best at the looser cutoffs of 10^{-6} and 10^{-8}, respectively. The D+S results are also especially poor at the loosest cutoff (10^{-6}), being around 50% of the D values for the same cutoff, but at least they approach the canonical rotation as the virtual space is expanded, unlike the D+WP values. The lack of convergence to the canonical result is to

be expected for the D+WP truncation though (and their T_2 ratios will never converge to 1 either); weak pairs are ignored based on an energy cutoff separate from the occupation cutoff used for the virtual space. Thus, even with no truncation of the virtual space, D+WP values will still be in error by some amount.

Table 4.4: CC2/aug-cc-pVDZ optical rotations for *S*-1-phenylethanol at 589 nm. Units are in deg dm^{-1} $(g/mL)^{-1}$.

	OSV						PNO					
	D		D+WP		D+S		D		D+WP		D+S	
Cutoff	$[\alpha]_D$	T_2 Ratio	$[\alpha]_D$	T_2 Ratio	$[\alpha]_D$	T_2 Ratio	$[\alpha]_D$	T_2 Ratio	$[\alpha]_D$	T_2 Ratio	$[\alpha]_D$	T_2 Ratio
10^{-6}	-128.5	0.0422	-158.0	0.0288	-72.8	0.0422	-101.2	0.00574	-130.4	0.00550	-61.5	0.00574
10^{-8}	-150.1	0.236	-182.4	0.160	-107.8	0.236	-142.2	0.0535	-175.1	0.0465	-106.7	0.0535
10^{-10}	-160.9	0.728	-192.7	0.467	-127.9	0.728	-156.7	0.248	-189.7	0.181	-126.8	0.248
10^{-12}	-164.3	0.974	-195.4	0.593	-164.5	0.974	-162.7	0.644	-194.0	0.415	-163.1	0.644
Canonical	-165.2											

In order to get a better grasp on the comparison of the performances of the different truncation schemes, the polarizabilities and optical rotations for *S*-1-phenylethanol have been plotted against their T_2 ratios in Figures 4.4-4.5. In each plot, the black bold horizontal line represents the full, canonical result for the property. For the polarizabilities, the PNO method appears to outperform the OSV approach. For each truncation (D, D+WP, D+S), the associated PNO curve is closer to the canonical result than the corresponding OSV plot. While OSV(D+S) exhibits the largest deviation from the canonical result, the PNO(D+S) curve is nearly on par with the OSV results. The comparison between PNO(D) and OSV(D) is reflected in the D+WP curves, but dropping weak pairs shifts the plots - yielding higher errors and converging to a value other than the canonical result. When up to 20% of the doubles amplitudes are retained, the D+WP results are superior to D+S polarizabilities. However, when less truncation is enforced, the PNO(D+S) surpasses the D+WP results,

Figure 4.4: CC2/aug-cc-pVDZ polarizability data for *S*-1-phenylethanol.

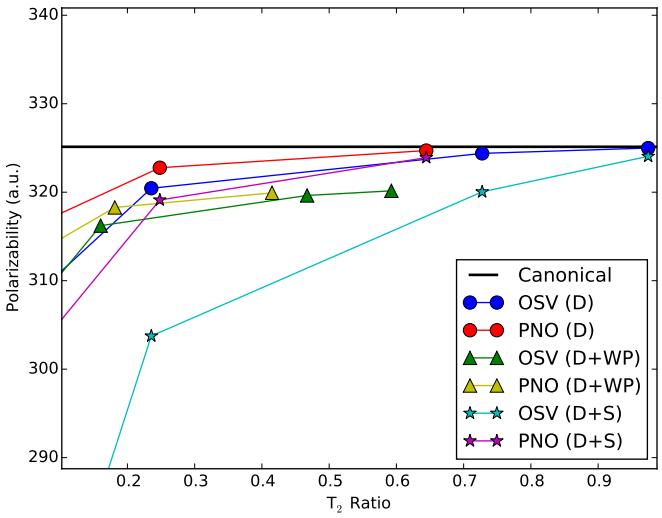

while OSV(D+S) remains clearly the largest in error except for at the tightest occupation cutoffs.

We can see immediately, in Figure 4.5, that the truncation variants more strongly influence the quality of local optical rotations, since the plots for the different schemes (e.g. D vs D+WP) are more spaced out relative to the polarizability curves. Furthermore, the rotation curves demonstrate different trends for the various truncations. D+S values easily overestimate the optical rotation, while D+WP underestimate it. The D values fall in between, approaching the canonical rotation from above. As in polarizabilities, the PNO(D) and PNO(D+S) outperform their OSV counterparts. Also, the OSV values appear significantly more sensitive to truncation of singles compared to PNO(D+S). The D+WP curves for both methods again illustrate how neglecting weak pairs essentially shifts the computed property value, and they fail to converge to the canonical result. At the highest truncation levels the

Figure 4.5: CC2/aug-cc-pVDZ optical rotations for *S*-1-phenylethanol.

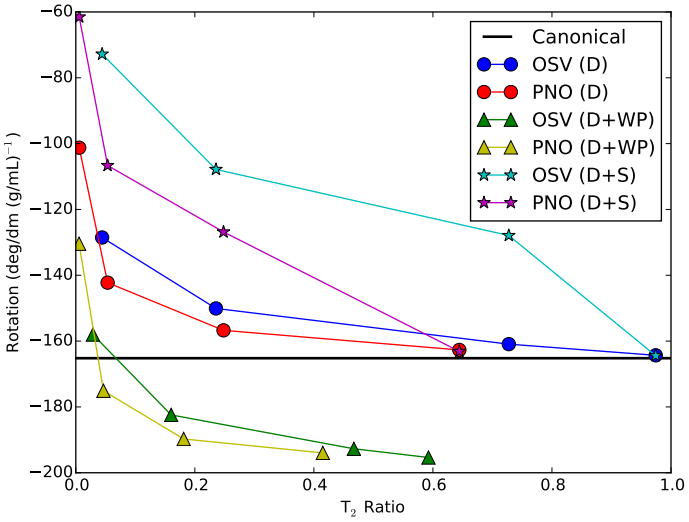

D+WP yield the most accurate results compared to D and D+S; however, this is due to cancellation of error.

4.3.5 (1*R*,4*R*)-norbornenone

The cage-like (1*R*,4*R*)-norbornenone presents a three-dimensional test case and features not one but two chiral centers. The notorious molecule several times has been featured in theoretical studies of optical properties.[6,16,76,85,140–142] One of the reasons for the large amount of interest given to norbornenone is due to its surprisingly large optical rotation. In a study by Caricato et al., similar molecules such as (1*R*,4*S*)-norcamphor and (1*S*,4*R*)-6-methylene-2-norbornanone yielded B3LYP/aug-cc-PVDZ rotations at 355 nm of 124 and -312 deg dm^{-1} (g/mL)$^{-1}$, respectively; for (1*S*,4*S*)-norbornenone, the predicted optical rotation at

the same wavelength and level of theory is a notably larger (in magnitude) -12417 deg dm^{-1} (g/mL)$^{-1}$.[142] Reasons for the high magnitude rotation have been attributed to delocalization interactions between the carbonyl and C=C bond[141] along with the low energy $n \rightarrow \pi^*$ excited state transition.[142]

Table 4.5 contains LOSV and LPNO polarizabilities at several thresholds and truncation schemes for (1*R*,4*R*)-norbornenone. For the values where only the doubles amplitudes are truncated, the methods provide accurate values at an occupation threshold of 10^{-8}, with favorable T_2 ratios: 0.255 for LOSV and 0.076 for LPNO. At this cutoff, the LOSV value is off by 1.83% from the canonical value compared to LPNO (3.00%). For both methods at the loosest threshold, the error increases by less than 1% when weak pairs are neglected in addition to truncating the doubles. A larger error is seen when both singles and doubles are truncated - several times more than D+WP.

Table 4.5: CC2/aug-cc-pVDZ polarizabilities for (1*R*,4*R*)-norbornenone at 589 nm. Atomic units are used.

	OSV						PNO					
	D		D+WP		D+S		D		D+WP		D+S	
Cutoff	α	T_2 Ratio	α	T_2 Ratio	α	T_2 Ratio	α	T_2 Ratio	α	T_2 Ratio	α	T_2 Ratio
10^{-6}	241.4	0.050	240.3	0.041	201.3	0.050	234.9	0.007	234.4	0.007	197.9	0.007
10^{-8}	252.2	0.255	250.5	0.216	237.2	0.255	249.1	0.076	247.6	0.0692	235.7	0.0763
10^{-10}	256.2	0.907	254.0	0.739	251.3	0.907	254.8	0.389	252.8	0.332	250.8	0.389
10^{-12}	256.7	0.987	254.5	0.792	255.8	0.987	256.6	0.863	254.3	0.705	255.7	0.863
Canonical	256.9											

The local optical rotation values for (1*R*,4*R*)-norbornenone, shown in Table 4.6, suffer much worse when dropping weak pairs and truncating singles. Due to the poor performance of D+WP and D+S truncations for *S*-1-phenylethanol rotations, we elected to perform

the associated D+WP and D+S calculations for (1*R*,4*R*)-norbornenone at only the tighter cutoffs. For both LOSV and LPNO, the tightest threshold D+WP values (10^{-13}) are still worse than the D-only values at the loosest (10^{-8}) cutoff. Also, only at the tightest cutoff do the D+S results begin to closely agree with the D-only values (and the canonical result). Even at tight cutoffs and with little savings (high T_2 ratios), the quality of the D+S values can be rather poor. In general, much like for the fluoroalkanes and *S*-1-phenylethanol, the optical rotations are much more sensitive to truncation (for all methods) compared to polarizabilities.

Table 4.6: CC2/aug-cc-pVDZ optical rotations for (1*R*,4*R*)-norbornenone at 589 nm. Units are in deg dm^{-1} $(g/mL)^{-1}$.

	OSV						PNO					
	D		D+WP		D+S		D		D+WP		D+S	
Cutoff	$[\alpha]_D$	T_2 Ratio	$[\alpha]_D$	T_2 Ratio	$[\alpha]_D$	T_2 Ratio	$[\alpha]_D$	T_2 Ratio	$[\alpha]_D$	T_2 Ratio	$[\alpha]_D$	T_2 Ratio
10^{-8}	673.8	0.255	-	-	-	-	531.1	0.076	-	-	-	-
10^{-9}	770.1	0.559	-	-	-	-	685.6	0.190	-	-	-	-
10^{-10}	789.9	0.907	-	-	-	-	756.9	0.389	-	-	-	-
10^{-11}	807.9	0.976	516.6	0.781	704.0	0.976	795.4	0.645	513.2	0.536	700.1	0.645
10^{-12}	813.6	0.987	518.8	0.792	772.3	0.987	808.5	0.863	516.5	0.705	771.5	0.863
10^{-13}	816.5	0.994	520.1	0.799	804.8	0.994	815.3	0.976	519.3	0.789	804.7	0.976
Canonical	817.6											

In Figures 4.6-4.7, the properties for each method and scheme are plotted against their T_2 ratios. For the polarizabilities, the PNO(D) values are once again in slightly better agreement with the canonical result than OSV(D) at a given T_2 ratio. Neglecting weak pairs for (1*R*,4*R*)-norbornenone has a minor effect on the polarizabilities, which become more evident as the virtual space is increased and the curves fall short of the canonical value. Truncating the single introduces the largest amount of error in the polarizabilities, especially for the OSV method.

Figure 4.6: CC2/aug-cc-pVDZ polarizability data for (1*R*,4*R*)-norbornenone computed at 589 nm.

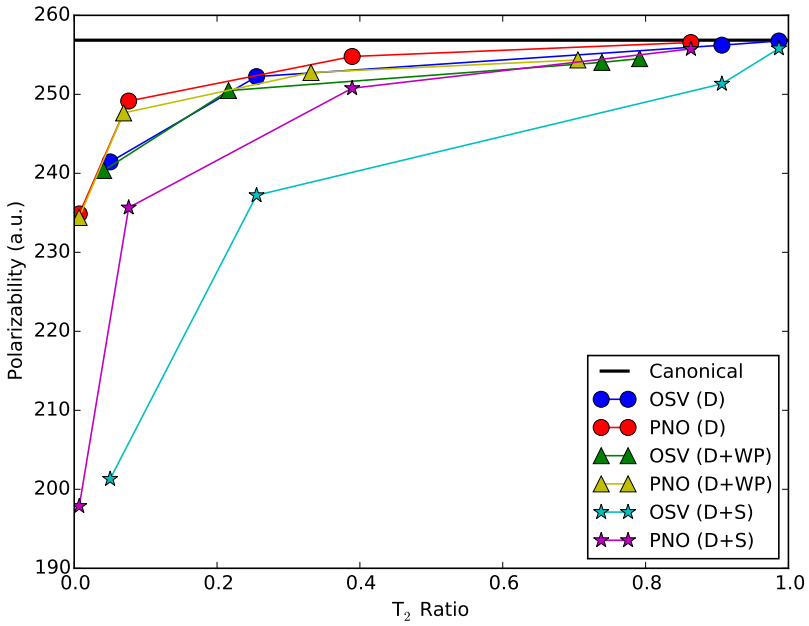

Figure 4.7: CC2/aug-cc-pVDZ optical rotation data for (1*R*,4*R*)-norbornenone computed at 589 nm.

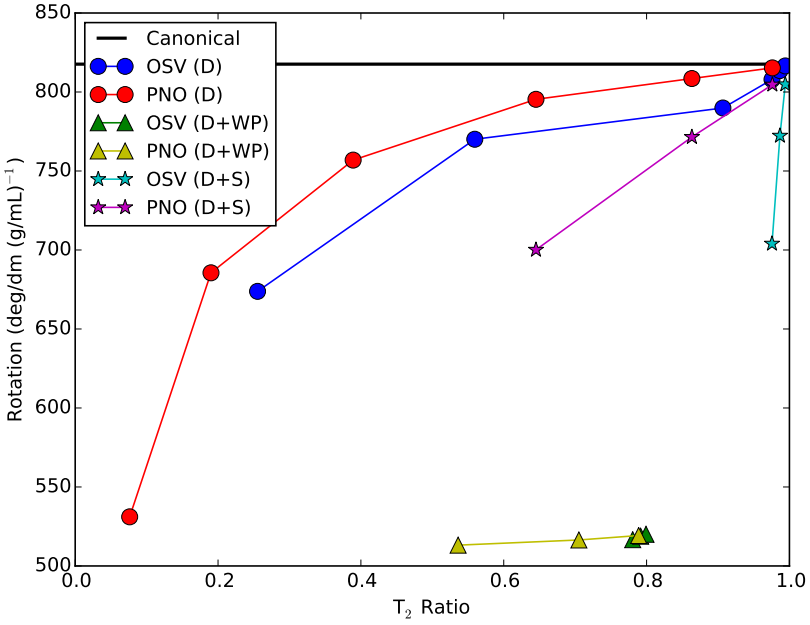

Similarly to *S*-1-phenylethanol, the optical rotation curves in Figure 4.7 display much higher errors compared to polarizabilities. For (1*R*,4*R*)-norbornenone, however, the error is worst when weak pairs are neglected. Even with T_2 ratios above 50%, the D+WP curves are in no better agreement than the PNO(D) method at the loosest cutoff where under 10% of the doubles are retained. However, the error is relatively constant for the D+WP data. While the errors for D+S values are smaller than D+WP, they grow rapidly as the truncation is increased. In fact, the OSV(D+S) curve is nearly vertical, and the PNO(D+S) performance deteriorates much more quickly than OSV(D) or PNO(D).

4.3.6 (1*R*,5*R*)-β-pinene

Our last test case is the cage-like molecule (1R,5R)-β-pinene. Like (1R,4R)-norbornenone, (1R,5R)-β-pinene contains two chiral centers and is rife with intramolecular interactions. However, unlike (1R,4R)-norbornenone, (1R,5R)-β-pinene has a relatively small reported optical rotation,[143,144] making it especially important to be able to confidently predict the sign of the property. β-pinene has previously received much attention from theoretical studies of chiral properties largely because of discrepancies between theory and experiment.[58,59,76,85,143–147] Polarizability and optical rotations for (1R,5R)-β-pinene at 589 nm for the simplest truncation scheme (only doubles truncated), are plotted for four cutoffs in Figures 4.8-4.9. For the polarizabilities, as we decrease the level of truncation, both the PNO and OSV curves quickly approach the canonical result. The PNO methods seems to slightly outperform the OSV approach - more closing approaching the canonical result at a given T_2 ratio. However, the differences in percent error for the two methods are rather small.

The optical rotation plots in Figure 4.9 show much higher localization errors for the local methods than polarizabilities. At small T_2 ratios, both methods predict the incorrect sign for the optical rotation. As the virtual space is increased, both local approaches quickly recover the correct sign. However, the error is still relatively high at moderate truncation. When the T_2 ratio is around 0.5, the errors of both methods are around 50%. Similar to polarizabilities, the PNO results agree the best with the canonical result at a given T_2 ratio, while the error is only marginally larger for the OSV method.

Figure 4.8: CC2/aug-cc-pVDZ polarizability data for (1R,5R)-β-pinene computed at 589 nm.

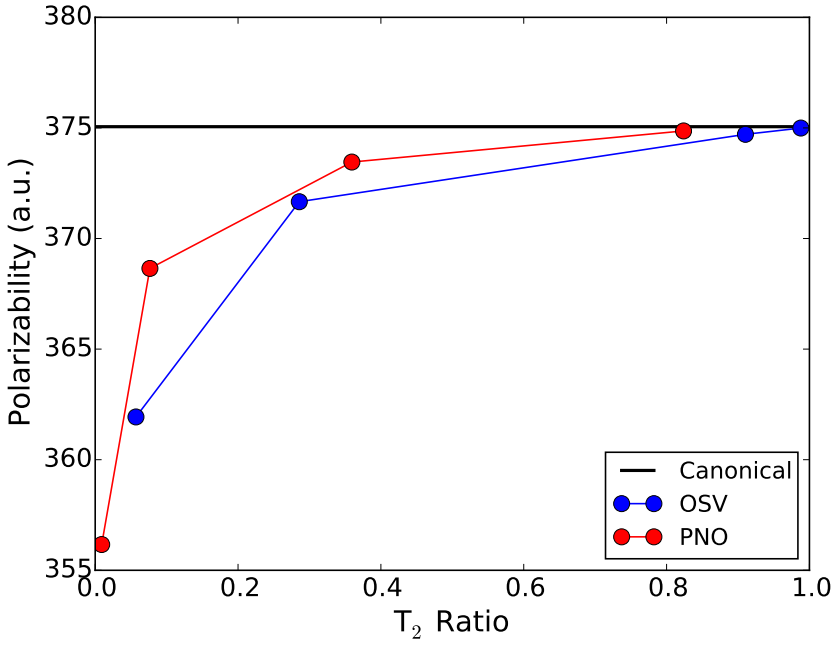

Figure 4.9: CC2/aug-cc-pVDZ optical rotations for (1R,5R)-β-pinene computed at 589 nm.

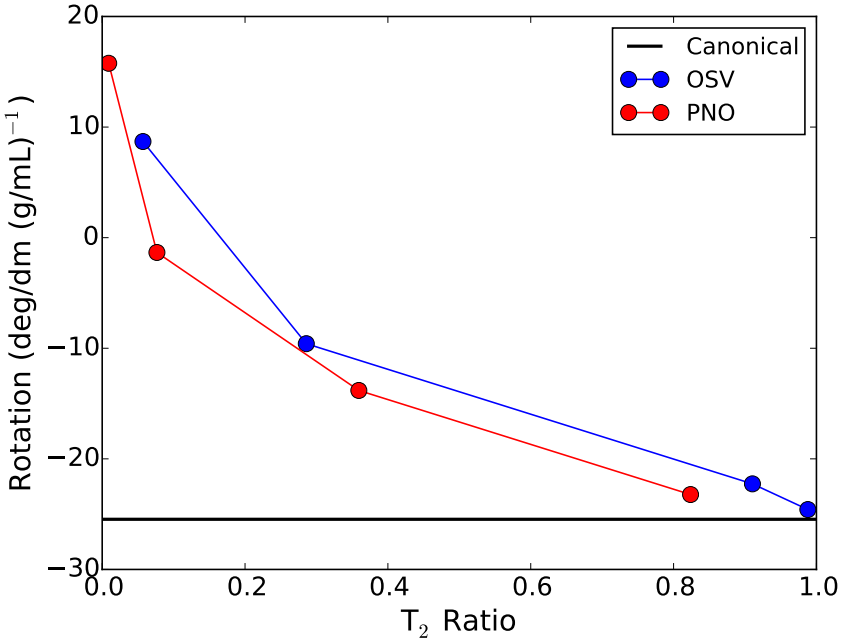

4.4 Conclusions

We have explored the performance of the OSV and PNO local correlation approaches to several test cases for optical properties. For select systems, the PAO approach data was also tested for comparison. Furthermore, we applied and compared additional truncation measures as would be necessary for a production level reduced-scaling implementation of these methods.

For simple alkane chains, distribution plots of the unperturbed (ground state) and perturbed doubles amplitudes illustrate that the perturbed wavefunction is less sparse, having larger magnitude values. For the PNO method, the separation in distributions between unper-

turbed and perturbed amplitudes is greater than for OSV or PAO by about an order of magnitude. Also, the amplitudes in the PNO basis are the most sparse. The PAO and OSV distributions have similar peak positions, but the OSV basis results in the narrowest distribution, while the the curves for the PAO basis are somewhat broad.

For chiral $(H_2)_2$ and $(H_2)_7$ helices, we plotted OSV and PNO polarizabilities and optical rotations for several occupation thresholds. For both methods, the values approach the canonical result as the threshold is tightened (and the complete virtual space approached). For a given occupation cutoff, the OSV method retains more of the virtual space compared to PNOs. Dispersion curves for the two helices at several cutoffs show that the local methods may be applied across a range of wavelengths.

The OSV and PNO approaches, along with the PAO method, perform well for the one-dimensional fluoroalkanes. For a given occupation threshold or domain cutoff, the amount of truncation increases with the size of the system. For these systems, the PNO method often has the largest error, but the percent differences between methods is small. Also, the results for the PNO method are the most truncated (smallest T_2 ratios), which must be considered when comparing the performances between methods. For fluoroheptane, the OSV and PNO rotations at the 10^{-6} cutoff agree more closely to the canonical result than PAO with BP domains, but have smaller virtual spaces.

For *S*-1-phenylethanol, we focused on the PNO and OSV methods and extended our analysis to three different truncation schemes. For both properties, the most accurate results are achieved when only the doubles amplitudes are truncated, with the PNO results in better

agreement than the OSV method by a few percent. The OSV method, for this test case, is highly sensitive to singles truncation, with OSV(D+S) yielding the largest errors. Neglecting weak pairs introduces little error for polarizabilities for *S*-1-phenylethanol. For optical rotations, dropping insignificant pairs shifts the data so that the D+WP values are more accurate at higher truncations, but only through fortuitous cancellation of data.

(1*R*,4*R*)-norbornenone, another three-dimensional test case, is a challenging system. Local polarizabilities, for all the schemes, perform fairly well. The D+S results give the largest error for polarizabilities, and the OSV accuracy is more susceptible to truncation of the singles than PNO. Only the doubles truncation data performs well for the optical rotations, but errors are relatively higher than for polarizabilities. Neglecting weak pairs introduces the largest error, but is constant across a range of truncation. When singles are truncated, the quality of the optical rotation quickly decays as the truncation is increased.

For the molecule (1*R*,5*R*)-β-pinene, looking at only the doubles truncation scheme, the polarizabilities have relatively little error at high truncation - less than 10% error at T_2 ratios also under 10%. For the optical rotations, unfortunately, the wrong sign is predicted at high truncation levels. The correct sign is recovered at relatively small T_2 ratios, but the error remains large until the virtual space is nearly complete.

In conclusion, optical rotations are more sensitive to OSV and PNO truncation than polarizabilities. As the structural complexity of the system increases, the local methods are less effective at truncating the virtual space while maintaining high accuracy. Additional reduced-scaling measures, such as neglecting weak pairs, can introduce large amounts of error

in the property predictions. Polarizabilities and optical rotations are especially influenced by the PNO and OSV truncation of singles amplitudes. In order to achieve high accuracy at high truncation levels, other methods and approaches need be developed.

Chapter 5

Excited State Transition Properties with Reduced-Scaling Equation-of-Motion Coupled Cluster Theory

5.1 Introduction

Coupled cluster theory is a powerful wavefunction-based quantum chemical method for computing molecular properties.[2–7,10,12,148] One attractive feature for the method is its capacity for systematic improvement by including higher and higher excitation levels in the expo-

nential expansion. Coupled cluster singles and doubles (CCSD), for example, is restricted to only include singly and doubly substituted determinants. As the wavefunction is expanded to include higher substitutions, though, the associated computational cost grows rapidly.[18–24] For the CCSD method, after clever factorization of the amplitude equations, the method still scales on the order of $\mathcal{O}(N^6)$, where N is some measure of the system size. When pursuing coupled cluster level properties beyond the correlation energy, the cost is exacerbated by solving for additional wavefunction parameters, such as the left-hand coupled cluster wavefunction and left- and right-hand excited state amplitudes. Fortunately, a multitude of techniques have been developed to address the high-cost of such calculations, including localized orbital methods, fragmentation schemes, and more, such that larger and more complex chemical systems may be studied using these methods.[25–53]

Several of these methods have been applied to coupled cluster level calculations of excited state data.[102–105,131–133] The local technique that has received the most attention in regards to excited states[102–105] is the projected atomic orbital approach of Pulay, which involves assigning subsets of the virtual space to local occupied orbital or orbital pairs.[25] The orbital specific virtual (OSV)[49,50] and pair natural orbital (PNO)[43,44] local correlation methods follow a similar scheme, and have also seen use in excited state calculations.[132,133] Other methods follow a different formula, partitioning or fragmenting the molecular into a set of smaller calculations.[131]

One of the first efforts to use local correlation techniques for excited states was put forth by Crawford and King, who applied the PAO method in the context of equation-of-motion

coupled cluster (EOM-CC) calculations of singlet excitation energies.[102] They also explored effects of weak pair truncations and implemented a CIS(D) doubles correction for the excitation energies. In order to treat both the ground and excited state wavefunction in an even manner, the same domain structures were maintained for both the ground and excited states. With sufficiently flexible basis sets, including Rydberg functions, the local-EOM-CC (L-EOM-CC) results were found to be in good agreement with the canonical transition energies - in error by less than 0.2 eV. They stressed the importance of proper domain construction and discussed potential issues for excitations that are non-local in nature, such as charge transfer transitions.

Korona and Werner also used EOM-CCSD with the PAO method, but unlike Crawford and King they tailored the orbital domains to be different for each desired excited state since the virtual space necessary for the excited states may differ from that of the ground state (and each other).[103] In an analogous manner, they also defined different pair hierarchies for the ground and excited states. While their state-specific local approach required them to keep track of multiple domain and pair lists, the additional layer of complexity allowed them to achieve highly satisfactory results, with average errors around 0.06 eV for non-Rydberg excitations.

As an initial effort towards making local coupled cluster methods amenable to excited state geometry optimizations, Kats et al. performed PAO-based local-CC2[138] (LCC2) calculations in conjunction with density-fitting to further reduce the computational demands.[104,149] In addition to energies, Kats et al. also examined transition strengths with the same method

to find that the standard domains, while sufficient for excitation energies, were often too small for such properties, and they adopted new domain construction schemes to reduce the error.[57] Further progress has been made with the LCC2 method by the introduction of the Laplace transform.[105]

Following a somewhat different approach, Mata and Stoll calculated EOM-CCSD excitation energies via the incremental scheme.[131] Rather than restricting the virtual space for an occupied orbital, the occupied space is partitioned into fragments that are used in an N-body like expansion. However, Mata and Stoll pointed out that the virtual space for each fragment may be straightforwardly truncated via local correlation techniques, such as the PAO method.

The pair natural orbital (PNO)[43,44] local correlation scheme, similar to the PAO approach in that it truncates the virtual space, was first applied to coupled cluster excitation properties by Helmich et al.[133] following their work on local PNO-CIS(D).[132] Employing state-specific PNOs, they solved for one excited state at a time; they found that for the excited state PNOs, more truncation could be enforced compared to the ground state PNOs.

In addition to the PNO and PAO methods, we apply the orbital specific virtual (OSV)[49,50] approach to the calculation of EOM-CCSD excitation energies and transition dipole and rotatory strengths. All three local methods aim to reduce the size of the virtual space by inducing sparsity in the wavefunction, where the negligible components may be systematically truncated. While the OSVs have been used as a preliminary step in PNO-based local methods for excited states,[132,133] we present data for an initial test set with all three local

approaches separately and compare their performance. As an additional consideration, we also explore the performance when other approximations are enforced, namely that certain weak pairs are dropped from the calculation, with the ultimate goal of obtaining a robust, reduced-scaling method that introduces only minimal error to the quality of the excitation data.

5.2 Background

5.2.1 EOM-CCSD

Equation of motion coupled cluster (EOM-CC) theory can be viewed as a linear expansion of the coupled cluster ground state wavefunction.[150] Solving the resulting eigenvalue problem, as shown in 5.1, yields the right-hand wavefunction for excited state m and the associated excitation energy

$$\bar{H}R_m|\phi_0\rangle = E_m R_m|\phi_0\rangle, \tag{5.1}$$

where R is an excitation cluster operator and $\bar{H}$ is the similarity-transformed Hamiltonian ($e^{-\hat{T}}He^{\hat{T}}$ where $\hat{T}$ is the cluster operator). Since the similarity-transformed Hamiltonian is not Hermitian, we also have the left-hand counterpart with identical eigenvalue/excitation energy

$$\langle\phi_0|L_m\bar{H} = \langle\phi_0|L_m E_m, \tag{5.2}$$

where L is the analogous de-excitation operator.

For excitation energies only, solving the right-hand eigenvalue problem is sufficient. Properties such as dipole and rotatory strengths, however, require the appropriate transition moments; in this case, both left and right-hand excited wavefunction parameters must be obtained. The two, distinct transition moments may be written as

$$\langle\phi_0|\vec{A}|\phi_m\rangle = \langle\phi_0|(1+\Lambda)\bar{A}R_m|\phi_0\rangle \tag{5.3}$$

and

$$\langle\phi_m|\vec{B}|\phi_0\rangle = \langle\phi_0|L_m\bar{B}|\phi_0\rangle \tag{5.4}$$

where $\vec{A}$ ($\vec{B}$) and $\bar{A}$ ($\bar{B}$) are the appropriate one electron operator and its similarity transformed counterpart, respectively, and Λ is the de-excitation cluster operator pertaining to the coupled cluster left-hand ground state wavefunction. For dipole strengths, the electric dipole operator $\vec{\mu}$ is chosen for both $\vec{A}$ and $\vec{B}$. In the case of rotatory strengths, we need transition moments involving both the the electric dipole operator and also the magnetic dipole operator $\vec{m}$.

5.2.2 Local Correlation Techniques

The PAO, PNO, and OSV approaches address the computational cost by targeting the virtual orbital space in the calculation. A first step for all of these methods is the localization of the occupied orbitals, using the Pipek-Mezey[117] or Boys schemes,[136] for example, and throughout this paper all occupied orbitals are assumed to be localized. Once local molecular orbitals

(LMOs) are obtained, the virtual space in each method is truncated on an orbital and orbital-pair basis. For the doubles amplitudes (t_{ij}^{ab}), for instance, we have

$$t_{ij}^{ab} = \sum_{\bar{a}_{ij}\bar{b}_{ij}} Q_{a\bar{a}_{ij}}^{ij} t_{ij}^{\bar{a}_{ij}\bar{b}_{ij}} Q_{b\bar{b}_{ij}}^{ij} \tag{5.5}$$

$$\approx \sum_{\bar{a}_{ij}\bar{b}_{ij}\in[ij]} Q_{a\bar{a}_{ij}}^{ij} t_{ij}^{\bar{a}_{ij}\bar{b}_{ij}} Q_{b\bar{b}_{ij}}^{ij} \tag{5.6}$$

where we have introduced truncation in Equation 5.6 by restricting the sum over $\bar{a}_{ij}$ and $\bar{b}_{ij}$ to be only a subset of the full ij virtual space. In Equations 5.5 - 5.6, the $\mathbf{Q}^{ij}$ are the local transformation matrices for occupied orbital pair ij, virtual orbitals are represented by a, b, ..., and orbitals in the local virtual basis are denoted by an overbar with the subscript explicitly indicating to which pair the local space pertains.

For the PAO method, the canonical virtual molecular orbitals are transformed to the atomic orbital space, but contributions from the occupied orbitals are removed via the projection operator

$$|\chi_{\bar{\mu}}\rangle = \left(1 - \sum_i |\chi_i\rangle\langle\chi_i|\right)|\chi_\mu\rangle \tag{5.7}$$

where $\bar{\mu}$, μ, and i denote projected atomic orbitals, atomic orbitals, and occupied molecular orbitals, respectively. To create a reduced PAO space for an occupied orbital, a subset of atoms is assigned to each occupied orbital such that the PAOs associated with only those atoms become the virtual *domain* for that occupied orbital. Pair domains can straightforwardly be formed as the union of the virtual space for two occupied orbitals. While the

domains for each LMO may be different, each domain draws from the same set of PAOs. In order to form domains that yield sufficiently accurate results, several automatic completeness checks have been developed that systematically increase the domain size until a specified criterion is met.[56,58,115] The PAOs are of course non-orthogonal among themselves, but they importantly retain orthogonality against the occupied space.

The PNO and OSV bases may be derived from an MP2 occupied-pair density

$$\mathbf{D}^{ij} = \frac{2}{1+\delta_{ij}} \left(\mathbf{T}^{ij} \tilde{\mathbf{T}}^{ij\dagger} + \mathbf{T}^{ij\dagger} \tilde{\mathbf{T}}^{ij} \right) \tag{5.8}$$

where $\mathbf{T}^{ij}$ is a matrix of MP2 amplitudes with elements

$$[\mathbf{T}^{ij}]_{ab} = t_{ab}^{ij} = \frac{\langle ab|ij\rangle}{f_{ii} + f_{jj} - \epsilon_a - \epsilon_b}, \tag{5.9}$$

$\langle ab|ij\rangle$ is a two-electron integral in physicists' notation, and $\tilde{\mathbf{T}}^{ij}$ is defined as

$$\tilde{\mathbf{T}}^{ij} = 2\mathbf{T}^{ij} - \mathbf{T}^{ij\dagger}. \tag{5.10}$$

In Equations 5.8-5.10, the MP2 amplitudes are approximate in the sense that the denominator of Equation 5.9 involves diagonal elements of the Fock matrix (f_{ii}, f_{jj}) since the occupied orbitals have been localized, while ϵ_a and ϵ_b are still the canonical virtual orbital energies.

To arrive at PNOs, the density in Equation 5.8 is diagonalized for every pair

$$\mathbf{D}^{ij}\mathbf{Q}^{ij} = \mathbf{Q}^{ij}\mathbf{n}^{ij}, \tag{5.11}$$

yielding a distinct PNO basis for each pair, and the virtual space is reduced by only retaining PNOs with occupation numbers $n^{ij}_{\bar{a}_{ij}}$ above a certain threshold.

The OSVs may be obtained and truncated in a similar manner, but only the diagonal pair densities are used,

$$\mathbf{D}^{ii}\mathbf{Q}^{ii} = \mathbf{Q}^{ii}\mathbf{n}^{ii}, \tag{5.12}$$

creating a unique virtual space for each LMO rather than for every pair. To form the appropriate OSV basis for off-diagonal pairs, the OSV transformations are concatenated, as shown in Equation 5.13, with the parentheses indicating that $\mathbf{Q}^{ii}$ and $\mathbf{Q}^{jj}$ are joined together and not multiplied.

$$\mathbf{Q}^{ij} \equiv \left(\mathbf{Q}^{ii}\mathbf{Q}^{jj}\right) \quad \text{(OSV)} \tag{5.13}$$

We aim to compare the efficacy of these three local correlation techniques for coupled cluster excitation energies and also transition properties. The driving question is whether the desired truncation levels — those required to achieve significantly reduced computational cost — may be enforced with only a minimal loss in accuracy, in the hopes that larger systems than currently possible may be approached with coupled cluster methods for excited states and

still yield reliable results.

5.3 Computational Details

We have extended our pilot, PAO-based local EOM-CCSD code[102] to simulate the truncation in the OSV and PNO approaches as well. In the EOM-CC calculation, the excited state wavefunctions are solved for using the Davidson algorithm,[151] with a set of guess vectors $\{B_m\}$ serving as the starting point

$$\sigma_m = \bar{H} B_m. \tag{5.14}$$

During the update procedure for the guess vectors, the residuals for the "sigma equations" (Eq. 5.14) are walked through the appropriate local basis in the preconditioning step to simulate the local (truncated) amplitudes as new guess vectors are generated. When solving for the ground state amplitudes, a similar filtering is enforced in each iteration.[27,56,58,59,62,102]

Using the EOM-CCSD formalism with three local correlation techniques - the OSV, PAO, and PNO approaches - we have obtained excitation data for a small test set of molecules. We performed tests at several truncation thresholds for two smaller systems, formamide and N-methylformamide; additionally, we examined the 6-31G* and aug-cc-pVDZ basis sets for formamide. For the larger, chiral systems, (*S*)-2-chloropropionitrile and *P*-dimethylallene, we examine excitation energies, rotational strengths and dipole strengths for only a few occupation cutoffs and domain sizes. The occupied orbitals were localized via the Boys[136] procedure, although for N-methylformamide, we employed the Pipek-Mezey localization scheme

for comparison. In general, the localization scheme has only minimal impact on the performance of the local correlation calculations. By comparing the number of doubles amplitudes in the local basis to the number of amplitudes in the canonical basis, we compute a T_2 ratio; this provides us with a measure of the savings achieved at a particular truncation level.

While a rigorously reduced-scaling method would implement additional measures to relieve the computational cost, we only truncated the doubles amplitudes (D) or doubles truncated with weak pairs neglected (D+WP) as an initial performance test of these methods applied to EOM-CCSD calculations. In the PAO approach, weak pairs are those whose domains have no atoms in common. For the OSV and PNO methods, pairs are deemed weak if the MP2-pair energy falls under 1×10^{-4} E_h. The same restrictions on the virtual space for the ground state CC amplitudes were also enforced upon excited state wavefunctions. In this way, we used a consistent virtual space for a given occupied pair in all of the coupled cluster components of the calculation.

5.4 Discussion

5.4.1 Excitation Energies

The first several transition energies for formamide computed using EOM-CCSD with the 6-31G* and aug-cc-pVDZ basis sets are plotted against T_2 ratios in Figures 5.1-5.2, respectively. For the 6-31G* basis, good agreement is found between the local methods and the canonical

result for the first excited state energy at all computed truncation levels. Errors for the second state transition energy are also small for this basis set. However, for higher energy transitions, the local results quickly start overestimating the energies. Only at high T_2 ratios, when the virtual space is nearly complete, do the differences between the local and canonical results for all transitions become negligible.

For the correlation consistent basis set, the results for formamide seem to deteriorate even more rapidly as the virtual space is reduced. For all local methods, the energy of the first excited state differs by less than 0.5 eV. The overestimation of higher energy transitions is exacerbated in the OSV and PNO methods. Around a T_2 ratio of 0.60, the second excited state transition energy for the OSV and PNO methods is closer to the fourth transition energy in the canonical calculation - less than 0.1 eV from the fourth state transition energy but at least 0.5 eV from the transition energy for the second excited state. The PAO method, with BP domains, predicts the second transition energy to be around 0.1 eV greater than the canonical result.

For the slightly larger N-methylformamide, we computed the transition energies at several occupation thresholds for the aug-cc-pVDZ basis set. Similar to formamide, the errors for the local methods for the first excited state transition are very small, less than 0.1 eV, except for the most truncated cases. Furthermore, we can see the slower convergence to the canonical result for the higher energy transitions compared to the first few excited state energies. The PAO(BP) energies for all but the first excited state are in better agreement than OSV or PNO of similar truncation (T_2 ratios around 0.5). The PAO(BP) method still overestimates

Figure 5.1: EOM-CCSD/6-31G* excitation energies for formamide. The number N in parentheses represents the occupation cutoff 10^{-N} (OSV, PNO) or domain scheme (PAO). Only doubles amplitudes were truncated.

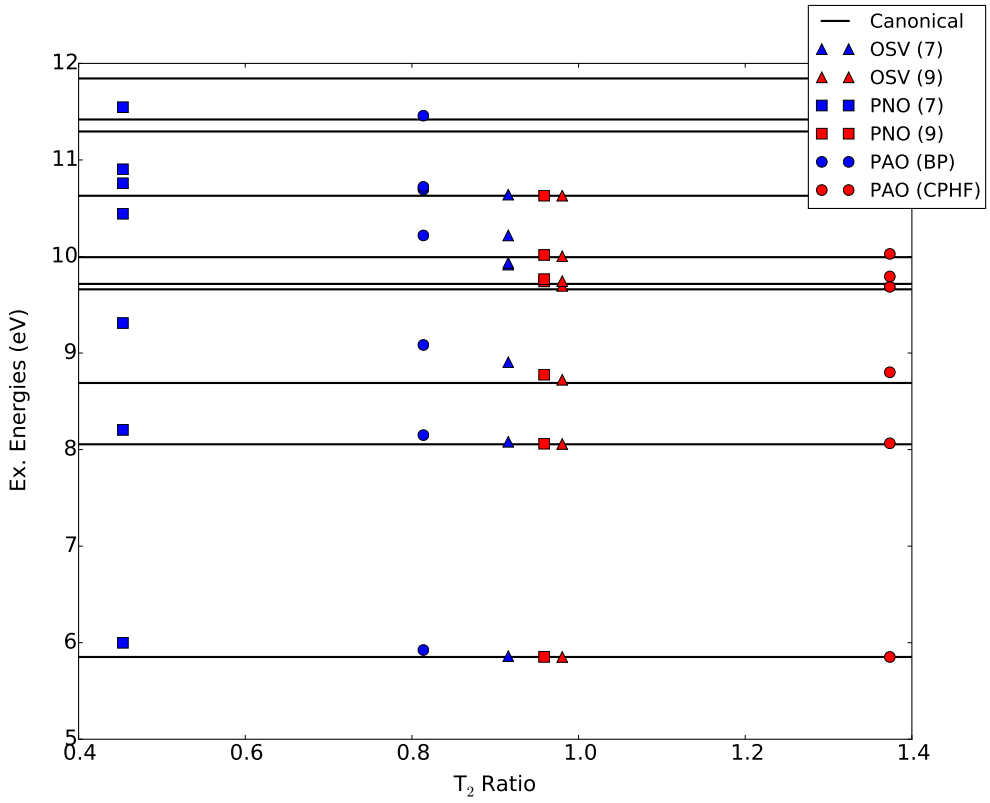

the energies, but the increase in error for the higher transitions is smaller than for the OSV or PNO approach.

Figure 5.4 contains plots of the transition energies for the first few excitations for (P)-dimethylallene. Unlike formamide and N-methylformamide, the virtual spaces for (P)-dimethylallene are large enough that weak pairs may actually be neglected from the calculation separately from the truncation of the virtual space (the small sizes of the formamide systems resulted in the D and D+WP results being essentially identical for the local methods).

Figure 5.2: EOM-CCSD/aug-cc-pVDZ excitation energies for formamide. The number N in parentheses represents the occupation cutoff 10^{-N} (OSV, PNO) or domain scheme (PAO). Only doubles amplitudes were truncated.

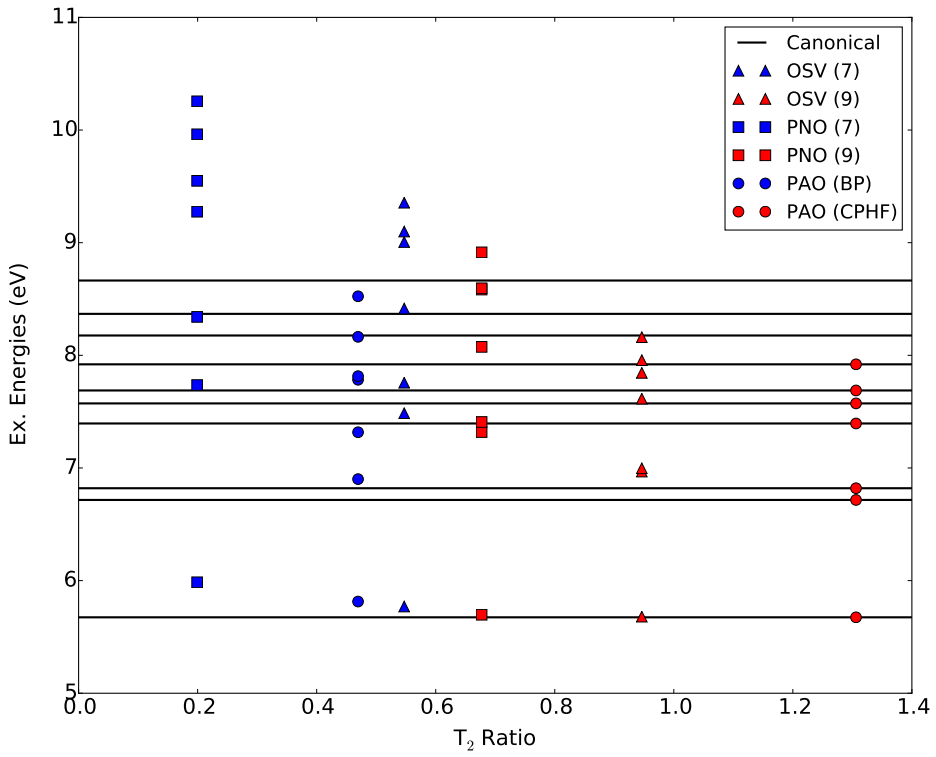

Nonetheless, when weak pairs are dropped from OSV or PNO calculations, very little additional localization error is introduced - less than 0.1 eV. For the PAO approach, on the other hand, the neglect of pairs increases the error to around 0.5 eV. However, the truncation (T_2 ratios) from PAO(D) to PAO(D+WP) with BP domains shifts from around 18% to 5%. The additional truncation in the OSV and PNO methods is relatively much smaller when the T_2 ratios are less than 40%. For excitation energies, the OSV and PNO methods naturally remove weak pairs as truncation is enforced; but the weak pair criterion for these methods is

Figure 5.3: EOM-CCSD/aug-cc-pVDZ excitation energies for N-methylformamide. The number N in parentheses represents the occupation cutoff 10^{-N} (OSV, PNO) or domain scheme (PAO). Only doubles amplitudes were truncated.

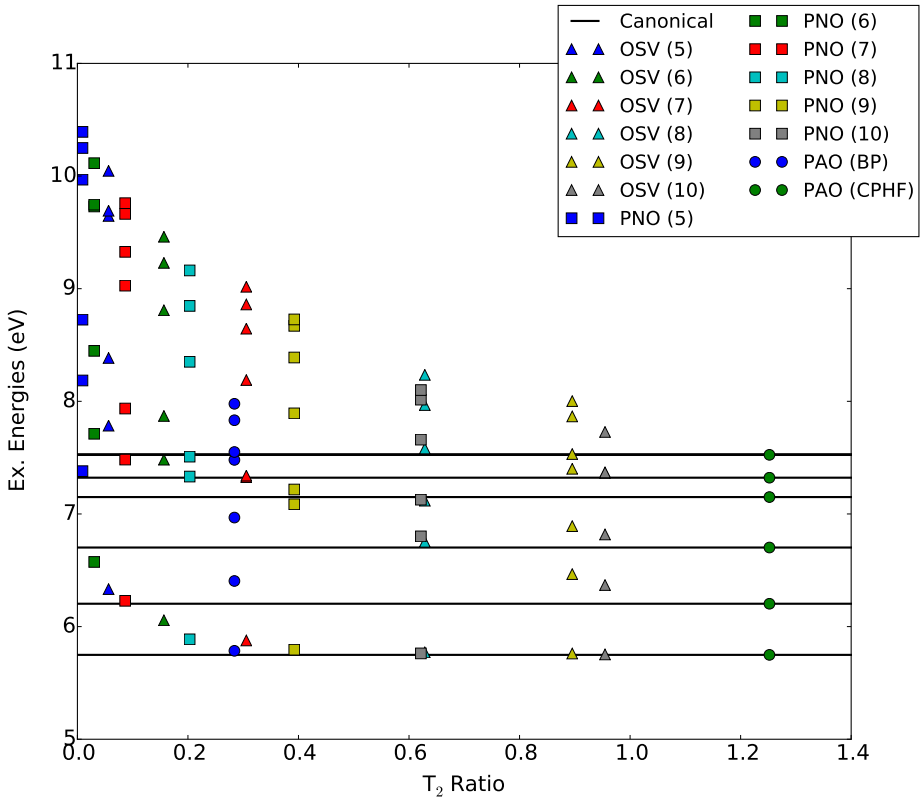

based on MP2 pair energies, while PAO weak pairs are based on overlaps between occupied orbital domains.

Similar conclusions regarding the effect of weak pair truncation may be drawn for (*S*)-2-chloropropionitrile, as shown in Figure 5.5. For T_2 ratios around 0.2, all methods are within 0.25 eV of the first two transition energies. The PAO(D) data with BP domains predicts the third and fourth transition energies to similar accuracy. The PNO and OSV methods, on the other hand, exhibit much higher error for the next transitions. The OSV(D) and

Figure 5.4: EOM-CCSD/aug-cc-pVDZ excitation energies for (*P*)-dimethylallene. The number N in parentheses represents the occupation cutoff 10^{-N} (OSV, PNO) or domain scheme (PAO). "D" indicates that only doubles were truncated, while "D+WP" indicates that weak pairs were neglected in addition to truncating the doubles.

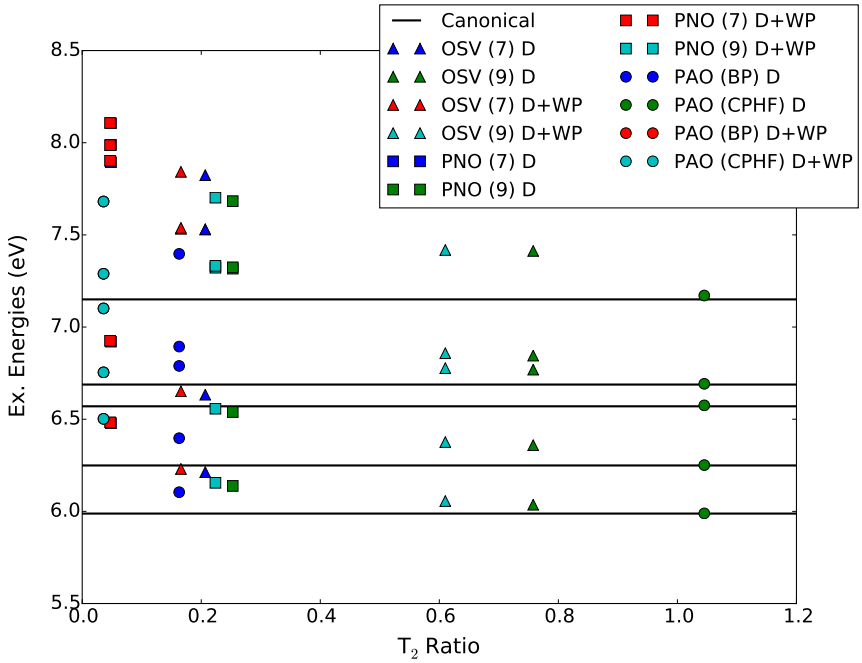

(D+WP) results at the 10^{-9} occupation cutoff qualitatively predict the first five transition energies, with increasing error for the higher energy transitions; the error is overestimated by less than 0.25 eV for the first four states. However, the improved agreement with the canonical result comes at the cost of higher T_2 ratios.

5.4.2 *P*-dimethylallene: Rotational and Dipole Strengths

For (*P*)-dimethylallene, the local rotational strengths at the looser occupation threshold (10^{-7}) and smaller domains (BP) are shown in Table 5.1. All methods agree in sign for the

Figure 5.5: EOM-CCSD/aug-cc-pVDZ excitation energies for (*S*)-2-chloropropionitrile. The number N in parentheses represents the occupation cutoff 10^{-N} (OSV, PNO) or domain scheme (PAO). "D" indicates that only doubles were truncated, while "D+WP" indicates that weak pairs were neglected in addition to truncating the doubles.

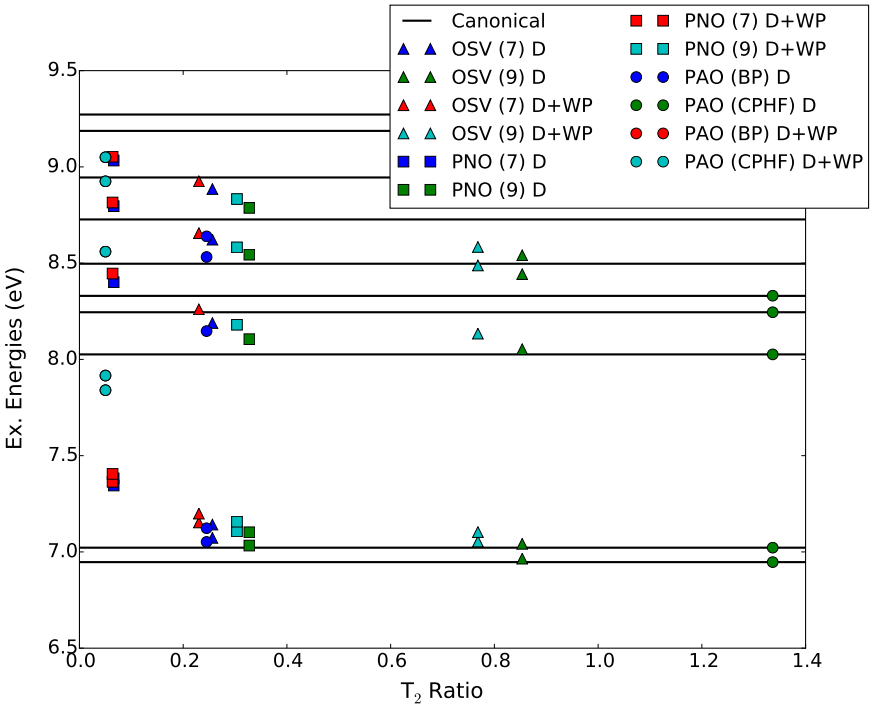

first two excitations, with the only exception being PAO(D+WP) for the second transition. The canonical rotational strength for the second state is small at -0.5503×10^{-40} cgs; and the overall change in the PAO results between D and D+WP is only about 2×10^{-40} cgs.

A striking feature of these results is that for different states a given method is not of similar accuracy. For example, the PNO method more closely reproduces the canonical result than the other methods for the third and fifth transitions. For the fifth transition, the canonical result is 2.776×10^{-40} cgs, but the OSV and PAO methods predict a negative rotational strength. Both the PNO(D) and PNO(D+WP) results, on the other hand, are the correct

sign and magnitude.

While the OSV(D) and PAO(D) values yield the incorrect sign for the third and fifth transitions, they are in much better agreement with the canonical rotational strength for the fourth excited state. The canonical value is 11.85×10^{-40} cgs, and the OSV(D) and PAO(D) values predict 18.53×10^{-40} cgs and 16.06×10^{-40} cgs respectively; the PNO(D) rotational for this transition exhibits much higher error, predicting the wrong sign with -59.34×10^{-40} cgs.

Table 5.1: EOM-CCSD/aug-cc-pVDZ velocity gauge rotational strengths (10^{-40} cgs) for (P)-dimethylallene.

Rotational Strengths (10^{-40} cgs)		OSV		PNO		PAO	
	Canonical	10^{-7}		10^{-7}		BP	
State		D	D+WP	D	D+WP	D	D+WP
1	-19.9183	-3.4509	-3.2539	-2.1540	-2.2333	-14.0352	-23.3898
2	-0.5503	-0.4362	-0.5029	-0.1851	-0.2190	-0.7955	1.2361
3	9.0618	-42.3643	-42.1242	6.8466	7.4025	-0.6394	14.1257
4	11.8540	18.5258	19.0389	-59.3445	-58.9813	16.0637	15.2577
5	2.7762	-6.7271	-7.6050	2.8000	1.6973	-2.1289	-34.8594
6	-4.8327						
7	-6.2756						
8	2.2385						
9	-0.0082						
10	1.6431						
T_2 Ratio	n/a	0.207	0.166	0.0483	0.0468	0.163	0.0358

Rotational strengths computed with more complete virtual spaces have been tabulated in Table 5.2. The PAO(D) values for the CPHF-based domains are in excellent agreement with the canonical rotational strengths for all computed transitions. However, the virtual space is nearly complete, as indicated with the corresponding T_2 ratio of 1.045. The PAO(D+WP) T_2 ratio of 0.358 indicates that, despite the larger orbital domains, the virtual space is still incomplete since not all domains overlap with each other and weak pairs may still be neglected.

The OSV method now correctly predicts the sign for all rotational strengths except for the third excited state. With the larger virtual space, the PNO results for the third and fifth transitions yield the wrong sign, in contrast to the PNO data at the 10^{-7} cutoff. However, the PNO rotational strength for the fourth excited state changes sign at the tighter occupation threshold, coming into agreement with the canonical result.

Neglecting weak pairs based on MP2 pair energies introduces very little error into the rotational strengths for the OSV and PNO approaches. The good agreement between D and D+WP results for the OSV and PNO methods may be attributed to the similarity of the sizes of the virtual spaces. The largest difference occurs for the 10^{-9} OSV results, where the ratios are 0.758 and 0.610, respectively, for the D and D+WP calculations.

Table 5.2: EOM-CCSD/aug-cc-pVDZ velocity gauge rotational strengths (10^{-40} cgs) for (P)-dimethylallene.

Rotational Strengths (10^{-40} cgs)		OSV		PNO		PAO	
	Canonical	10^{-9}		10^{-9}		CPHF (0.10)	
State		D	D+WP	D	D+WP	D	D+WP
1	-19.9183	-13.2762	-13.9300	-5.2236	-5.9940	-18.2345	-23.3898
2	-0.5503	-1.0030	-1.0298	-0.5636	-0.6370	-0.5704	1.2361
3	9.0618	-6.0225	-5.1277	-36.7667	-36.1732	8.9650	14.1257
4	11.8540	13.9205	14.0788	17.2129	17.5457	11.7066	15.2577
5	2.7762	15.8662	13.0691	-7.4472	-8.2755	2.9290	-34.8594
6	-4.8327						
7	-6.2756						
8	2.2385						
9	-0.0082						
10	1.6431						
T_2 Ratio	n/a	0.758	0.610	0.253	0.224	1.045	0.0358

In Table 5.3, dipole strengths for (*P*)-dimethylallene are collected for the 10^{-7} cutoff and BP domains. Between the three local methods, the PAO approach agrees best with the canonical dipole strengths. For the transition to the first excited state, the PAO(D) dipole strength undershoots the canonical value, but the PAO values are increasingly overestimated for the higher transitions. For example, the PAO(D) dipole strength for the second excited state is 56.03×10^{-40} cgs compared to 54.16×10^{-40} cgs for the canonical calculation; yet, for the fourth excited state, the PAO(D) value is 207.8×10^{-40} cgs vs. 131.0×10^{-40} cgs for the full virtual space.

The OSV approach only qualitatively reproduces the dipole strengths for the third and fourth excited state transitions, but they still differ by about a factor of two from the full calculation. For instance, the OSV dipole strength is 2321×10^{-40} cgs while the reference value is 1073×10^{-40} cgs. OSV dipole strengths for the remaining three transitions differ by an order of magnitude from the canonical values. For the PNO dipole strengths at this occupation cutoff, none of the values match in the order of magnitude of the canonical results; however, the PNO virtual space is much more truncated at this cutoff than the OSV space. The T_2 ratio for the OSV(D) calculation is 0.207, while the PNO ratio is only 0.0483. However, the PAO(D+WP) dipole strengths with the BP domains are still in qualitative agreement for all computed dipole strengths with a T_2 ratio of 0.0358, smaller than that of the PNO calculations.

Table 5.3: EOM-CCSD/aug-cc-pVDZ dipole strengths (10^{-40} cgs) for (*P*)-dimethylallene.

Dipole Strengths (10^{-40} cgs)		OSV		PNO		PAO	
	Canonical	10^{-7}		10^{-7}		BP	
State		D	D+WP	D	D+WP	D	D+WP
1	34.9086	3.0012	3.2289	0.9279	1.0720	27.3680	50.4429
2	54.1642	3.2466	4.0835	0.4424	0.5898	56.0269	76.4228
3	1073.2303	2320.9212	2346.2034	47.6895	52.4582	1237.9677	1374.1101
4	131.0148	334.9032	348.7589	4456.1841	4394.7492	207.7547	143.1676
5	2612.9509	230.1498	232.7415	516.8925	522.3604	4252.3517	5257.0807
6	107.5289						
7	68.8876						
8	3.1739						
9	11.6465						
10	1763.8348						
T_2 Ratio	n/a	0.207	0.166	0.0483	0.0468	0.163	0.0358

Tightening the occupation threshold and increasing the domains improves agreement between canonical dipole strengths and the local values, as shown in Table 5.4. The PAO(D) with CPHF-based domains most closely reproduce the reference results, but the virtual space is almost complete. The virtual space also significantly increases for the OSV method - the T_2 ratio changes from 0.207 to 0.758 when the occupation cutoff is tightened from 10^{-7} to 10^{-9}. As a result all of the OSV dipole strengths at the 10^{-9} cutoff are in qualitative agreement the canonical case. The PNO T_2 ratio for the tighter cutoff is still relatively small at 0.253 (compared to 0.166 at the 10^{-7} threshold). The corresponding improvement in accuracy is also small - only the dipole strength for the second and third excited states matches the order of magnitude of the canonical calculation, similar to the OSV (10^{-7}) case.

Table 5.4: EOM-CCSD/aug-cc-pVDZ dipole strengths (10^{-40} cgs) for (*P*)-dimethylallene.

Dipole Strengths (10^{-40} cgs)		OSV		PNO		PAO	
	Canonical	10^{-9}		10^{-9}		CPHF (0.10)	
State		D	D+WP	D	D+WP	D	D+WP
1	34.9086	18.0266	20.4335	4.1086	5.0630	32.0434	50.4429
2	54.1642	34.7655	38.4822	4.7254	5.5604	54.1516	76.4228
3	1073.2303	1274.2980	1275.7495	2098.1635	2069.9200	1072.7723	1374.1101
4	131.0148	203.8391	201.8198	306.1187	311.3973	129.9186	143.1676
5	2612.9509	5035.7045	5069.8527	180.7093	180.3198	2481.0822	5257.0807
6	107.5289						
7	68.8876						
8	3.1739						
9	11.6465						
10	1763.8348						
T_2 Ratio	n/a	0.758	0.610	0.253	0.224	1.045	0.0358

5.4.3 (*S*)-2-chloropropionitrile: Rotational and Dipole Strengths

Rotational strengths for (*S*)-2-chloropropionitrile at the 10^{-7} and BP domains are presented in Table 5.5. For the first three transitions, the local approaches correctly predict the sign for the rotational strength, with the exception of the PNO values for the first excited state. However, the canonical and local rotational strengths for the first excited state are all small - less than 1×10^{-40} cgs. The PAO(D+WP/BP) values most closely match the canonical rotational strengths for the first two excited states, but this is likely due to fortuitous cancellation of error. For the rotational strength of the fourth excited state, none of the local methods produce a positive value, compared to the canonical 17.96×10^{-40} cgs. For the transition to the fifth excited state, all methods agree on the sign, but the PNO and PAO results are qualitatively different. The PNO values underestimate the value by an order of magnitude, while the PAO(D) result overestimates in a similar manner.

Table 5.5: EOM-CCSD/aug-cc-pVDZ velocity gauge rotational strengths (10^{-40} cgs) for (*S*)-2-chloropropionitrile.

Rotational Strengths (10^{-40} cgs)		OSV		PNO		PAO	
	Canonical	10^{-7}		10^{-7}		BP	
State		D	D+WP	D	D+WP	D	D+WP
1	0.8909	0.4772	0.0459	-0.0824	-0.2059	0.5534	0.8349
2	-3.2800	-2.4469	-1.4647	-1.5225	-0.8862	-2.5343	-2.9430
3	-3.1301	-1.3710	-1.5524	-0.8196	-0.9278	-1.6426	-1.3750
4	17.9566	-4.5532	-5.7815	-3.2841	-3.9112	-8.9352	-5.7852
5	5.4934	2.1621	2.0530	0.7580	1.1304	27.1283	8.9894
6	7.2765						
7	-3.8143						
8	-7.6964						
9	10.5081						
10	-51.6622						
T_2 Ratio	n/a	0.256	0.230	0.0659	0.0639	0.245	0.0502

Tightening the occupation threshold improves both the OSV and PNO results. The PNO values for rotational strengths for the first excited state now agree with the canonical value, as shown in Table 5.6. With an essentially complete virtual space with the CPHF domains, the PAO(D) results reproduce closely the canonical rotational strengths. The OSV and PNO methods still predict the incorrect sign for the fourth state. Not including the PAO(D/CPHF) value, the PNO methods most accurately predict the rotational strength for the fifth excited state, despite heavier truncation compared to the OSV approach: 4.442×10^{-40} cgs (T_2 ratio 0.328) vs. 28.36×10^{-40} cgs (T_2 ratio 0.845) for the PNO(D) and OSV(D) rotational strengths, respectively, where the canonical value is 5.493×10^{-40} cgs.

Table 5.6: EOM-CCSD/aug-cc-pVDZ velocity gauge rotational strengths (10^{-40} cgs) for (*S*)-2-chloropropionitrile.

Rotational Stengths (10^{-40} cgs)		OSV		PNO		PAO	
	Canonical	10^{-9}		10^{-9}		CPHF (0.10)	
State		D	D+WP	D	D+WP	D	D+WP
1	0.8909	0.7865	0.3122	0.4305	0.0855	0.8647	0.8349
2	-3.2800	-3.0803	-1.9427	-2.5818	-1.5551	-3.2800	-2.9430
3	-3.1301	-2.2538	-2.9516	-1.5364	-1.9755	-2.9195	-1.3750
4	17.9566	-6.6444	-8.7029	-7.5838	-7.5231	18.6240	-5.7852
5	5.4934	28.3591	29.7585	4.4417	6.1835	5.1224	8.9894
6	7.2765						
7	-3.8143						
8	-7.6964						
9	10.5081						
10	-51.6622						
T_2 Ratio	n/a	0.854	0.768	0.328	0.304	1.34	0.0502

Dipole strengths for (*S*)-2-chloropropionitrile at the higher truncation levels are collected in Table 5.7. The OSV and PNO results qualitatively agree with the full calculation for the first, second, and third excited states. For the third state, the dipole strength is overestimated by both OSV and PNO, whereas the canonical value is much larger than the OSV and PNO predictions for the fifth excited state. The PAO(D/BP) results, on the other hand, are in much better agreement for the fifth excited state, with a T_2 ratio similar to OSV(D) around 0.25. The canonical dipole strength for the fifth state is 898×10^{-40} cgs, while OSV(D) yields 48.43×10^{-40} cgs and PAO(D) 1265×10^{-40} cgs.

Table 5.7: EOM-CCSD/aug-cc-pVDZ dipole strengths (10^{-40} cgs) for (S)-2-chloropropionitrile.

Dipole Strengths (10^{-40} cgs)		OSV		PNO		PAO	
	Canonical	10^{-7}		10^{-7}		BP	
State		D	D+WP	D	D+WP	D	D+WP
1	46.3275	36.8605	39.6206	60.8860	48.2000	54.9268	116.3838
2	195.3127	170.6412	153.1615	136.9407	136.9474	206.1966	304.7047
3	7.8963	24.0813	23.3510	18.5148	18.0093	14.9040	16.0866
4	1246.0871	1385.6494	1387.2808	1135.0758	1128.5315	1778.9027	1576.0830
5	897.7412	48.4261	37.5076	33.6007	35.8658	1264.5591	624.6500
6	1030.4038						
7	262.9511						
8	124.1503						
9	537.8126						
10	1075.4570						
T_2 Ratio	n/a	0.256	0.230	0.0659	0.0639	0.245	0.0502

Table 5.8 shows dipole strengths with less truncated virtual spaces. The OSV dipole strengths improve for all states, especially for the fifth excited state where qualitative agreement is now achieved. The OSV(D/10^{-7}) dipole strength for this transition is 48.43×10^{-40} cgs, but OSV(D/10^{-9}) predicts a value of 1166×10^{-40} cgs, in much better agreement with 897.7×10^{-40} cgs for the canonical case. Both OSV and PNO values still overshoot the dipole strength for the transition to the third excited state, but the PAO(D) result accurately predicts the quantity at 7.443×10^{-40} cgs compared to the canonical result of 7.896×10^{-40} cgs. The PNO(D/10^{-9}) dipole strength is 25.83×10^{-40} cgs for the third excited state, in worse agreement than PNO(D/10^{-7}) value of 18.51×10^{-40} cgs. However, the PNO(D/10^{-9}) results for the first two excited states qualitatively and quantitatively reproduce the canonical values with low T_2 ratios, competitive with PAO(D/BP).

Table 5.8: EOM-CCSD/aug-cc-pVDZ dipole strengths (10^{-40} cgs) for (S)-2-chloropropionitrile.

Dipole Strengths (10^{-40} cgs)		OSV		PNO		PAO	
	Canonical	10^{-9}		10^{-9}		CPHF (0.10)	
State		D	D+WP	D	D+WP	D	D+WP
1	46.3275	47.3329	49.4538	42.9496	45.3051	46.3943	116.3838
2	195.3127	201.2315	183.6644	191.0065	173.3500	194.9098	304.7047
3	7.8963	19.9844	16.8977	25.8287	24.5944	7.4429	16.0866
4	1246.0871	1781.6694	1788.9430	1533.0899	1530.1307	1231.1015	1576.0830
5	897.7412	1166.0868	1217.8733	64.4877	88.1004	903.1406	624.6500
6	1030.4038						
7	262.9511						
8	124.1503						
9	537.8126						
10	1075.4570						
T_2 Ratio	n/a	0.854	0.768	0.328	0.304	1.34	0.0502

5.5 Conclusions

Using three local correlation techniques, we have computed local EOM-CCSD excitation energies for the first few excited states of a test set of molecules. For two chiral systems, (*P*)-dimethylallene and (*S*)-2-chloropropionitrile, we also calculated rotational and dipole strengths for each transition. Unlike work by others,[103–105,132,133] we enforced the same truncated virtual spaces on both the ground and excited state amplitudes in order to treat both in an comparable manner. At low T_2 ratios, good agreement is only found for the first few excited states. Truncation of the excited state wavefunctions with the same restrictions as the ground state appears to work best with the PAO method. Nonetheless, the straightforward truncation based on ground-state virtual spaces and domains results in larger errors than desired.

For excitation energies, all computed PAO results were generally in best agreement with the canonical values. However, both the OSV and PNO methods also accurately reproduced the transition energies for the first few states. All methods tend to increasingly overestimate the excitation energy for higher excitations and as more of the virtual space is truncated.

Instances arise for all local methods where the sign for the rotational strength is predicted incorrectly, while data for other transitions for the same method and virtual space may be well-reproduced. Due to cancellation of error, transition data for different states may be of different accuracy, although the nature of the transition (charge transfer vs. local excitation) likely plays a role as well.

Errors in the rotational strengths are somewhat reflected in the dipole strengths. The local values tend to qualitatively predict the dipole strengths for transitions where the method yields the correct sign for the rotational strength. Only as the virtual space nears completion, as can be seen for the OSV method at the 10^{-9} cutoff and PAO method with BP domains, do the local dipole strengths come into close quantitative agreement as well.

Neglecting weak pairs in the OSV and PNO calculations introduces only minor additional error in both rotational and dipole strengths. However, very little additional truncation is introduced when they are dropped from the calculation, as can be seen in similar T_2 ratios for D vs. D+WP for the OSV and PNO methods. For the PNO scheme, on the other hand, larger differences in truncation and accuracy arise with the weak pair approximation. However, the pairs are classified by orbital domain overlaps, rather than by pair energies as in the OSV and PNO approaches.

Chapter 6

Simulation of Circularly Polarized Luminescence Spectra Using Coupled Cluster Theory

6.1 Introduction

A variety of spectroscopic techniques are widely employed to assist in the determination of the absolute stereochemical configurations of chiral compounds[69–72,152] — the important

class of molecules lacking an improper rotation axis — that take advantage of the difference in the indices of refraction (birefringence), absorption (dichroism), or scattering (Raman optical activity) between left- and right-circularly polarized light when interacting with a non-racemic sample. The emission counterpart to electronic circular dichroism (ECD) is circularly polarized luminescence (CPL); the former provides structural information about the ground state, and the latter accesses complementary characteristics of the excited state. When only minor changes in the geometry occur between the ground state and excited state, CPL and ECD spectra will exhibit transitions similar in magnitude and sign, but alterations in the geometry can lead to significant differences between the two — sometimes even changes in sign of certain rotational strengths.

Over the last several decades, measurements of CPL spectra have found a home in studies of proteins,[153,154] transition metal complexes,[155] and even polymers.[156] CPL also opens the door for novel chiroptical experiments, such as those probing achiral luminescent materials in chiral environments[157,158] and exciting chiral solutions with only right or left-hand circularly polarized light and monitoring the emission.[159–161] Indeed, it has also been shown that certain fireflies that have a right and left lantern also exhibit CPL.[162] Recent advances in instrumentation such as the development of light-emitting diode sources promise to increase the practicality and usage of CPL measurements.[163]

The investigation of absolute configuration *via* CPL — like its circular dichroism, birefringence, and Raman scattering counterparts — requires external references for the assignment of the signs of specific chiroptical responses. This need has motivated the development of the-

oretical models of CPL spectra, beginning with the semiempirical calculations of Schlessinger and Warshel in 1974.[164] The first density-functional theory (DFT) computations were carried out by Coughlin *et al.* in 2008[155] in their examination of iridium (III) complexes. In 2010, Pritchard and Autschbach[165] used DFT to compute Franck-Condon vibrationally resolved absorption, emission, ECD, and CPL bands corresponding to the lowest-energy $n \rightarrow \pi^*$ transition of the small chiral ketones *d*-camphorquinone, (*S*,*S*)-*trans*-β-hydrindanone, and (1*R*,5*S*)-*cis*-β-hydrindanone for comparison with well-resolved experimental spectra. They found that the camphorquinone exhibits little structural variation between the ground and excited state, while the $n \rightarrow \pi^*$ excitation results in a loss of C_2 symmetry in the *trans*-β-hydrindanone as its carbonyl is bent out of the plane of the cylopentane ring.

Pecul and Ruud[148] also carried out a series of DFT computations of CPL spectra of organic ketones. Their selection of five β,γ-enones was directly inspired by the experimental work of Schippers *et al.*,[166] who reported fascinating variations in the signs of rotational strengths for the lowest-energy ECD $n \rightarrow \pi^*$ and CPL $\pi^* \rightarrow n$ transitions. Pecul and Ruud found that three of the five compounds — (1*S*,3*R*)-4-methyleneadamantan-2-one, (1*R*)-7-methylenebicyclo[2.2.1]heptan-2-one, and (1*S*)-2-methylenebicyclo[2.2.1]heptan-7-one — manifest two conformers in the excited state corresponding to different orientations of the carbonyl group relative to the bridgehead carbon of the cage, and each conformer yields an opposite-sign rotatory strength. For these three compounds, the overall sign of the CPL transition was found to depend on which structure was lower in energy, and disagreement was observed for two of the compounds (the methyleneadamantan-2-one and the methylenebi-

cyclo[2.2.1]heptan-7-one) between the B3LYP functional[167,168] and its long-range corrected counterpart, CAM-B3LYP.[169] Furthermore, while CAM-B3LYP predictions of dipole and rotatory strengths were closer to experiment for four of the five compounds, B3LYP dissymmetry factors — which are proportional to the ratio of the two transition strengths — were closer to the measured values, apparently due to cancellation of errors. For the smallest of their β,γ-enones, (1*R*,4*R*)-norbornenone, Pecul and Ruud also optimized the ground and excited states using the second-order coupled cluster method (CC2), implemented for greater computational efficiency using the resolution-of-the-identity approach (RI-CC2). Although they found that RI-CC2 produced a significantly longer C=O bond length in the excited state as compared to DFT, CAM-B3LYP and RI-CC2 CPL rotatory strengths (the latter computed using the B3LYP optimized excited-state geometry) agreed well with each other, but were not as close as B3LYP to the experimental data.

The most recent theoretical CPL simulations include those of Longhi *et al.*,[170] for a series of bicyclic ketones, again focusing on the lowest-energy $n \rightarrow \pi^*$ transition using DFT (CAM-B3LYP). Similarly to Pecul and Ruud, they found that, for compounds with more than one excited-state conformer, the sign of the CPL rotatory strengths depended primarily on which was lower in energy, as distinguished by the direction of puckering of the C=O moiety. For camphor, two such conformers were identified, while for 5-oxocamphor, which has two carbonyls, four minimum-energy structures compete. Finally, we note the use of the BHLYP functional by Shen *et al.* in the analysis of photophysical emission of organometallic helicenes in order to elucidate the influence of platinum centers on the compounds' CPL spectra and

other chiroptical properties.[171]

The purpose of the present study is twofold. First, we consider the importance of higher-order electron correlation effects on the sign and structure of simulated CPL spectra by application of coupled cluster theory — particularly on the geometries and energy ordering of key excited states — for the first time at the singles and doubles (CCSD) level of theory for the ground state and the equation-of-motion CCSD (EOM-CCSD) level for excited states. Second, for selected compounds we go beyond the lowest-energy transition and consider the requirements of a robust theoretical simulation of CPL bands corresponding to non-valence excited states.

6.2 Computational Details

From the EOM-CC perspective, transition strengths are computed using the eigenfunctions of the similarity-transformed Hamiltonian, *via*,[8,172–175]

$$e^{-\hat{T}}\hat{H}e^{\hat{T}}\hat{\mathcal{R}}_n|0\rangle = \bar{H}\hat{R}_n|0\rangle = E_n\hat{\mathcal{R}}_n|0\rangle, \tag{6.1}$$

and

$$\langle 0|\hat{\mathcal{L}}_n\bar{H} = E_n\langle 0|\hat{\mathcal{L}}_n, \tag{6.2}$$

where $|0\rangle$ is the single-determinant reference function, $\hat{T}$ is the ground-state cluster operator, and $\hat{\mathcal{R}}_n$ and $\hat{\mathcal{L}}_n$ represent excitation and de-excitation cluster operators, respectively. Unlike

variational methods such as configuration interaction, the left- and right-hand eigenfunctions are not simply adjoints of each other due to the non-Hermitian nature of $\bar{H}$, though the excitation energies, E_n, are identical. This leads to the distinct left- and right-hand transition-moment expressions,

$$\langle\Psi_0|\vec{A}|\Psi_n\rangle = \langle 0|\left(1+\hat{\Lambda}\right)e^{-\hat{T}}\vec{A}e^{\hat{T}}\hat{\mathcal{R}}_n|0\rangle, \tag{6.3}$$

and

$$\langle\Psi_n|\vec{B}|\Psi_0\rangle = \langle 0|\hat{\mathcal{L}}_n e^{-\hat{T}}\vec{B}e^{\hat{T}}|0\rangle, \tag{6.4}$$

where $|\Psi_0\rangle$ and $|\Psi_n\rangle$ are the ground- and nth-excited-state, respectively, $\vec{A}$ and $\vec{B}$ are (vector) property operators, and $\hat{\Lambda}$ denotes the cluster de-excitation operator associated with the left-hand ground-state wave function. Although the corresponding transition strengths (the dot product of the above moment expressions) are not size intensive in the truncated EOM-CC approach,[173,175] such errors are not likely to be significant for the relatively small molecular systems considered in this work. For the dipole transition strengths required for absorption and fluorescence, both $\vec{A}$ and $\vec{B}$ are chosen to be the electric dipole operator, and CD and CPL rotatory strengths require the mixed response function between the electric dipole operator and the magnetic dipole operator, $\vec{m}$. While the choice of length ($\vec{r}$) or velocity ($\vec{p}$) representation for the electric dipole operator is inconsequential for exact wave functions, the use of finite basis sets leads to differences between the computed transition strengths (as well as arbitrary origin dependence for the rotatory strengths calculated us-

Figure 6.1: Structures of (a) (1*R*,4*R*)-norbornenone, (b) (*S*)-3-methylcyclopentanone, (c) (1*R*,4*R*)-α-fenchocampherone, (d) *trans*-bicyclo[3.3.0]octane-3,7-dione, (e) (1*R*,5*S*)-*cis*-β-hydrindanone, (f) (*S*,*S*)-*trans*-β-hydrindanone, (g) (1*R*)-7-methylenebicyclo[2.2.1]heptan-2-one, and (h) (1*S*)-2-methylenebicyclo[2.2.1]heptan-7-one.

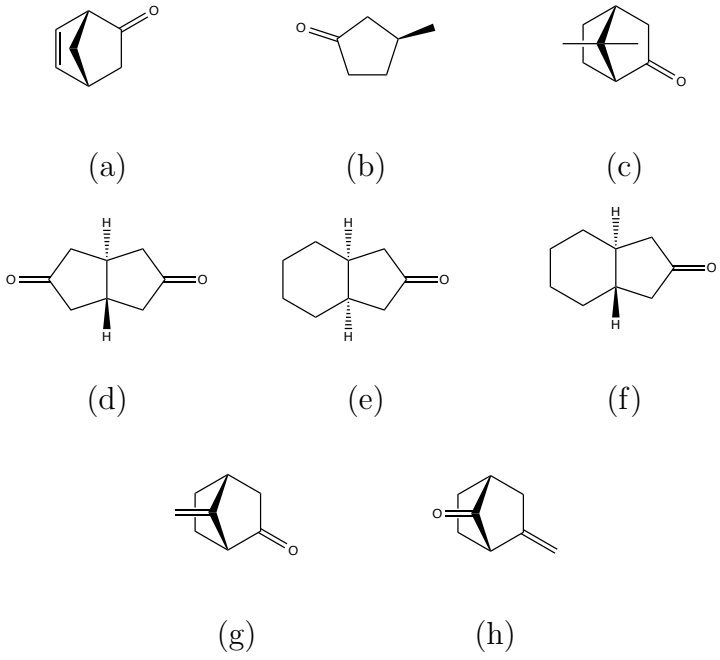

ing the length representation) for all quantum chemical methods. However, coupled cluster transition strengths exhibit differences between the two representations even in a complete basis due to the lack of variational optimization of the CC energy with respect to the molecular orbitals used to represent the correlated wave function. (Note that this problem also plagues truncated configuration interaction methods.) Thus, in this work, when computing the dipole and rotational strengths, both the length and velocity formalisms were obtained, with the latter provided in the Supplementary Information.

We have carried out ECD and CPL calculations for the series of organic ketones shown in

Figure 6.1. All ground-state geometries were optimized using the B3LYP[119,167,168] and CAM-B3LYP[169] functionals in conjunction with the aug-cc-pVDZ[123,139] basis set. The relevant excited states were optimized with the corresponding time-dependent DFT (TDDFT)[176] and employing the same basis set and functional. For two systems — (1*R*,4*R*)-norbornenone and (*S*)-3-methylcyclopentanone — we also performed coupled cluster level optimizations of the geometries, using CCSD for the ground states and EOM-CCSD for the excited states, again with the aug-cc-pVDZ basis set.[21,65,172,177] Structural optimizations were considered converged when the maximum and root-mean-squared values of the Cartesian gradient vector fell below $10^{-4} E_h/a_0$. Analytic gradient methods were used for both DFT- and coupled-cluster-based optimizations.[177] All electrons were correlated in the coupled cluster structural optimizations, while the 1*s* core orbitals on all carbon and oxygen atoms were held frozen in the coupled cluster transition-property computations. DFT computations were performed using Gaussian-09,[178] and all coupled-cluster level results were obtained using the PSI4 quantum chemical program.[137]

Dipole absorption strengths and ECD rotatory strengths were obtained for the lowest several excited states in the TDDFT and EOM-CCSD approximations at the optimized ground state geometry of each structure using the aug-cc-pVDZ basis set. Similarly, dipole emission and CPL rotatory strengths were computed using the same quantum chemical methods at the corresponding excited-state geometries. In addition to calculating the dipole and rotational

strengths, we also computed the dissymmetry factor,[148,165,166]

$$g_x \equiv \frac{4R_x}{D_x} \tag{6.5}$$

where R is the rotational strength and D is the dipole strength, and the subscript $x = a, e$ indicates either absorption (ECD) or emission (CPL).

6.3 Results and Discussion

6.3.1 Optimized Excited-State Structures: (1*R*,4*R*)-Norbornenone and (*S*)-3-Methylcyclopentanone

The optimization of electronically excited states is often cumbersome and computationally expensive, particularly for advanced many-body methods such as coupled cluster theory. It would therefore be advantageous to identify less expensive, yet acceptably accurate alternatives to complete CC optimizations. With this goal in mind, we have carried out EOM-CCSD/aug-cc-pVDZ optimizations of the ground and first three excited states of (1*R*,4*R*)-norbornenone, as well as the ground and first two excited states of (*S*)-3-methylcyclopentanone, for comparison to corresponding B3LYP/aug-cc-pVDZ optimizations. (Complete coordinates for all structures are given in Appendix A.)

In the work by Pecul and Ruud,[148] they observed that the RI-CC2 optimized structure of the

first ($n \rightarrow \pi^*$) excited state of norbornenone differed from its B3LYP counterpart primarily in the C=O bond distance, with CC2 yielding a much longer value of 1.360 Å vs. 1.267 Å with B3LYP (and 1.264 Å with CAM-B3LYP). Upon comparison with the first excited state of formaldehyde, which also arises from an $n \rightarrow \pi^*$ transition, they concluded that the CC2 and B3LYP results likely bracketed the "true" bond length, which they estimated to be ca. 1.295 Å. It is thus noteworthy that the EOM-CCSD/aug-cc-pVDZ optimized structure of this state of (1*R*,4*R*)-norbornenone exhibits a C=O bond length of 1.296 Å, in nearly perfect agreement with the estimate by Pecul and Ruud. All other geometrical parameters, including the C=C distance and key dihedral angles, are essentially identical between EOM-CCSD and both B3LYP and CAM-B3LYP.

Similarly good agreement in the structures obtained with DFT and CC methods is found for the second and third excited states of (1*R*,4*R*)-norbornenone. According to EOM-CCSD/aug-cc-pVDZ, these states exhibit a contraction of the C=O bond to 1.181 Å (second excited state) and 1.189 Å (third) as compared to 1.215 Å in the ground state. The C=C distance, however, increases in both states to 1.429 Å (second) and 1.404 Å (third) vs. 1.358 Å in the ground state, indicating that these states involve $\pi \rightarrow \pi^*$ transition character. At the same time, the carbonyl distorts only slightly from planarity with the C−C−C plane to which it is connected in both states — slightly away from the bridgehead carbon atom in the second excited state and slightly toward the bridgehead in the third. The largest (but still minor) difference in the EOM-CCSD vs. B3LYP and CAM-B3LYP structures arises for the C=C distance, with the DFT methods yielding 1.446 Å and 1.448 Å respectively, for

the second excited state and 1.387 Å and 1.385 Å for the third.

For (*S*)-3-methylcyclopentanone we again find that the B3LYP and EOM-CCSD optimized structures of all three states — ground and first two excited states — are very similar, with the largest difference occurring in the C=O bond length in the first ($n \rightarrow \pi^*$) excited state: EOM-CCSD yields a bond length of 1.313 Å, only 0.017 Å longer than that given by B3LYP. In addition, EOM-CCSD yields slightly greater pyramidalization around the carbonyl carbon in the first excited state, with the C=O moiety bent away from the C−C−C plane by 37° vs. 33° with B3LYP. For the second excited state, the structures produced by EOM-CCSD and B3LYP are essentially identical, with both methods in agreement that the C=O bond distance is *shorter* than in the ground state (1.194 Å vs. 1.217 Å at the EOM-CCSD/aug-cc-pVDZ level of theory) and that no pyramidalization of the carbonyl carbon occurs. Analysis of the EOM-CCSD excited-state wave function and TDDFT orbital transition vectors for this state reveal that it exhibits strong Rydberg character involving the 3*s* orbital of the oxygen atom. Thus, the ground and second excited state structures are similar, apart from the contraction of the C=O bond.

Absorption and emission data computed using EOM-CCSD for (1*R*,4*R*)-norbornenone and (*S*)-3-methylcyclopentanone using the above optimized structures are given in Tables 6.1 and 6.2, respectively. For the first excited state of (1*R*,4*R*)-norbornenone, the choice of optimized ground- and excited-state geometries makes little difference, with the largest discrepancy occurring for the dipole strength: 1716×10^{-40} cgs using the CC geometries vs. 1752×10^{-40} cgs using the DFT geometries. However, even this shift is minor and ultimately has minimal

impact on the resulting absorption dissymetry factor. The emission data for the first excited state, on the other hand, show a larger dependence on the choice of optimized excited-state geometry with the B3LYP structures yielding significantly larger values than with the EOM-CCSD structures for the excitation energy (2.94 vs. 2.85 eV, respectively), rotatory strength (21.5 vs. 12.5 $\times$ 10^{-40} cgs) and dipole strength (2389 vs. 1338 $\times$ 10^{-40} cgs). The source of this difference lies, of course, in the longer C=O bond distance (and somewhat less on the larger pyramidalization of the carbonyl carbon) predicted by EOM-CCSD. However, the errors in the rotatory and dipole strengths introduced by the use of the B3LYP geometry largely cancel in the emission dissymmetry factor, which differs by ca. 1.5×10^{-3} cgs between the two structures. In addition, the dissymmetry factor decreases by a factor of two between absorption and emission, which reflects the structural changes noted above.

For the second excited state of (1*R*,4*R*)-norbornenone, somewhat larger differences appear between the use of CC or B3LYP geometries. For the second state, for example, while the EOM-CCSD excitation energies are identical for the two structures, the rotatory strengths and dipole strengths are more sensitive to small perturbations in the structure, leading to a sizeable quantitative discrepancy in the corresponding dissymmetry factor of 19.74×10^{-3} cgs between the structures. For the corresponding emission, the shifts in the excitation energy (0.35 eV), rotatory strength (23.87×10^{-40} cgs), and dipole strengths (3870×10^{-40} cgs) are even larger, though these mostly cancel in the dissymmetry factor, which differs by less than 3×10^{-3} cgs. The third excited state, on the other hand, is better behaved, with the largest differences between the CC and B3LYP geometries appearing in the rotatory strength of the

Table 6.1: EOM-CCSD/aug-cc-pVDZ electronic transition data for the ground and first three excited states of (1*R*,4*R*)-norbornenone. Absorption data were computed using the CCSD or B3LYP optimized ground-state optimized geometries, while emission data were obtained at the corresponding EOM-CCSD or B3LYP (TD-DFT) structures. Reported rotational strengths were computed using the length representation of the electric dipole operator.

Geometry	Transition	Energy (eV)	RS (10^{-40} cgs)	DS (10^{-40} cgs)	g_x (10^{-3} cgs)
CCSD	G $\rightarrow$ 1	4.26	34.06	1716	79.40
B3LYP	G $\rightarrow$ 1	4.29	34.63	1752	79.08
CCSD	G $\leftarrow$ 1	2.85	12.52	1338	37.44
B3LYP	G $\leftarrow$ 1	2.94	21.46	2389	35.93
CCSD	G $\rightarrow$ 2	6.00	-8.380	1042	-32.18
B3LYP	G $\rightarrow$ 2	6.00	-10.06	774.6	-51.92
CCSD	G $\leftarrow$ 2	4.58	61.18	20620	11.87
B3LYP	G $\leftarrow$ 2	4.93	37.31	16750	8.910
CCSD	G $\rightarrow$ 3	6.31	28.26	27250	4.149
B3LYP	G $\rightarrow$ 3	6.33	29.78	26210	4.544
CCSD	G $\leftarrow$ 3	5.62	8.128	21600	1.505
B3LYP	G $\leftarrow$ 3	5.76	19.00	25250	3.011

emission (8.128×10^{-40} vs. 19.00×10^{-40} cgs, respectively). This leads to a factor of two difference between the dissymmetry factor for the transition, but still only a small shift in absolute terms (1.506×10^{-3} cgs).

Similar observations may be made for the (*S*)-3-methylcyclopentanone absorption and emission data collected in Table 6.2. For example, the excitation energies for both the first and second excited states shift by less than 0.04 eV between the two choices of optimized geometries. The rotatory strengths exhibit similarly minor changes, and it is noteworthy that the two states give opposite-sign ECD signals. The dipole strengths exhibit somewhat larger differences, though the transition to the first excited state remains weak regardless of the

choice of structure, as expected for an $n \rightarrow \pi^*$ transition. The dipole strength for the second excited state is two orders of magnitude larger than for the first state, again as expected due to the similarity with the ground-state structure, but the choice of optimized geometries leads to a shift of less than 1% in the computed values. The impact of the observed shifts on the absorption dissymmetry factors, however, are, again relatively minor, particularly for the second excited state. Furthermore, the small structural changes between the ground and second state described above are also reflected in the small difference in the absorption and emission dissymmetry factors (3.524 vs. 3.250 $\times 10^{-3}$ cgs, respectively, using the EOM-CCSD geometries), whereas the difference is more than an order of magnitude larger for the first excited state (-478.3 vs. -27.91 $\times 10^{-3}$ cgs) due to the concomitantly larger geometry distortions.

Table 6.2: EOM-CCSD/aug-cc-pVDZ electronic transition data for the ground and first two excited states of (*S*)-3-methylcyclopentanone. Absorption data were computed using the CCSD or B3LYP optimized ground-state optimized geometries, while emission data were obtained at the corresponding EOM-CCSD or B3LYP (TD-DFT) structures. Reported rotational strengths were computed using the length representation of the electric dipole operator.

Geometry	Transition	Energy (eV)	RS (10^{-40} cgs)	DS (10^{-40} cgs)	g_x (10^{-3} cgs)
CCSD	G $\rightarrow$ 1	4.25	-8.884	74.29	-478.3
B3LYP	G $\rightarrow$ 1	4.28	-8.448	66.83	-505.7
CCSD	G $\leftarrow$ 1	3.04	-6.882	986.5	-27.91
B3LYP	G $\leftarrow$ 1	3.21	-6.973	849.5	-32.83
CCSD	G $\rightarrow$ 2	6.32	8.826	10020	3.524
B3LYP	G $\rightarrow$ 2	6.32	8.285	9930	3.337
CCSD	G $\leftarrow$ 2	6.05	8.380	10310	3.250
B3LYP	G $\leftarrow$ 2	6.11	7.738	9204	3.363

Although we do not have sufficient data to separate the errors introduced by the use of the approximate DFT vs. EOM-CC optimized excited-state structures as compared to errors associated with the use of DFT vs. EOM-CC transition strengths, we conclude from the above observations that the DFT optimized structures are sufficient for obtaining reasonably accurate EOM-CC dipole strengths, rotatory strengths, and especially dissymmetry factors for most cases. Thus, we have made use of B3LYP/aug-cc-pVDZ ground- and excited-state optimized geometries for subsequent EOM-CCSD and CAM-B3LYP calculations for all of the remaining test cases, though we necessarily keep in mind that some cases may be problematic and errors associated with the excited-state geometries may occur.

6.3.2 (1*R*,4*R*)-α-Fenchocampherone

Table 6.3 reports electronic transition data for the ground and first three excited states of (1*R*,4*R*)-α-fenchocampherone. The B3LYP/aug-cc-pVDZ geometries (coordinates given in Appendix A) follow the typical trends for such ketones. Due to its $n \rightarrow \pi^*$ character, the first excited state exhibits an extension of the C=O bond from 1.212 Å to 1.286 Å, as well as bending of the carbonyl away from the bridgehead carbon. The second and third states, on the other hand, involve significant Rydberg character associated with the oxygen atom, and thus their structures are closer to that of the ground state, with C=O bond lengths of 1.192 and 1.190 Å, respectively, and planarity around the carbonyl.

As expected, B3LYP typically underestimates transition energies relative to EOM-CCSD,

Table 6.3: Electronic transition data for the ground and first three excited states of (1*R*,4*R*)-α-fenchocampherone obtained using EOM-CCSD, B3LYP, and CAM-B3LYP with the aug-cc-pVDZ basis set. Reported rotational strengths were obtained using the length representation of the electric dipole operator.

Method	Transition	Energy (eV)	RS (10^{-40} cgs)	DS (10^{-40} cgs)	g_x (10^{-3} cgs)
EOM-CCSD	G $\rightarrow$ 1	4.31	5.810	126.1	184.3
B3LYP	G $\rightarrow$ 1	4.17	8.038	206.7	155.5
CAM-B3LYP	G $\rightarrow$ 1	4.26	5.822	142.1	163.8
EOM-CCSD	G $\leftarrow$ 1	3.04	1.147	1279	3.586
B3LYP	G $\leftarrow$ 1	2.96	2.565	1118	9.180
CAM-B3LYP	G $\leftarrow$ 1	3.03	1.676	1092	6.141
EOM-CCSD	G $\rightarrow$ 2	6.32	6.889	8311	3.316
B3LYP	G $\rightarrow$ 2	5.57	-4.553	3838	-4.746
CAM-B3LYP	G $\rightarrow$ 2	6.36	5.881	6971	3.375
EOM-CCSD	G $\leftarrow$ 2	6.01	6.642	8482	3.132
B3LYP	G $\leftarrow$ 2	5.30	-5.557	4703	-4.726
CAM-B3LYP	G $\leftarrow$ 2	6.06	5.463	7055	3.097
EOM-CCSD	G $\rightarrow$ 3	6.82	-0.1304	688.2	-0.7576
B3LYP	G $\rightarrow$ 3	6.00	1.701	762.3	8.926
CAM-B3LYP	G $\rightarrow$ 3	6.84	0.5237	839.9	2.494
EOM-CCSD	G $\leftarrow$ 3	6.48	0.01313	1202	0.04369
B3LYP	G $\leftarrow$ 3	5.72	2.183	962.6	9.072
CAM-B3LYP	G $\leftarrow$ 3	6.52	0.8763	1124	3.118

though CAM-B3LYP largely corrects this discrepancy for the three excited states considered here. More interesting, however, is the corresponding pattern in the dipole and rotatory strengths, with CAM-B3LYP values typically shifted back toward their EOM-CCSD counterparts as compared to B3LYP. For the absorption to the second excited state, for example, EOM-CCSD yields a dipole strength of 8311 $\times 10^{-40}$ cgs, while B3LYP predicts a value of less than half that of 3838 $\times 10^{-40}$ cgs. CAM-B3LYP, however, yields a value much closer to EOM-CCSD at 6971 $\times 10^{-40}$ cgs. Similarly for rotatory strengths, CAM-B3LYP tends

to fall closer to EOM-CCSD than B3LYP, *e.g.*, for the absorption to the first excited state where CAM-B3LYP and EOM-CCSD give values near 5.8 $\times 10^{-40}$ cgs, while B3LYP yields a value roughly 40% larger at 8.0 $\times 10^{-40}$ cgs. Furthermore, for the absorption and emission between the ground and second excited state, B3LYP yields a qualitatively incorrect rotatory strength — and thus an incorrect dissymmetry factor — with a prediction of a negative value vs. the positive values given by both EOM-CCSD and CAM-B3LYP.

An additional point of disagreement appears between coupled cluster and density functional methods for (1*R*,4*R*)-α-fenchocampherone. In particular, for the absorption from the ground state to the third excited state, the rotatory strength is negative according to EOM-CCSD and positive according to both B3LYP and CAM-B3LYP — though all three methods predict the transition strength to be small — leading, of course, to opposite sign dissymmetry factors between CC and DFT. Finally, we note that, while the choice of length vs. velocity representations of the electric dipole operator makes little difference for most of the EOM-CCSD predictions, the emission from the first excited state exhibits a qualitative discrepancy between the two. The length representation (Table 6.3) gives a value of +1.147 $\times 10^{-40}$ cgs (in agreement with both B3LYP and CAM-B3LYP), while the velocity representation gives -3.493 $\times 10^{-40}$ cgs. (Velocity representation data are provided for all compounds in Appendix A.)

6.3.3 β-Hydrindanone

Table 6.4 reports CC and DFT electronic transition data for (1*R*,5*S*)-*cis*-β-hydrindanone, which exhibits similar patterns to those of (1*R*,4*R*)-α-fenchocampherone in that CAM-B3LYP typically yields excitation energies, dipole strengths, and rotatory strengths closer to EOM-CCSD than does B3LYP. Like (1*R*,4*R*)-α-fenchocampherone, the first excited state is largely of $n \rightarrow \pi^*$ character, while the second and third states are more diffuse. This is borne out by their structures: the first excited state exhibits a C=O bond length of 1.297 Å, more than 0.08 Å longer than that of the ground state, while the second and third excited states have C=O bonds of 1.198 and 1.197 Å, respectively. The most significant discrepancy among the three methods occurs for the second excited state, for which B3LYP yields negative rotatory strengths in both absorption and emission, whereas EOM-CCSD and CAM-B3LYP give positive rotatory strengths for this state. Examination of the velocity gauge data for emission from the second excited state reveals a change in sign for the CAM-B3LYP rotatory strength, bringing it in agreement with the B3LYP results. However, the CAM-B3LYP and EOM-CCSD rotatory strengths are very small - less than 1 $\times 10^{-40}$ cgs in magnitude - for both gauge representations, and the CAM-B3LYP data is much closer to EOM-CCSD than B3LYP despite differences in sign.

Similarly, Table 6.5 reports transition data for the first excited state of (*S*,*S*)-*trans*-β-hydrindanone. (Unlike (1*R*,4*R*)-α-fenchocampherone and (1*R*,5*S*)-*cis*-β-hydrindanone, we were unable to optimize higher lying states for this molecule.) Like its *cis* counterpart, the first excited state is characterized by an $n \rightarrow \pi^*$ transition, resulting in extension of the C=O

Table 6.4: Electronic transition data for the ground and first three excited states of (1*R*,5*S*)-*cis*-β-hydrindanone obtained using EOM-CCSD, B3LYP, and CAM-B3LYP with the aug-cc-pVDZ basis set. Reported rotational strengths were obtained using the length representation of the electric dipole operator.

Method	Transition	Energy (eV)	RS (10^{-40} cgs)	DS (10^{-40} cgs)	g_x (10^{-3} cgs)
EOM-CCSD	G $\rightarrow$ 1	4.26	8.220	76.17	431.7
B3LYP	G $\rightarrow$ 1	4.14	11.59	135.7	341.6
CAM-B3LYP	G $\rightarrow$ 1	4.22	8.725	83.99	415.5
EOM-CCSD	G $\leftarrow$ 1	3.23	7.245	803.4	36.07
B3LYP	G $\leftarrow$ 1	3.17	9.734	743.0	52.41
CAM-B3LYP	G $\leftarrow$ 1	3.25	8.084	691.3	46.78
EOM-CCSD	G $\rightarrow$ 2	6.32	0.6181	9016	0.2743
B3LYP	G $\rightarrow$ 2	5.61	-4.092	5104	-3.207
CAM-B3LYP	G $\rightarrow$ 2	6.34	0.3677	8063	0.1824
EOM-CCSD	G $\leftarrow$ 2	6.09	0.8460	8082	0.4187
B3LYP	G $\leftarrow$ 2	5.41	-5.350	5026	-4.257
CAM-B3LYP	G $\leftarrow$ 2	6.11	0.1108	7145	0.06203
EOM-CCSD	G $\rightarrow$ 3	6.77	7.342	3311	8.870
B3LYP	G $\rightarrow$ 3	5.98	6.096	3114	7.831
CAM-B3LYP	G $\rightarrow$ 3	6.77	6.808	3579	7.608
EOM-CCSD	G $\leftarrow$ 3	6.48	6.099	3366	7.248
B3LYP	G $\leftarrow$ 3	5.72	8.896	4477	7.948
CAM-B3LYP	G $\leftarrow$ 3	6.49	6.440	3876	6.646

bond from 1.212 Å to 1.295 Å. Furthermore, the rotatory strengths, dipole strengths, and dissymmetry factors for the first excited state of both *cis* and *trans* isomers of β-hydrindanone compare closely, *e.g.*, at the EOM-CCSD/aug-cc-pVDZ level of theory, the absorption and emission symmetry factors of *cis* (*trans*) isomers are ($\times 10^{-40}$ cgs) 431.7 (390.7) and 36.07 (34.87), respectively, which suggests that their absorption (CD) and emission (CPL) signatures will be similar. This observation agrees with Pritchard and Autschbach's analysis[165] of the vibronic structure of the first excited state of (1*R*,5*S*)-*cis*-β-hydrindanone, *viz.* that

the CPL emission signature is primarily due to the chirality around the carbonyl moiety.

Table 6.5: Electronic transition data for the ground and first excited state of (*S*,*S*)-*trans*-β-hydrindanone obtained using EOM-CCSD, B3LYP, and CAM-B3LYP with the aug-cc-pVDZ basis set. Reported rotational strengths were obtained using the length representation of the electric dipole operator.

Method	Transition	Energy (eV)	RS (10^{-40} cgs)	DS (10^{-40} cgs)	g_x (10^{-3} cgs)
EOM-CCSD	G $\rightarrow$ 1	4.27	11.32	115.9	390.7
B3LYP	G $\rightarrow$ 1	4.14	15.64	213.2	293.5
CAM-B3LYP	G $\rightarrow$ 1	4.23	12.10	122.7	394.2
EOM-CCSD	G $\leftarrow$ 1	3.20	7.738	887.6	34.87
B3LYP	G $\leftarrow$ 1	3.13	11.24	833.4	53.93
CAM-B3LYP	G $\leftarrow$ 1	3.21	8.849	749.4	47.23

6.3.4 *trans*-Bicyclo[3.3.0]octane-3,7-dione

The ground state of *trans*-bicyclo[3.3.0]octane-3,7-dione has C_{2h} point-group symmetry and is thus achiral. However, $n \rightarrow \pi^*$ excitation results in elongation of one of its C=O bonds from 1.209 Å to 1.292 Å, as well as puckering of the carbonyl away from planarity. This puckering can proceed in either direction off the C_2 symmetry axis and toward the horizontal plane of the ground state, yielding a non-symmetric, and thus chiral, structure. The two resulting enantiomers may be labelled as either *M* or *P* in relation to the central, twisted C−C bond joining the two cyclopentanone rings. The dipole strength of the absorption is relatively large, as shown in Table 6.6, though the corresponding rotatory strength and dissymmetry factor are both zero in the Franck-Condon (vertical transition) approximation. Emission from the chiral excited state, however, involves significant dipole and rotatory

strengths, and the latter is predicted to be negative for the P enantiomer and positive for the M enantiomer. As observed for the other systems discussed above, CAM-B3LYP gives a value between EOM-CCSD and B3LYP for the rotatory strengths, though EOM-CCSD and B3LYP agree somewhat better for the dipole strengths in this case.

The second excited-state of *trans*-bicyclo[3.3.0]octane-3,7-dione, however, is primarily of oxygen 3s-type Rydberg character and thus retains the same C_{2h} symmetry of the ground state. In addition, the excited-state character corresponds to a ^1B_g state, which is a dipole-forbidden transition from the ^1A_g ground state (as well as an allowed, but essentially zero magnetic dipole-transition), as can be seen in Table 6.6. (We further note that all three states considered here have been confirmed as minima on their respective potential energy surfaces.)

6.3.5 β,γ-Enones

In addition to (1R,4R)-norbornenone discussed earlier, we considered two additional β,γ-enones, (1R)-7-methylenebicyclo[2.2.1]heptan-2-one and (1S)-2-methylenebicyclo[2.2.1]heptan-7-one, both of which were also analyzed by Pecul and Ruud[148] for comparison with earlier experimental data.[166] They reported that these two molecules exhibit two minima on the lowest $n \rightarrow \pi^*$ potential energy surface, distinguished by the direction of pyramidalization of the C=O moiety either away from the C=C bond (to which they referred as **E1**) or toward the C=C bond (**E2**). We have identified these same structures for both (1R)-7-methylenebi-

Table 6.6: Electronic transition data for the ground and first two excited states of *trans*-bicyclo[3.3.0]octane-3,7-dione obtained using EOM-CCSD, B3LYP, and CAM-B3LYP with the aug-cc-pVDZ basis set. Reported rotational strengths were obtained using the length representation of the electric dipole operator.

Method	Transition	Energy (eV)	RS (10^{-40} cgs)	DS (10^{-40} cgs)	g_x (10^{-3} cgs)
EOM-CCSD	G $\rightarrow$ 1 (P/M)	4.26	—	400.2	—
B3LYP	G $\rightarrow$ 1 (P/M)	4.07	—	1040.	—
CAM-B3LYP	G $\rightarrow$ 1 (P/M)	4.20	—	426.4	—
EOM-CCSD	G $\leftarrow$ 1 (P)	3.23	-9.645	943.0	-40.91
B3LYP	G $\leftarrow$ 1 (P)	3.14	-17.01	1001	-67.94
CAM-B3LYP	G $\leftarrow$ 1 (P)	3.24	-11.04	807.6	-54.68
EOM-CCSD	G $\leftarrow$ 1 (M)	3.23	9.645	943.0	40.91
B3LYP	G $\leftarrow$ 1 (M)	3.14	17.01	1001	67.94
CAM-B3LYP	G $\leftarrow$ 1 (M)	3.24	11.04	807.6	54.68
EOM-CCSD	G $\rightarrow$ 2	4.31	—	—	—
B3LYP	G $\rightarrow$ 2	4.19	—	—	—
CAM-B3LYP	G $\rightarrow$ 2	4.26	—	—	—
EOM-CCSD	G $\leftarrow$ 2	4.02	—	—	—
B3LYP	G $\leftarrow$ 2	3.92	—	—	—
CAM-B3LYP	G $\leftarrow$ 2	4.00	—	—	—

cyclo[2.2.1]heptan-2-one and (1S)-2-methylenebicyclo[2.2.1]heptan-7-one, as well as a second valence excited state of each molecule with mixed $n \rightarrow \pi^*$ and $\pi \rightarrow \pi^*$ character. In both molecules, this latter state exhibits the same pyramidalization around the C=O as its **E1** counterpart, but much more pronounced elongation of the C=C bond, *e.g.*, in (1S)-2-methylenebicyclo[2.2.1]heptan-7-one, the C=C bond is 1.335 Å in the ground state, 1.350 Å in **E1**, and 1.384 Å in the second excited state. The EOM-CC and DFT vertical electronic transition properties for these states are given in Tables 6.7 and 6.8.

In agreement with Pecul and Ruud,[148] we find that the vertical absorption from the ground state of (1R)-7-methylenebicyclo[2.2.1]heptan-2-one exhibits a positive rotatory strength,

Table 6.7: Electronic transition data for the ground and first two excited states of (1R)-7-methylenebicyclo[2.2.1]heptan-2-one obtained using EOM-CCSD, B3LYP, and CAM-B3LYP with the aug-cc-pVDZ basis set. Reported rotational strengths were obtained using the length representation of the electric dipole operator.

Method	Transition	Energy (eV)	RS (10^{-40} cgs)	DS (10^{-40} cgs)	g_x (10^{-3} cgs)
EOM-CCSD	G $\rightarrow$ 1	4.31	18.74	1149	65.25
B3LYP	G $\rightarrow$ 1	4.12	30.19	2907	41.54
CAM-B3LYP	G $\rightarrow$ 1	4.24	21.84	1525	57.31
EOM-CCSD	G $\leftarrow$ 1 (E1)	2.99	9.357	1311	28.55
B3LYP	G $\leftarrow$ 1 (E1)	2.87	18.08	1202	60.19
CAM-B3LYP	G $\leftarrow$ 1 (E1)	2.96	12.67	1124	45.07
EOM-CCSD	G $\leftarrow$ 1 (E2)	3.01	-0.8767	2884	-1.216
B3LYP	G $\leftarrow$ 1 (E2)	2.88	-0.2693	4114	-0.2619
CAM-B3LYP	G $\leftarrow$ 1 (E2)	2.97	-1.447	3055	-1.895
EOM-CCSD	G $\rightarrow$ 2	6.25	-41.23	4988	-33.06
B3LYP	G $\rightarrow$ 2	5.59	-22.05	3825	-23.07
CAM-B3LYP	G $\rightarrow$ 2	6.25	-48.78	7087	-27.53
EOM-CCSD	G $\leftarrow$ 2	5.14	6.892	899.9	30.64
B3LYP	G $\leftarrow$ 2	3.48	2.061	387.6	21.27
CAM-B3LYP	G $\leftarrow$ 2	4.41	5.529	811.9	27.24

while that from the ground state of (1S)-2-methylenebicyclo[2.2.1]heptan-7-one is negative. EOM-CCSD yields significantly smaller absolute values of both rotatory and dipole strengths for the absorption than either B3LYP or CAM-B3LYP, but somewhat larger absorption dissymmetry factors. Interestingly, and perhaps only coincidentally, the EOM-CC absorption dissymmetry factors for (1R)-7-methylenebicyclo[2.2.1]heptan-2-one and (1S)-2-methylenebicyclo[2.2.1]heptan-7-one are almost identical in magnitude (but opposite in sign).

On emission, the **E1** and **E2** structures of (1R)-7-methylenebicyclo[2.2.1]heptan-2-one exhibit positive and (small) negative rotatory strengths, respectively, while the dipole strength of **E2** is more than a factor of two larger than that of **E1** with EOM-CCSD. This leads

Table 6.8: Electronic transition data for the ground and first two excited states of (1*S*)-2-methylenebicyclo[2.2.1]heptan-7-one obtained using EOM-CCSD, B3LYP, and CAM-B3LYP with the aug-cc-pVDZ basis set. Reported rotational strengths were obtained using the length representation of the electric dipole operator.

Method	Transition	Energy (eV)	RS (10^{-40} cgs)	DS (10^{-40} cgs)	g_x (10^{-3} cgs)
EOM-CCSD	G $\rightarrow$ 1	4.34	-15.26	947.1	-64.46
B3LYP	G $\rightarrow$ 1	4.10	-25.97	3004	-34.58
CAM-B3LYP	G $\rightarrow$ 1	4.23	-18.56	1408	-52.72
EOM-CCSD	G $\leftarrow$ 1 (E1)	2.42	-6.819	1788	-15.25
B3LYP	G $\leftarrow$ 1 (E1)	2.15	-13.38	1202	-44.55
CAM-B3LYP	G $\leftarrow$ 1 (E1)	2.30	-9.388	1395	-26.91
EOM-CCSD	G $\leftarrow$ 1 (E2)	2.60	3.413	2995	4.558
B3LYP	G $\leftarrow$ 1 (E2)	2.43	2.521	3923	2.571
CAM-B3LYP	G $\leftarrow$ 1 (E2)	2.52	3.334	3050.	4.372
EOM-CCSD	G $\rightarrow$ 2	6.10	30.78	8588	14.34
B3LYP	G $\rightarrow$ 2	5.45	25.00	7262	13.77
CAM-B3LYP	G $\rightarrow$ 2	6.07	57.13	36510	6.258
EOM-CCSD	G $\leftarrow$ 2	4.55	1.023	579.4	7.063
B3LYP	G $\leftarrow$ 2	2.89	-11.90	975.5	-48.78
CAM-B3LYP	G $\leftarrow$ 2	3.82	-0.9672	781.7	-4.949

to a nearly two order of magnitude difference in the CPL dissymmetry factors between the two structures. For (1*S*)-2-methylenebicyclo[2.2.1]heptan-7-one, the signs of the rotatory strengths are reversed: the **E1** structure gives a negative transition, while **E2** gives a positive transition. The dipole strengths are significantly larger for **E2** than **E1** for (1*S*)-2-methylenebicyclo[2.2.1]heptan-7-one, though the difference is not so great as for (1*R*)-7-methylenebicyclo[2.2.1]heptan-2-one.

Schippers *et al.*[166] measured both polarized and unpolarized absorption and fluorescence spectra of these compounds in *n*-heptane (and in 1:3 methylcyclohexane/isopentane for the emission spectra of (1*S*)-2-methylenebicyclo[2.2.1]heptan-7-one) at ambient temperature.

For the $n \rightarrow \pi^*$ absorption transition of (1R)-7-methylenebicyclo[2.2.1]heptan-2-one they reported a dipole strength of 1790×10^{-40} cgs and a rotatory strength of 20.5×10^{-40} cgs, leading to a a dissymmetry factor of 45.8×10^{-3} cgs. Comparison of these data with those of Table 6.7 reveal very good agreement with CAM-B3LYP for both the dipole and rotatory strengths (1525×10^{-40} cgs and 21.84×10^{-40} cgs, respectively), but rather poor agreement with B3LYP for these same values (2907×10^{-40} cgs and 30.19×10^{-40} cgs, respectively). However, the errors in the latter mostly cancel in the dissymmetry factor, resulting in much better agreement with experiment by B3LYP (41.54×10^{-3} cgs) than by CAM-B3LYP (57.31×10^{-3} cgs). EOM-CCSD, on the other hand, gives reasonable agreement with experiment for the rotatory strength (18.74×10^{-40} cgs), but underestimates the dipole strength resulting in much too large of a dissymetry factor (65.25×10^{-3} cgs).

For (1S)-2-methylenebicyclo[2.2.1]heptan-7-one, the comparison with experiment is similar. For the $n \rightarrow \pi^*$ absorption, Schippers *et al.*[166] report a dipole strength of 1870×10^{-40} cgs, a rotatory strength of -15.2×10^{-40} cgs, and a corresponding dissymetry factor of -32.5×10^{-3} cgs. Again, CAM-B3LYP yields better agreement with experiment than B3LYP for the two transition strengths, but the errors in B3LYP mostly cancel to give rather close agreement with experiment for the dissymmetry factor: -34.58×10^{-3} cgs for B3LYP vs. -52.72×10^{-3} cgs for CAM-B3LYP. Furthermore, whereas EOM-CCSD gives (providentially) perfect agreement with experiment for the rotatory strength (-15.26×10^{-40} cgs), it underestimates the dipole strength by a factor of two, giving a g_a value that is correspondingly too large.

For the fluorescence spectra of (1R)-7-methylenebicyclo[2.2.1]heptan-2-one, Schippers *et*

al.[166] reported a dissymmetry value of 15.7×10^{-3} cgs, but they described their corresponding value for (1*S*)-2-methylenebicyclo[2.2.1]heptan-7-one of $< 3 \times 10^{-3}$ cgs as "an upper limit of the degree of circular polarization." From the (1*R*)-7-methylenebicyclo[2.2.1]heptan-2-one transition data in Table 6.7, emission from the **E1** structure gives a positive rotatory strength, and thus a positive dissymmetry factor, with EOM-CCSD giving the best agreement with experiment at 28.55×10^{-3} cgs. For (1*S*)-2-methylenebicyclo[2.2.1]heptan-7-one, emission from **E2** gives a positive rotatory strength and dissymmetry factor, with all three theoretical methods giving good agreement with the small experimental limit of g_e.

Table 6.9: Adiabatic excitation energies (in eV) at the B3LYP/aug-cc-pVDZ optimized geometries for (1*R*)-7-methylenebicyclo[2.2.1]heptan-2-one and (1*S*)-2-methylenebicyclo[2.2.1]heptan-7-one.

Transition	EOM-CCSD	B3LYP	CAM-B3LYP
(1*R*)-7-methylenebicyclo[2.2.1]heptan-2-one			
1 (E1)	3.83	3.76	3.90
1 (E2)	3.88	3.79	3.94
2	6.51	4.91	5.92
(1*S*)-2-methylenebicyclo[2.2.1]heptan-7-one			
1 (E1)	3.74	3.50	3.73
1 (E2)	3.68	3.56	3.71
2	6.01	4.44	5.43

However, as pointed out by Pecul and Ruud,[148] the dominance of **E1** vs. **E2** in the fluorescence and CPL spectra depends upon which structure is lower in energy upon *adiabatic* emission. The corresponding energy differences between the ground state and each of **E1** and **E2** (as well as the second excited state) of (1*R*)-7-methylenebicyclo[2.2.1]heptan-2-one and (1*S*)-2-methylenebicyclo[2.2.1]heptan-7-one are given in Table 6.9. All three methods

agree that conformer **E1** of (1*R*)-7-methylenebicyclo[2.2.1]heptan-2-one lies slightly lower in energy than **E2**, with EOM-CCSD predicting the largest difference of only 0.05 eV. For (1*S*)-2-methylenebicyclo[2.2.1]heptan-7-one, however, both EOM-CCSD and CAM-B3LYP predict **E2** to be lower in energy than **E1** (by 0.06 eV, according to EOM-CCSD), whereas B3LYP predicts **E1** to be lower (also by 0.06 eV). Thus, B3LYP would predict a *negative* dissymmetry factor for the polarized emission in (1*S*)-2-methylenebicyclo[2.2.1]heptan-7-one, in disagreement with both the experimentally determined limit and the EOM-CCSD and CAM-B3LYP predictions.

6.4 Conclusions

We have carried out the first EOM-CCSD calculations of CPL rotatory strengths for comparison to results from both DFT (B3LYP and CAM-B3LYP) and experiment using a series of eight chiral ketones as a test set. For each case, we obtained optimized structures for up to three excited states, including both valence and Rydberg-type states — the latter being CPL transitions which have not been examined theoretically before. For two of the test molecules — (1*R*,4*R*)-norbornenone and (*S*)-3-methylcyclopentanone — we compared the efficacy of optimizing the excited-state geometries using B3LYP (TD-DFT) vs. EOM-CCSD in order to streamline the determination of the corresponding transition strengths. We observed only minimal differences between the structures obtained using each method, as well as acceptably small differences in vertical transition properties calculated with EOM-CCSD

using the two sets of geometries. Thus, we pursued only B3LYP ground- and excited-state geometry optimizations for the remaining six molecules.

For most of the cases considered here, EOM-CCSD and CAM-B3LYP exhibited relatively good agreement, while B3LYP typically underestimated excitation energies and overestimated rotatory strengths. For one case, (1*R*,4*R*)-α-fenchocampherone, EOM-CCSD and the DFT methods disagreed on the sign of the rotatory strength for the absorption to the third excited state; all other cases exhibited (at least) qualitative agreement between CC and CAM-B3LYP. The choice of length vs. velocity representation of the electric dipole operator made little qualitative or quantitative difference for almost all cases, the only exceptions being the CPL emission from the first excited state of (1*R*,4*R*)-α-fenchocampherone and from the second ecited state of (1*R*,5*S*)-*cis*-β-hydrindanone.

One test case, *trans*-bicyclo[3.3.0]octane-3,7-dione, exhibits the intruiguing phenomenon of having a C_{2h}-symmetric (and thus achiral) ground state and second excited state, but a C_1 non-symmetric (chiral) first excited state. Thus, the vertical transition from the ground state to the first excited state has a zero rotatory strength, but we predict the corresponding emission to exhibit a strong CPL signal. While the inclusion of vibronic effects in the simulation would lead to non-zero rotatory strengths for the absorption, they would likely remain weak. To our knowledge, this has not yet been investigated experimentally.

Finally we compared theoretical and experimental ECD and CPL spectral data for two β,γ-enones, (1*R*)-7-methylenebicyclo[2.2.1]heptan-2-one and (1*S*)-2-methylenebicyclo[2.2.1]heptan-7-one, which exhibit two conformers on the first excited-state potential energy surface.

While CAM-B3LYP provides closer agreement with experiment for both dipole and rotatory absorption strengths than B3LYP, the latter yields better agreement for the corresponding dissymmetry factor due to cancellation of errors. In addition, for these two compunds, EOM-CCSD significantly underestimates the dipole strength of the absorption, resulting in a concomitant overestimation of the related dissymmetry factor. On the other hand, EOM-CCSD yields near-perfect (and fortuitous) agreement with the experimental rotatory strength for (1*S*)-2-methylenebicyclo[2.2.1]heptan-7-one. Finally, both CAM-B3LYP and EOM-CCSD predict the same energy ordering of the two conformers of the first excited state of (1*S*)-2-methylenebicyclo[2.2.1]heptan-7-one, yielding good agreement with experiment for the sign of the CPL transition strength, while B3LYP disagrees qualitatively.

6.5 Acknowledgments

This research was supported by grants CHE-1058420 and ACI-1147794 from the U.S. National Science Foundation.

Chapter 7

Conclusions

In Chapter 2, the essential equations for coupled cluster linear response[8,11] were laid forth. The formalism allows for quantum chemical predictions of molecular optical properties,[10] which may aid greatly in assigning absolute configurations to chiral molecules. Due to the high polynomial scaling of coupled cluster, however, such calculations are limited to relatively small systems.[18–20,22–24,64]

Many chiral compounds of interest are on a very large scale, in the biomolecular and biological regime, and often they feature more than one chiral center or axis. A standard CCLR program unfortunately may not be applied to such systems - even with sufficient time and memory, the calculation may not be practical. Simulating properties in solution, another goal for the CCLR methods, also faces the scaling wall of coupled cluster. A straightforward approach for a solvated system is to explicitly include several solvent molecules in the cal-

culation, which will quickly increase the computational cost. Furthermore, an average over several configurations is likely necessary for physically meaningful results, adding yet more computational demand.

To apply CCLR methodology to problems on a larger scale, reduced-scaling techniques and approaches must be incorporated into the calculations. As a step in that direction, local coupled cluster polarizabilities, optical rotations, and excited state data have been calculated with different local correlation approaches. In Chapter 3, the LOO-CCD work[59] built upon previous efforts by the Crawford group,[56,58,179] further testing PAO orbital domains based upon the CPHF equations. Including an orbital-optimization procedure in the calculation, an effort towards a gauge-invariant coupled cluster method, had little influence on the localization error introduced by the PAO approach. Conclusions on the performance of the PAO coupled cluster method remained unchanged - simple systems are more amenable to local methods, while more complex structures require larger virtual spaces, resulting in less computational savings.

Next, the performance of the OSV, PNO, and PAO local correlation techniques was tested for coupled cluster polarizabilities and optical rotations in Chapter 4. Wavefunction distributions in each basis for a series of alkanes reveal that the PNO-basis is the most sparse - the distribution is shifted toward smaller values compared to the OSV and PNO bases. The PAO and OSV distributions are similar with regard to sparsity, but the OSV plots feature a narrower distribution. Comparing the distributions of the ground state amplitudes to the perturbed amplitudes required by the CCLR function illustrate that the perturbed wave-

functions are generally less sparse than their ground state counterparts by around one order of magnitude.

The localization errors for optical rotations are often at least an order of magnitude larger than for polarizabilities. By a narrow margin, the PNO method outperforms the OSV method - more closely agreeing with the canonical value for a given truncation level. Neglecting weak pairs from the calculations causes a shift in the local property values. Both polarizabilities and optical rotations are highly sensitive to truncation of the singles; and the OSV method, especially, appears to be the most influenced by the singles contributions. For the three-dimensional structures, accurate predictions of the canonical result could only be produced when computational savings were small.

In Chapter 5, the same local correlation techniques were also applied to properties of excited states using the EOM-CCSD method.[150] Each of the local virtual spaces for the excited state wavefunctions were kept identical to that of the ground state as a general test of the methods and to ensure all states were treated in a balanced manner. For the excitation energies, good agreement is found for only the first two or three excited states in calculations where truncation is significant, with higher energy transitions being increasingly overestimated in the local calculations. For rotational and dipole strengths, the errors due to the local approach are often large. Due to cancellation of error, data for higher transitions is sometimes found in better agreement than for lower states. As the virtual space is increased, however, the strengths for the lower states tend to increase in accuracy. Following a state-specific approach,[55,104,105,132,133] which performs well for excitation energies, would likely yield better

agreement for the transition properties as well.

In addition to testing local correlation methods, the EOM-CC formalism was extended to novel property calculations, as shown in Chapter 6. Circularly polarized luminescence, the emission counterpart to electronic circular dichroism, was explored for the first time at the EOM-CCSD level. For several chiral molecules, the rotational and dipole strengths for absorption and emission were calculated for the ground and first few excited states. For one test case, *trans*-bicyclo[3.3.0]octane-3,7-dione, the ground state geometry of the molecule is found to be achiral and yields an appropriate zero rotational strength for the transition to the first excited state. The emission from the first excited state, on the other hand, gives a non-zero rotational strength due to loss of symmetry in the excited state geometry. A challenging aspect of the project was the optimization of ground and excited state geometries, and it provides an example where reduced-scaling techniques would be highly useful. While extensive tests revealed that B3LYP/aug-cc-pVDZ geometries were sufficient for accurate EOM-CCSD transition data, coupled-cluster level optimizations could become more accessible if used in conjunction with a robust, accurate local correlation scheme.

Overall, relatively little success has been found for local correlation techniques applied to the calculation of coupled cluster properties - including polarizabilities, optical rotations, and excitation data. The requisite accuracy is lost as the desired truncation and computational savings are achieved. Some avenues for improvement certainly remain, but the truncation approaches (the OSV, PNO, and PAO methods) appear to remove components of the wavefunction that are essential for accurate property results, despite having minimal effect on

the correlation energy. Hopefully, this work sets the stage for further development of novel local correlation techniques for the accurate calculation of molecular properties.

Bibliography

[1] S. Wnendt and K. Zwingenberger. *Nature*, 385(6614):303–304, January 1997.

[2] P. L. Polavarapu. *Mol. Phys.*, 91(3):551–554, November 1997.

[3] J. R. Cheeseman, M. J. Frisch, F. J. Devlin, and P. J. Stephens. *J. Phys. Chem. A*, 104:1039–1046, November 1999.

[4] P. J. Stephens, F. J. Devlin, J. R. Cheeseman, and M. J. Frisch. *J. Phys. Chem. A*, 105:5356–5371, May 2001.

[5] T. Ruud, Kenneth adn Helgaker. *Chem. Phys. Lett.*, 352:533–539, December 2001 2002.

[6] K. Ruud, P. J. Stephens, F. J. Devlin, P. R. Taylor, J. R. Cheeseman, and M. J. Frisch. *Chem. Phys. Lett.*, 373:606–614, March 2003.

[7] T. D. Crawford, M. C. Tam, and M. L. Abrams. *J. Phys. Chem. A*, 111(48):12057–12068, December 2007.

[8] H. Koch and P. Jørgensen. *J. Chem. Phys.*, 93(5):3333–3344, September 1990.

[9] R. Kobayashi, H. Koch, and P. Jørgensen. *Chem. Phys. Lett.*, 219:30–35, March 1994.

[10] T. D. Crawford. *Theor. Chem. Acc.*, 115:227–245, December 2006.

[11] O. Christiansen, P. Jørgensen, and C. Hättig. *Int. J. Quantum Chem.*, 68(1):1–52, 1998.

[12] H. R. McAlexander and T. D. Crawford. *J. Chem. Phys.*, 142:154101–1 – 154101–11, 2015.

[13] T. B. Pedersen, H. Koch, L. Boman, and A. M. Sanchez de Meras. *Chem. Phys. Lett.*, 393:319–326, June 2004.

[14] T. B. Pedersen, H. Koch, and C. Hättig. *J. Chem. Phys.*, 110(17):8318–8327, February 1999.

[15] T. B. Pedersen and B. Fernandez. *J. Chem. Phys.*, 114(16):6983–6993, February 2001.

[16] P. Lahiri, K. B. Wiberg, P. H. Vaccaro, M. Caricato, and T. D. Crawford. *Angew. Chem. Int. Ed.*, 53(5):1386–1389, January 2014.

[17] F. J. Luque, . Curutchet, C, J. Munoz-Muriedas, A. Bidon-Chanal, I. Soteras, A. Morreale, J. Gelpi, and M. Orozco. *Phys. Chem. Chem. Phys.*, 5:3827–3836, August 2003.

[18] R. J. Bartlett. *Theor. Chim. Acta*, 80:71–79, 1991.

[19] R. J. Bartlett. Coupled-cluster theory: An overview of recent developments. In D. R. Yarkony, editor, *Modern Electronic Structure Theory*, volume 2 of *Advanced Series in Physical Chemistry*, chapter 16, pages 1047–1131. World Scientific, Singapore, 1995.

[20] J. Gauss. The coupled-cluster method. In P. Schleyer, N. L. Allinger, T. Clark, J. Gasteiger, P. A. Kollman, H. F. Schaefer III, and P. R. Schreiner, editors, *Encyclopedia of Computational Chemistry*, pages 615–636. John Wiley and Sons, Chichester, 1998.

[21] T. D. Crawford and H. F. Schaefer. An introduction to coupled cluster theory for computational chemists. In K. B. Lipkowitz and D. B. Boyd, editors, *Reviews in Computational Chemistry*, volume 14, chapter 2, pages 33–136. VCH Publishers, New York, 2000.

[22] R. J. Bartlett. How and why coupled-cluster theory became the pre-eminent method in an ab initio quantum chemistry. In C. D. *et al.*, editor, *Theory and Applications of Computational Chemistry: The First Forty Years*, chapter 42, pages 1191–1221. Elsevier, New York, 2005.

[23] R. J. Bartlett and M. Musial. *Rev. Mod. Phys.*, 79:291–352, 2007.

[24] R. J. Bartlett. *Mol. Phys.*, 108(21-23):2905–2920, 2010.

[25] P. Pulay. *Chem. Phys. Lett.*, 100(2):151–154, June 1983.

[26] H. Stoll. *J. Chem. Phys.*, 97(11):8449–8454, December 1992.

[27] C. Hampel and H.-J. Werner. *J. Chem. Phys.*, 104(16):6286–6297, April 1996.

[28] K. Kitaura, E. Ikeo, T. Asada, T. Nakano, and M. Uebayasi. *Chem. Phys. Lett.*, 313: 701–706, November 1999.

[29] M. Schütz, G. Hetzer, and H.-J. Werner. *J. Chem. Phys.*, 111(13):5691–5705, October 1999.

[30] G. Hetzer, M. Schütz, H. Stoll, and H.-J. Werner. *J. Chem. Phys.*, 113(21):9443–9455, December 2000.

[31] M. Schütz. *J. Chem. Phys.*, 113(22):9986–10001, December 2000.

[32] M. Schütz and H.-J. Werner. *J. Chem. Phys.*, 114(2):661–681, January 2001.

[33] M. Schütz. *J. Chem. Phys.*, 116(20):8772–8785, May 2002.

[34] W. Li and S. Li. *J. Chem. Phys.*, 121(14):6649–6657, October 2004.

[35] D. Fedorov and K. Kitaura. *J. Chem. Phys.*, 123:134103–1 – 134103–11, October 2005.

[36] S. Li, J. Shen, W. Li, and Y. Jiang. *J. Chem. Phys.*, 125:074109–1 – 074109–10, August 2006.

[37] R. A. Mata and H.-J. Werner. *Mol. Phys.*, 105(19-22):2753–2761, November 2007.

[38] A. G. Taube and R. J. Bartlett. *J. Chem. Phys.*, 128(164101):164101–1 – 164101–17, April 2008.

[39] W. Li, P. Piecuch, and J. R. Gour. *Theory and Applications of Computational Chemistry*, pages 68–113, 2009.

[40] W. Li, P. Piecuch, J. R. Gour, and S. Li. *J. Chem. Phys.*, 131:114109–1 114109–30, September 2009.

[41] H. Stoll. *Mol. Phys.*, 108(3-4):243–248, February 2009.

[42] J. Friedrich and M. Dolg. *J. Chem. Theory Comput.*, 5(2):287–294, January 2009.

[43] F. Neese, F. Wennmohs, and A. Hansen. *J. Chem. Phys.*, 130(114108):114108–1 – 114108–18, 2009.

[44] F. Neese, A. Hanse, and D. G. Liakos. *J. Chem. Phys.*, 131(064103):064103–1 – 064103–15, August 2009.

[45] W. Li and P. Piecuch. *J. Phys. Chem. A*, 114:6721–6727, April 2010.

[46] W. Li and P. Piecuch. *J. Phys. Chem. A*, 114(33):8644–8657, 2010.

[47] D. G. Liakos, A. Hansen, and F. Neese. *J. Chem. Theory Comput.*, 7(1):76–87, 2011.

[48] D. P. Tew, B. Helmich, and C. Hättig. *J. Chem. Phys.*, 135:074107–1 – 074107–11, August 2011.

[49] J. Yang, Y. Kurashige, F. R. Manby, and G. K. Chan. *J. Chem. Phys.*, 134:044123–1 – 044123–13, January 2011.

[50] J. Yang, G. K.-L. Chan, F. R. Manby, M. Schütz, and H.-J. Werner. *J. Chem. Phys.*, 136(144105):144105–1 – 144105–16, April 2012.

[51] D. G. Liakos and F. Neese. *J. Phys. Chem. A*, 116:4801–4816, April 2012.

[52] C. Hättig, D. P. Tew, and B. Helmich. *J. Chem. Phys.*, 136:204105–1 – 204105–14, May 2012.

[53] C. Riplinger and F. Neese. *J. Chem. Phys.*, 138:034106–1 – 034106–18, 2013.

[54] J. Gauss and H.-J. Werner. *Phys. Chem. Chem. Phys.*, 2:2083–2090, March 2000.

[55] T. Korona, K. Pflüger, and H.-J. Werner. *Phys. Chem. Chem. Phys.*, 6:2059–2065, March 2004.

[56] N. J. Russ and T. D. Crawford. *Chem. Phys. Lett.*, 400:104–111, November 2004.

[57] D. Kats, T. Korona, and M. Schütz. *J. Chem. Phys.*, 127:064107–1 – 064107–11, 2007.

[58] N. J. Russ and T. D. Crawford. *Phys. Chem. Chem. Phys.*, 10:3345–3352, May 2008.

[59] H. R. McAlexander, T. J. Mach, and T. D. Crawford. *Phys. Chem. Chem. Phys.*, 14 (21):7830–7836, 2012.

[60] J. Friedrich, H. R. McAlexander, A. Kumar, and T. D. Crawford. *Phys. Chem. Chem. Phys.*, 2015.

[61] S. Sæbø and P. Pulay. *Chem. Phys. Lett.*, 113:13, 1985.

[62] S. Saebø and P. Pulay. *J. Chem. Phys.*, 86(2):914–922, January 1987.

[63] S. Saebø and P. Pulay. *Annu. Rev. Phys. Chem.*, 44:213–236, 1993.

[64] T. D. Crawford and H. F. Schaefer. *Reviews in Computational Chemistry*, 14:33–136, 2000.

[65] R. J. Bartlett. Analytical evaluation of gradients in coupled-cluster and many-body perturbation theory. In P. Jørgensen and J. Simons, editors, *Geometrical Derivatives of Energy Surfaces and Molecular Properties*, pages 35–61. D. Reidel, Dordrecht, 1986.

[66] A. C. Scheiner, G. E. Scuseria, J. E. Rice, T. J. Lee, and H. F. Schaefer. *J. Chem. Phys.*, 87(9):5361–5373, 1987.

[67] T. Helgaker, P. Jørgensen, and J. Olsen. *Molecular electronic-structure theory*. Wiley, Chichester, New York, 2000.

[68] E. Merzbacher. *Quantum Mechanics*. John Wiley and Sons, New York, 2nd edition, 1970.

[69] L. D. Barron. *Molecular Light Scattering and Optical Activity*. Cambridge University press, 2nd edition, 2004.

[70] M. Pecul and K. Ruud. *Adv. Quantum Chem.*, 50:185–212, 2005.

[71] J. Autschbach. *Chirality*, 21:E116–E152, December 2009.

[72] T. D. Crawford. High-accuracy quantum chemistry and chiroptical properties. In N. Berova, K. Nakanishi, R. W. Woody, and P. Polavarapu, editors, *Comprehensive Chiroptical Spectroscopy*, volume 1, pages 675–697. Wiley, 2012.

[73] R. G. Parr and W. Yang. *Density-Functional Theory of Atoms and Molecules*. Oxford University, New York, 1989.

[74] I. Shavitt and R. J. Bartlett. *Many-Body Methods in Chemistry and Physics: MBPT and Coupled-Cluster Theory*. Cambridge University Press, Cambridge, 2009.

[75] C. Diedrich, S. Kausemann, and S. Grimme. *J. Comp. Meth. Sci. Eng.*, 4:1–8, 2004.

[76] M. Srebro, N. Govind, W. A. de Jong, and J. Autschbach. *J. Phys. Chem. A*, 115(40): 10930–10949, August 2011.

[77] T. D. Crawford. *Chem. Phys. Chem.*, 12:3442–3448, 2011.

[78] J. R. Cheeseman, M. J. Frisch, F. J. Devlin, and P. J. Stephens. *Chem. Phys. Lett.*, 252:211–220, 1996.

[79] J. Autschbach, T. Ziegler, S. J. A. van Gisbergen, and E. J. Baerends. *J. Chem. Phys.*, 116(16):6930–6940, 2002.

[80] S. Grimme. Calculation of the electronic spectra of large molecules. In K. B. Lipkowitz, R. Larter, and T. R. Cundari, editors, *Reviews in Computational Chemistry*, volume 20, chapter 3, pages 153–218. VCH Publishers, New York, 2004.

[81] M. Pecul and K. Ruud. *Int. J. Quantum Chem.*, 104(5):816–829, 2005.

[82] S. Luber and M. Reiher. *Chem. Phys.*, 346:212–223, 2008.

[83] K. Ruud and A. J. Thorvaldsen. *Chirality*, 21:E54–E67, 2009.

[84] K. B. Wiberg, Y. Wang, S. M. Wilson, P. H. Vaccaro, W. L. Jorgensen, T. D. Crawford, M. L. Abrams, J. R. Cheeseman, and M. Luderer. *J. Phys. Chem. A*, 112:2415–2422, 2008.

[85] T. D. Crawford and P. J. Stephens. *J. Phys. Chem. A*, 112:1339–1345, January 2008.

[86] T. B. Pedersen, H. Koch, and C. Hättig. *J. Chem. Phys.*, 110(17):8318–8327, 1999.

[87] G. D. Lindh, T. J. Mach, and T. D. Crawford. The optimized orbital coupled cluster doubles method and optical rotation. in press, 2011.

[88] F. London. *J. Phys. Radium*, 8(10):397–409, 1937.

[89] K. Wolinski, J. F. Hinton, and P. Pulay. *J. Am. Chem. Soc.*, 112(23):8251–8260, 1990.

[90] T. Helgaker and P. Jørgensen. *J. Chem. Phys.*, 95(4):2595–2601, 1991.

[91] T. B. Pedersen. Introduction to response theory. In *Handbook of Computational Chemistry*, pages 135–156. Springer, 2012.

[92] G. D. Purvis and R. J. Bartlett. *J. Chem. Phys.*, 76:1910–1918, 1982.

[93] G. E. Scuseria and H. F. Schaefer. *Chem. Phys. Lett.*, 142(5):354–358, December 1987.

[94] C. D. Sherrill, A. I. Krylov, E. F. C. Byrd, and M. Head-Gordon. *J. Chem. Phys.*, 109 (11):4171–4182, September 1998.

[95] S. Sæbø and P. Pulay. *Ann. Rev. Phys. Chem.*, 44:213–236, 1993.

[96] M. Schütz. *Phys. Chem. Chem. Phys.*, 4(16):3941–3947, 2002.

[97] G. E. Scuseria and P. Y. Ayala. *J. Chem. Phys.*, 111(18):8330–8343, August 1999.

[98] P. E. Maslen, M. S. Lee, and M. Head-Gordon. *Chem. Phys. Lett.*, 319(3-4):205–212, 2000.

[99] N. Flocke and R. J. Bartlett. *Chem. Phys. Lett.*, 367(1-2):80–89, 2003.

[100] W. Li, P. Piecuch, J. R. Gour, and S. Li. *J. Chem. Phys.*, 131:114109, 2009.

[101] A. Hansen, D. G. Liakos, and F. Neese. *J. Chem. Phys.*, 135(214102):214102–1 – 214102–20, December 2011.

[102] T. D. Crawford and R. A. King. *Chem. Phys. Lett.*, 366:611–622, 2002.

[103] T. Korona and H.-J. Werner. *J. Chem. Phys.*, 118(7):3006–3019, February 2003.

[104] D. Kats, T. Korona, and M. Schütz. *J. Chem. Phys.*, 125:104016–1 – 104106–15, 2006.

[105] D. Kats and M. Schütz. *J. Chem. Phys.*, 131:124117–1 – 124117–11, 2009.

[106] K. Freundorfer, D. Kats, T. Korona, and M. Schütz. *J. Chem. Phys.*, 133(24):244110, 2010.

[107] L. Rosenfeld. *Z Physik*, 52:161–174, 1929.

[108] H. Koch and P. Jørgensen. *J. Chem. Phys.*, 93(5):3333–3344, 1990.

[109] T. D. Crawford, C. D. Scherrill, E. F. Valeev, J. T. Fermann, R. A. King, M. L. Leininger, S. T. Brown, C. L. Janssen, E. T. Seidl, J. P. Kenny, and W. D. Allen. *J. Comput. Chem.*, 28:1610–1616, 2007.

[110] T. B. Pedersen and H. Koch. *J. Chem. Phys.*, 108(13):5194–5204, April 1998.

[111] J. E. Rice, R. D. Amos, N. C. Handy, T. J. Lee, and H. F. Schaefer. *J. Chem. Phys.*, 85(2):963–968, 1986.

[112] L. Adamowicz, W. D. Laidig, and R. J. Bartlett. *Int. J. Quantum Chem. Symp.*, 18: 245, 1984.

[113] Y. Yamaguchi, Y. Osamura, J. D. Goddard, and H. F. Schaefer. *A New Dimension to Quantum Chemistry: Analytic Derivative Methods in* Ab Initio *Molecular Electronic Structure Theory.* Number 29 in International Series of Monographs on Chemistry. Oxford Univ. Press, New York, 1994.

[114] A. Kohn and J. Olsen. *J. Chem. Phys.*, 122:084116–1 – 084116–5, February 2005.

[115] J. W. Boughton and P. Pulay. *J. Comput. Chem.*, 14(6):736–740, June 1993.

[116] H.-J. Werner and K. Pflüger. *Ann. Rep. Comp. Chem.*, 2:53–80, 2006.

[117] J. Pipek and P. G. Mezey. *J. Chem. Phys.*, 90(9):4916–4926, January 1989.

[118] P. J. Stephens, F. J. Devlin, C. F. Chabalowski, and M. J. Frisch. *J. Phys. Chem.*, 98 (45):11623–11627, 1994.

[119] A. D. Becke. *J. Chem. Phys.*, 98(7):5648–5652, April 1993.

[120] C. Lee, W. Yang, and R. G. Parr. *Phys. Rev. B.*, 37:785–789, 1988.

[121] T. J. Mach and T. D. Crawford. *J. Phys. Chem. A*, 115:10045–10051, 2011.

[122] P. C. Hariharan and J. A. Pople. *Theor. Chem. Acc.*, 28:213–222, 1973.

[123] T. H. Dunning. *J. Chem. Phys.*, 90(2):1007, 1989.

[124] R. A. Kendall, T. H. Dunning, and R. J. Harrison. *J. Chem. Phys.*, 96(9):6796–6806, 1992.

[125] W. A. Goddard. *Science*, 227:917–923, 1985.

[126] H. F. Schaefer. *Science*, 231:1100–1107, 1986.

[127] S. Hirata. *Phys. Chem. Chem. Phys.*, 11:8397–8412, 2009.

[128] C. D. Sherrill. *J. Chem. Phys.*, 132:110902, 2010.

[129] H.-J. Werner and P. Gill. *Phys. Chem. Chem. Phys.*, 10:3318–3319, 2008.

[130] T. B. Adler and H.-J. Werner. *J. Chem. Phys.*, 130:241101–1 – 241101–5, June 2009.

[131] R. A. Mata and H. Stoll. *J. Chem. Phys.*, 134:034122–1 –0341122–8, January 2011.

[132] B. Helmich and C. Hättig. *J. Chem. Phys.*, 135:214106–1–214106–11, December 2011.

[133] B. Helmich and C. Hättig. *J. Chem. Phys.*, 139:084114–1–084114–13, August 2013.

[134] T. D. Crawford. *Reduced-Scaling Coupled-Cluster Theory for Response Properties of Large Molecules*, volume 11 of *Challenges and Advances in Computational Chemistry and Physics*, chapter 2, pages 37–55. Springer Netherlands, 2010. doi: 10.1007/978-90-481-2885-3_2.

[135] R. Ditchfield. *Mol. Phys.*, 27(4):789–807, 1974.

[136] S. F. Boys. *Rev. Mod. Phys.*, 32(2):296–299, April 1960.

[137] J. M. Turney, A. C. Simmonett, R. M. Parrish, E. G. Hohenstein, F. Evangelista, J. T. Fermann, B. J. Mintz, L. A. Burns, J. J. Wilke, M. L. Abrams, N. J. Russ, M. L. Leininger, C. L. Janssen, E. T. Seidl, W. D. Allen, H. F. Schaefer, R. A. King, E. F. Valeev, C. D. Sherrill, and T. D. Crawford. *WIRES Comput. Mol. Sci.*, 2(4):2012, 556-565 2012.

[138] O. Christiansen, H. Koch, and P. Jørgensen. *Chem. Phys. Lett.*, 243(5-6):409–418, September 1995.

[139] T. H. Dunning, Jr., K. A. Peterson, and A. K. Wilson. *J. Chem. Phys.*, 114(21): 9244–9253, June 2001.

[140] K. B. Wiber, Y.-g. Wang, S. M. Wilson, V. P. H., and J. R. Cheeseman. *J. Phys. Chem. A*, 110:13995–14002, December 2006.

[141] B. Moore, II, M. Srebro, and J. Autschbach. *J. Chem. Theory Comput.*, 8(11):4336–4346, September 2012.

[142] M. Caricato, P. H. Vaccaro, T. D. Crawford, K. B. Wiberg, and P. Lahiri. *J. Phys. Chem. A*, 118(26):4863–4871, June 2014.

[143] P. J. Stephens, D. M. McCann, J. R. Cheeseman, and M. J. Frisch. *Chirality*, 17(S1): S52–S64, 2005.

[144] D. M. McCann and P. J. Stephens. *J. Org. Chem.*, 71(16):6074–6098, June 2006.

[145] B. Mennucci, J. Tomasi, R. Cammi, J. R. Cheeseman, M. J. Frisch, F. J. Devlin, S. Gabriel, and P. J. Stephens. *J. Phys. Chem. A*, 106(25):6102–6113, May 2002.

[146] T. Müller, K. B. Wiberg, P. H. Vaccaro, J. R. Cheeseman, and M. J. Frisch. *J. Opt. Soc. Am. B*, 19(1):125–141, January 2002.

[147] S. M. Wilson, K. B. Wiberg, J. R. Cheeseman, M. J. Frisch, and P. H. Vaccaro. *J. Phys. Chem. A*, 109(51):11752–11764, November 2005.

[148] M. Pecul and K. Ruud. *Phys. Chem. Chem. Phys.*, 13:643–650, 2011.

[149] M. Feyereisen, G. Fitzgerald, and A. Komornicki. *Chem. Phys. Lett.*, 208(5,6):359–363, June 1993.

[150] J. F. Stanton and R. J. Bartlett. *J. Chem. Phys.*, 98(9):7029–7039, May 1993.

[151] E. R. Davidson. *J. Comput. Phys.*, 17:87–94, August 1975.

[152] N. Berova, P. L. Polavarapu, K. Nakanishi, and R. W. Woody. Comprehensive chiroptical spectroscopy. Wiley, 2012.

[153] F. S. Richardson and J. P. Riehl. *Chem. Rev.*, 77(6):773–792, 1977.

[154] E. Gussakovsky. *Circularly polarized luminescence (CPL) of proteins and protein complexes*, volume 2008 of *Reviews in fluorescence*, pages 425–459. Springer New York, 2008. doi: 10.1007/978-1-4419-1260-2.

[155] F. J. Coughlin, M. S. Westrol, K. D. Oyler, N. Byrne, C. Krami, E. Zysman-Colman, M. S. Lowry, and S. Bernhard. *Inorg. Chem.*, 47(6):2039–2048, 2008.

[156] F. C. Spano, Z. Zhao, and S. C. J. Meskers. *J. Chem. Phys.*, 120(22):10594–10604, June 2004.

[157] H. G. Brittain and F. S. Richardson. *J. Chem. Phys.*, 80(23):2590–2592, 1976.

[158] A. Salam. *Chem. Phys.*, 173:123–132, 1993.

[159] H. P. J. M. Dekkers, C. A. Emeis, and L. J. Oosterhoff. *J. Am. Chem. Soc.*, 91(16): 4589–4590, 1969.

[160] H. P. J. M. Dekkers and P. F. Moral. *Tetrahedron: Asymmetry*, 4(3):473–478, 1993.

[161] H. G. Brittain and N. Grinberg. *Techniques of chiroptical spectroscopy*, chapter 10, pages 271–294. Ewing's analytical instrumentation handbook. CRC Press, 3rd edition, 2005.

[162] H. Wynberg, E. W. Meijer, J. C. Hummelen, H. P. J. M. Dekkers, P. H. Schippers, and A. D. Carlson. *Nature*, 286:641–642, August 1980.

[163] E. Castiglioni, S. Abbate, and G. Longhi. *Appl. Spectrosc.*, 64(12):1416–1419, 2010.

[164] J. Schlessinger and A. Warshel. *Chem. Phys. Lett.*, 28(3):380–383, 1974.

[165] B. Pritchard and J. Autschbach. *Chem. Phys. Chem.*, 11:2409–2415, 2010.

[166] P. H. Schippers, J. P. M. van der Ploeg, and H. P. J. M. Dekkers. *J. Am. Chem. Soc.*, 105(1):84–89, 1983.

[167] C. Lee, W. Yang, and R. G. Parr. *Phys. Rev. B.*, 37:785–789, 1988.

[168] P. J. Stephens, F. J. Devlin, C. F. Chabalowski, and M. J. Frisch. *J. Phys. Chem.*, 98 (45):11623–11627, November 1994.

[169] T. Yanai, D. P. Tew, and N. C. Handy. *Chem. Phys. Lett.*, 393:51–57, June 2004.

[170] G. Longhi, E. Castiglioni, S. Abbate, F. Lebon, and D. A. Lightner. *Chirality*, 25(10): 589–599, July 2013.

[171] C. Shen, E. Anger, M. Srebro, N. Vanthuyne, K. K. Deol, T. D. Jefferson, G. Muller, J. A. G. Williams, L. Toupet, C. Roussel, J. Autschbach, R. Réau, and J. Crassous. *Chem. Sci.*, 5:1915–1927, 2014.

[172] J. F. Stanton and R. J. Bartlett. *J. Chem. Phys.*, 98(9):7029–7039, 1993.

[173] H. Koch, R. Kobayashi, A. S. de Merás, and P. Jørgensen. *J. Chem. Phys.*, 100: 4393–4400, 1994.

[174] H. Koch, H. J. Aa. Jensen, P. Jørgensen, and T. Helgaker. *J. Chem. Phys.*, 93(5): 3345–3350, 1990.

[175] F. Pawlowski, J. Olsen, and P. Jørgensen. *J. Chem. Phys.*, 142(11):114109–1–114109–51, March 2015.

[176] M. E. Casida. *Recent Advances in Density Functional Methods*, volume 1. World Scientific, Singapore, 1995.

[177] J. F. Stanton and J. Gauss. *J. Chem. Phys.*, 99(11):8840–8847, December 1993.

[178] M. J. Frisch, G. W. Trucks, H. B. Schlegel, G. E. Scuseria, M. A. Robb, J. R. Cheeseman, G. Scalmani, V. Barone, B. Mennucci, G. A. Petersson, H. Nakatsuji, M. Caricato, X. Li, H. P. Hratchian, A. F. Izmaylov, J. Bloino, G. Zheng, J. L. Sonnenberg, M. Hada, M. Ehara, K. Toyota, R. Fukuda, J. Hasegawa, M. Ishida, T. Nakajima, Y. Honda, O. Kitao, H. Nakai, T. Vreven, J. A. Montgomery, Jr., J. E. Peralta, F. Ogliaro, M. Bearpark, J. J. Heyd, E. Brothers, K. N. Kudin, V. N. Staroverov, R. Kobayashi, J. Normand, K. Raghavachari, A. Rendell, J. C. Burant, S. S. Iyengar, J. Tomasi, M. Cossi, N. Rega, J. M. Millam, M. Klene, J. E. Knox, J. B. Cross, V. Bakken, C. Adamo, J. Jaramillo, R. Gomperts, R. E. Stratmann, O. Yazyev, A. J. Austin, R. Cammi, C. Pomelli, J. W. Ochterski, R. L. Martin, K. Morokuma, V. G. Zakrzewski, G. A. Voth, P. Salvador, J. J. Dannenberg, S. Dapprich, A. D. Daniels, Ö. Farkas, J. B. Foresman, J. V. Ortiz, J. Cioslowski, and D. J. Fox. Gaussian 09 Revision A.1. Gaussian Inc. Wallingford CT 2009.

[179] N. J. Russ and T. D. Crawford. *J. Chem. Phys.*, 121(2):691–696, July 2004.

Appendix A

CPL: Supplementary Information

The supplementary information contains Cartesian coordinates (in Ångströms), adiabatic excitation energies, and velocity-gauge transition strengths and dissymmetry factors for all states of all test structures examined in this work.

A.1 Geometries

Table A.1: B3LYP/aug-cc-pVDZ geometry (Ångströms) of (1*R*)-7-methylenebicyclo[2.2.1]heptan-2-one, ground state.

Atomic Symbol	X	Y	Z
C	−0.720 318	0.424 432	1.011 669
C	−0.662 438	1.711 221	0.144 614
H	−0.044 329	2.489 937	0.610 379
C	−0.062 460	1.202 588	−1.210 887
C	0.132 380	−0.333 607	−0.974 291
C	1.297 968	−0.429 060	0.017 302
C	0.735 233	0.026 985	1.375 797
H	1.340 664	0.836 671	1.805 150
H	0.763 845	−0.825 225	2.070 098
O	2.434 806	−0.772 845	−0.216 377
H	0.255 979	−0.939 895	−1.875 038
C	−1.032 351	−0.621 809	−0.046 342
C	−2.014 930	−1.517 568	−0.132 421
H	−2.084 322	−2.209 635	−0.972 169
H	−2.786 074	−1.588 963	0.635 570
H	0.879 632	1.697 752	−1.476 721
H	−0.765 280	1.350 104	−2.039 822
H	−1.668 004	2.124 654	−0.000 901
H	−1.409 068	0.468 262	1.861 823

Table A.2: B3LYP/aug-cc-pVDZ geometry (Ångströms) of (1*R*)-7-methylenebicyclo[2.2.1]heptan-2-one, first excited state (E1 structure).

Atomic Symbol	X	Y	Z
C	−0.675 409	0.487 607	1.001 697
C	−0.340 004	1.748 971	0.159 520
H	0.385 144	2.395 826	0.669 998
C	0.220 344	1.156 032	−1.176 185
C	0.059 602	−0.375 821	−0.974 450
C	1.142 234	−0.823 403	0.096 989
C	0.660 136	−0.174 792	1.427 424
H	1.395 625	0.552 587	1.806 337
H	0.527 844	−0.959 825	2.187 111
O	2.370 308	−0.788 935	−0.257 983
H	0.085 378	−0.991 257	−1.877 985
C	−1.146 826	−0.463 333	−0.077 862
C	−2.274 100	−1.166 143	−0.218 601
H	−2.426 150	−1.832 801	−1.067 676
H	−3.084 315	−1.090 765	0.507 487
H	1.267 699	1.421 435	−1.359 541
H	−0.369 582	1.485 131	−2.043 364
H	−1.247 791	2.338 254	−0.020 848
H	−1.372 180	0.658 187	1.831 157

Table A.3: B3LYP/aug-cc-pVDZ geometry (Ångströms) of (1*R*)-7-methylenebicyclo[2.2.1]heptan-2-one, first excited state (E2 structure).

Atomic Symbol	X	Y	Z
C	0.793 708	−0.126 550	1.025 698
C	1.343 941	−1.339 391	0.227 472
H	1.074 924	−2.291 556	0.702 245
C	0.693 058	−1.175 075	−1.186 213
C	−0.160 358	0.106 789	−1.032 100
C	−1.359 729	−0.327 856	−0.060 300
C	−0.697 752	−0.370 275	1.357 550
H	−0.901 919	−1.323 450	1.865 060
H	−1.115 015	0.452 992	1.958 124
O	−2.488 546	0.233 362	−0.246 709
H	−0.515 008	0.579 996	−1.950 311
C	0.642 082	0.923 521	−0.059 985
C	1.017 815	2.206 295	−0.101 901
H	0.774 120	2.843 903	−0.951 891
H	1.584 952	2.657 682	0.713 037
H	0.083 836	−2.035 627	−1.484 097
H	1.454 305	−1.002 353	−1.961 288
H	2.438 414	−1.293 130	0.164 290
H	1.393 179	0.159 897	1.897 167

Table A.4: B3LYP/aug-cc-pVDZ geometry (Ångströms) of (1*R*)-7-methylenebicyclo[2.2.1]heptan-2-one, second excited state.

Atomic Symbol	X	Y	Z
C	−0.642 616	0.425 218	1.075 585
C	−0.421 306	1.700 024	0.193 453
H	0.341 501	2.334 919	0.657 241
C	0.024 934	1.129 534	−1.200 333
C	0.088 210	−0.411 299	−0.949 372
C	1.232 197	−0.760 226	0.051 130
C	0.743 462	−0.182 801	1.417 384
H	1.406 759	0.620 206	1.775 928
H	0.674 695	−0.941 127	2.213 423
O	2.439 677	−0.648 284	−0.357 747
H	0.067 818	−1.030 791	−1.851 244
C	−1.098 657	−0.493 944	−0.023 736
C	−2.286 102	−1.169 298	−0.210 150
H	−2.658 485	−1.392 137	−1.210 583
H	−2.855 121	−1.548 680	0.640 793
H	1.034 066	1.442 001	−1.497 475
H	−0.672 170	1.428 517	−1.998 092
H	−1.345 918	2.285 249	0.109 029
H	−1.351 293	0.564 873	1.899 187

Table A.5: B3LYP/aug-cc-pVDZ geometry (Ångströms) of (1*S*)-2-methylenebicyclo[2.2.1]heptan-7-one, ground state.

Atomic Symbol	X	Y	Z
C	−0.842 883	0.266 585	1.027 807
C	−1.083 838	1.501 824	0.123 690
H	−0.647 031	2.408 034	0.562 558
C	−0.398 151	1.111 840	−1.238 290
C	0.188 592	−0.307 425	−0.969 949
C	1.318 240	−0.161 962	0.030 677
C	0.666 575	0.199 917	1.375 621
H	1.039 354	1.151 988	1.778 714
H	0.866 209	−0.580 990	2.123 316
C	2.620 871	−0.339 326	−0.204 003
H	2.990 359	−0.622 020	−1.190 057
H	3.363 534	−0.211 445	0.585 158
H	0.405 964	−0.907 602	−1.856 737
C	−0.910 878	−0.842 570	−0.031 902
O	−1.617 409	−1.815 988	−0.120 128
H	0.389 213	1.816 276	−1.529 679
H	−1.132 962	1.065 704	−2.052 518
H	−2.157 623	1.681 535	−0.012 904
H	−1.528 914	0.153 124	1.871 266

Table A.6: B3LYP/aug-cc-pVDZ geometry (Ångströms) of (1*S*)-2-methylenebicyclo[2.2.1]heptan-7-one, first excited state (E1 structure).

Atomic Symbol	X	Y	Z
C	0.679 491	0.819 176	−0.809 581
C	1.230 980	1.217 427	0.578 934
H	0.940 284	2.242 607	0.850 018
C	0.623 134	0.148 715	1.532 571
C	−0.223 108	−0.770 728	0.624 277
C	−1.378 014	−0.089 017	−0.000 015
C	−0.840 570	1.047 302	−0.854 469
H	−1.109 964	2.034 473	−0.448 505
H	−1.243 042	0.982 221	−1.873 346
C	−2.664 287	−0.486 322	0.099 660
H	−3.471 422	0.075 746	−0.371 846
H	−2.940 248	−1.374 633	0.667 597
H	−0.412 614	−1.774 815	1.013 963
C	0.740 780	−0.751 071	−0.765 596
O	1.781 959	−1.441 635	−0.691 472
H	0.003 519	0.587 083	2.327 720
H	1.407 105	−0.449 859	2.010 560
H	2.325 936	1.166 525	0.580 389
H	1.234 328	1.230 839	−1.659 465

Table A.7: B3LYP/aug-cc-pVDZ geometry (Ångströms) of (1*S*)-2-methylenebicyclo[2.2.1]heptan-7-one, first excited state (E2 structure).

Atomic Symbol	X	Y	Z
C	0.975 483	0.219 394	0.931 330
C	1.562 992	−1.090 992	0.374 956
H	1.414 115	−1.909 856	1.093 884
C	0.785 904	−1.314 748	−0.952 432
C	−0.206 824	−0.127 018	−1.021 454
C	−1.225 552	−0.222 011	0.078 399
C	−0.481 930	−0.002 749	1.391 669
H	−0.574 709	−0.852 956	2.084 967
H	−0.870 961	0.888 487	1.902 095
C	−2.547 182	−0.376 044	−0.083 716
H	−3.227 035	−0.418 086	0.768 461
H	−2.991 431	−0.464 392	−1.075 631
H	−0.606 790	0.095 253	−2.015 276
C	0.764 091	1.021 652	−0.425 906
O	0.394 671	2.225 665	−0.445 205
H	0.232 295	−2.263 738	−0.974 159
H	1.457 227	−1.290 956	−1.818 504
H	2.639 362	−0.991 751	0.195 392
H	1.608 667	0.757 768	1.643 345

Table A.8: B3LYP/aug-cc-pVDZ geometry (Ångströms) of (1*S*)-2-methylenebicyclo[2.2.1]heptan-7-one, second excited state.

Atomic Symbol	X	Y	Z
C	0.733 371	1.037 174	−0.436 170
C	0.857 124	1.008 697	1.119 516
H	0.398 793	1.873 992	1.619 056
C	0.186 855	−0.335 705	1.511 492
C	−0.136 478	−1.003 447	0.095 980
C	−1.303 930	−0.156 083	−0.280 701
C	−0.772 119	1.160 395	−0.763 608
H	−1.313 774	2.011 244	−0.328 286
H	−0.904 899	1.192 429	−1.858 602
C	−2.629 209	−0.514 076	−0.103 602
H	−2.903 348	−1.390 347	0.481 635
H	−3.426 001	0.026 691	−0.615 086
H	−0.280 097	−2.085 375	0.133 308
C	0.998 633	−0.439 522	−0.819 076
O	2.165 856	−0.960 612	−0.750 397
H	−0.682 911	−0.218 828	2.176 104
H	0.883 461	−1.026 981	2.003 705
H	1.922 721	0.985 129	1.379 180
H	1.373 715	1.772 341	−0.930 823

Table A.9: B3LYP/aug-cc-pVDZ geometry (Ångströms) of (1*R*,4*R*)-α-fenchocampherone, ground state.

Atomic Symbol	X	Y	Z
C	−0.893 484	−0.499 491	−0.047 633
C	−0.373 263	0.342 330	1.168 980
C	−0.372 201	1.786 019	0.608 523
C	0.071 164	1.583 071	−0.877 598
C	0.217 777	0.035 109	−1.004 745
C	1.480 746	−0.288 980	−0.210 185
O	2.565 535	−0.613 615	−0.642 836
C	1.105 877	−0.092 861	1.270 867
H	1.253 106	−1.033 715	1.816 497
H	1.760 545	0.656 465	1.735 495
H	0.235 555	−0.346 572	−2.030 777
H	−0.682 056	1.949 983	−1.585 101
H	1.009 831	2.098 953	−1.114 518
H	0.320 111	2.431 541	1.163 845
H	−1.363 919	2.248 908	0.675 067
H	−0.948 119	0.215 614	2.094 880
C	−0.831 417	−2.022 460	0.162 632
H	0.172 204	−2.395 075	0.397 505
H	−1.502 539	−2.325 407	0.979 181
H	−1.162 498	−2.542 915	−0.746 873
C	−2.323 742	−0.147 117	−0.481 959
H	−2.590 740	−0.695 366	−1.396 340
H	−3.037 642	−0.445 679	0.299 680
H	−2.476 850	0.918 466	−0.679 142

Table A.10: B3LYP/aug-cc-pVDZ geometry (Ångströms) of (1*R*,4*R*)-α-fenchocampherone, first excited state.

Atomic Symbol	X	Y	Z
C	−1.004 837	−0.342 468	−0.083 734
C	−0.310 425	0.233 937	1.188 985
C	0.025 704	1.689 362	0.775 914
C	0.408 485	1.550 943	−0.732 243
C	0.199 408	0.037 103	−1.004 078
C	1.351 831	−0.709 942	−0.267 177
O	2.558 744	−0.566 947	−0.687 466
C	1.024 421	−0.536 877	1.248 094
H	0.951 821	−1.522 693	1.730 506
H	1.821 575	0.026 040	1.756 027
H	0.129 059	−0.241 049	−2.062 138
H	−0.238 167	2.158 610	−1.380 915
H	1.443 562	1.845 393	−0.937 900
H	0.848 687	2.094 202	1.378 481
H	−0.833 537	2.355 455	0.918 174
H	−0.897 623	0.151 580	2.114 420
C	−1.308 863	−1.846 935	−0.021 739
H	−0.421 999	−2.454 654	0.182 580
H	−2.061 348	−2.051 161	0.753 767
H	−1.724 564	−2.188 004	−0.980 529
C	−2.306 476	0.378 833	−0.477 243
H	−2.665 599	0.009 778	−1.448 038
H	−3.088 702	0.162 398	0.264 529
H	−2.208 606	1.465 939	−0.549 910

Table A.11: B3LYP/aug-cc-pVDZ geometry (Ångströms) of (1*R*,4*R*)-α-fenchocampherone, second excited state.

Atomic Symbol	X	Y	Z
C	−0.918 750	−0.470 270	−0.025 561
C	−0.349 171	0.364 574	1.167 856
C	−0.275 576	1.804 370	0.615 220
C	0.195 942	1.581 245	−0.847 541
C	0.180 152	0.036 958	−1.018 869
C	1.454 967	−0.372 797	−0.192 944
O	2.489 446	−0.699 004	−0.686 112
C	1.095 425	−0.144 488	1.288 950
H	1.212 222	−1.112 739	1.793 242
H	1.820 912	0.565 159	1.715 370
H	0.203 878	−0.349 611	−2.042 599
H	−0.509 337	1.980 412	−1.590 715
H	1.173 277	2.027 356	−1.076 625
H	0.422 173	2.426 969	1.190 343
H	−1.257 698	2.295 914	0.651 550
H	−0.902 707	0.253 331	2.109 027
C	−0.929 206	−1.992 997	0.180 774
H	0.049 927	−2.428 767	0.431 180
H	−1.620 873	−2.251 852	0.994 803
H	−1.282 510	−2.492 752	−0.733 283
C	−2.316 369	−0.046 322	−0.512 457
H	−2.568 523	−0.570 910	−1.445 663
H	−3.054 631	−0.342 781	0.246 317
H	−2.426 159	1.030 654	−0.686 613

Table A.12: B3LYP/aug-cc-pVDZ geometry (Ångströms) of (1*R*,4*R*)-α-fenchocampherone, third excited state.

Atomic Symbol	X	Y	Z
C	−0.898 254	−0.490 688	−0.013 399
C	−0.353 588	0.381 179	1.165 756
C	−0.323 325	1.816 641	0.593 433
C	0.143 591	1.589 144	−0.872 440
C	0.178 339	0.043 684	−1.021 609
C	1.461 687	−0.325 601	−0.197 044
O	2.473 259	−0.722 004	−0.681 492
C	1.110 294	−0.073 961	1.285 671
H	1.269 593	−1.024 348	1.806 838
H	1.811 664	0.675 463	1.677 519
H	0.212 931	−0.358 198	−2.036 348
H	−0.566 341	1.965 936	−1.619 215
H	1.107 368	2.075 527	−1.098 937
H	0.373 419	2.472 333	1.140 907
H	−1.307 560	2.291 947	0.637 270
H	−0.895 123	0.265 191	2.110 194
C	−0.863 376	−2.011 086	0.213 231
H	0.122 322	−2.419 138	0.476 410
H	−1.557 676	−2.287 130	1.021 928
H	−1.195 289	−2.540 769	−0.693 811
C	−2.309 989	−0.123 923	−0.504 368
H	−2.540 099	−0.665 257	−1.432 966
H	−3.038 681	−0.453 283	0.247 028
H	−2.454 869	0.945 427	−0.680 273

Table A.13: B3LYP/aug-cc-pVDZ geometry (Ångströms) of (1*R*,5*S*)-*cis*-β-hydrindanone, ground state.

Atomic Symbol	X	Y	Z
C	0.472 171 293 965	0.630 966 601 046	−0.785 450 654 345
C	0.472 171 293 965	0.630 966 601 046	0.773 242 815 655
C	0.472 171 293 965	−0.864 812 185 381	1.146 466 666 141
C	1.203 566 937 855	−1.557 333 202 628	−0.005 822 031 754
C	1.401 219 377 825	−0.544 285 940 684	−1.137 302 160 283
H	2.460 311 995 415	−0.239 601 630 805	−1.115 291 997 173
H	1.217 490 110 093	−1.008 175 585 659	−2.114 940 421 395
O	1.569 905 606 719	−2.713 152 018 727	−0.020 084 503 982
H	−0.544 384 235 154	−1.284 431 726 158	1.196 665 342 860
H	0.957 399 570 671	−1.093 645 571 090	2.103 669 670 035
C	−0.638 681 209 164	1.492 912 733 670	1.393 387 128 128
C	−2.018 923 855 633	1.254 480 929 759	0.764 059 950 722
C	−1.962 446 015 971	1.405 707 628 330	−0.761 718 584 058
C	−0.940 396 144 560	0.435 855 798 124	−1.367 689 476 959
H	−1.278 156 856 040	−0.597 921 162 055	−1.185 260 327 102
H	−0.896 667 776 415	0.551 893 587 852	−2.460 995 144 520
H	−2.954 881 946 194	1.228 307 378 028	−1.200 796 282 744
H	−1.684 390 094 658	2.442 078 568 895	−1.016 794 391 660
H	−2.744 643 327 024	1.960 476 977 173	1.193 185 995 903
H	−2.384 593 725 901	0.245 575 517 475	1.014 974 450 475
H	−0.371 410 203 044	2.553 179 313 140	1.254 294 535 682
H	−0.677 481 784 259	1.324 735 870 483	2.480 314 891 083
H	1.440 291 690 694	1.045 918 000 959	1.097 358 894 088
H	0.871 935 329 197	1.586 543 163 920	−1.155 926 966 844

Table A.14: B3LYP/aug-cc-pVDZ geometry (Ångströms) of (1*R*,5*S*)-*cis*-β-hydrindanone, first excited state.

Atomic Symbol	X	Y	Z
C	0.471 273 805 711	0.616 314 269 054	−0.789 119 436 781
C	0.471 273 805 711	0.616 314 269 054	0.759 370 763 219
C	0.471 273 805 711	−0.880 365 502 858	1.174 431 746 244
C	1.014 700 735 602	−1.589 444 940 472	−0.065 502 329 316
C	1.385 062 013 073	−0.576 328 264 059	−1.142 897 974 365
H	2.458 013 130 581	−0.303 980 359 576	−1.062 667 620 523
H	1.225 234 681 277	−0.975 770 015 082	−2.155 026 495 192
O	1.684 510 260 181	−2.692 284 291 881	0.061 853 918 575
H	−0.530 054 329 816	−1.264 519 187 435	1.429 650 164 916
H	1.111 146 588 663	−1.062 145 614 671	2.055 562 875 361
C	−0.641 034 898 582	1.469 818 108 174	1.395 410 722 492
C	−2.015 399 345 058	1.262 294 678 192	0.744 302 069 148
C	−1.938 754 394 340	1.453 901 609 864	−0.775 786 353 720
C	−0.935 556 276 539	0.472 791 280 855	−1.395 613 441 708
H	−1.293 729 491 908	−0.556 470 245 285	−1.237 211 620 506
H	−0.875 419 072 491	0.618 623 239 848	−2.484 706 093 203
H	−2.930 076 507 235	1.311 683 113 452	−1.229 830 246 562
H	−1.634 463 070 425	2.490 408 310 487	−0.999 305 514 091
H	−2.738 732 376 226	1.964 032 079 019	1.184 675 085 721
H	−2.391 674 515 725	0.249 785 853 038	0.962 033 107 520
H	−0.359 728 049 086	2.530 593 596 957	1.292 223 073 544
H	−0.690 515 140 162	1.268 994 606 138	2.476 250 937 674
H	1.439 716 958 406	1.027 809 265 391	1.081 961 370 132
H	0.921 819 803 377	1.551 014 646 528	−1.159 313 719 539

Table A.15: B3LYP/aug-cc-pVDZ geometry (Ångströms) of (1*R*,5*S*)-*cis*-β-hydrindanone, second excited state.

Atomic Symbol	X	Y	Z
C	0.465 292 808 187	0.612 790 865 190	−0.767 972 937 703
C	0.465 292 808 187	0.612 790 865 190	0.769 163 792 297
C	0.465 292 808 187	−0.877 412 401 633	1.174 189 741 356
C	1.215 297 048 508	−1.541 932 843 818	0.005 048 590 203
C	1.425 720 545 588	−0.533 106 235 788	−1.135 978 147 189
H	2.485 664 266 290	−0.244 062 494 549	−1.011 301 017 049
H	1.299 994 510 647	−1.011 470 188 645	−2.116 125 418 638
O	1.536 366 068 866	−2.695 733 817 873	−0.028 523 751 351
H	−0.529 985 912 780	−1.350 311 985 684	1.171 483 104 382
H	0.967 932 515 725	−1.116 366 999 489	2.122 415 614 584
C	−0.663 020 579 864	1.429 478 949 005	1.417 630 757 385
C	−2.028 620 870 799	1.261 708 183 731	0.741 463 239 981
C	−1.931 667 342 148	1.441 737 137 625	−0.778 025 747 752
C	−0.927 547 280 354	0.460 902 195 997	−1.397 468 320 715
H	−1.300 561 458 437	−0.568 676 881 836	−1.272 430 540 817
H	−0.843 077 880 508	0.625 693 961 177	−2.486 281 355 492
H	−2.917 372 014 924	1.299 298 631 052	−1.244 711 432 945
H	−1.621 076 967 729	2.473 680 229 419	−1.006 211 541 554
H	−2.722 926 107 879	2.007 209 972 915	1.165 395 099 675
H	−2.462 302 843 919	0.275 327 502 570	0.970 470 882 338
H	−0.356 042 121 294	2.486 752 681 928	1.356 703 691 413
H	−0.720 844 518 069	1.197 361 681 957	2.493 222 461 001
H	1.438 266 062 415	1.024 383 843 131	1.109 460 558 103
H	0.925 551 047 179	1.548 069 526 495	−1.133 395 540 629

Table A.16: B3LYP/aug-cc-pVDZ geometry (Ångströms) of (1*R*,5*S*)-*cis*-β-hydrindanone, third excited state.

Atomic Symbol	X	Y	Z
C	0.406 712 210 766	0.624 426 746 670	−0.794 927 903 334
C	0.406 712 210 766	0.624 426 746 670	0.751 187 956 666
C	0.406 712 210 766	−0.867 225 081 135	1.124 488 293 422
C	1.311 103 726 706	−1.466 919 660 343	0.033 168 970 682
C	1.392 929 728 397	−0.497 026 263 222	−1.169 961 804 109
H	2.444 268 362 624	−0.174 791 774 939	−1.190 301 431 542
H	1.175 826 986 374	−1.056 514 444 903	−2.087 329 906 283
O	1.946 078 791 742	−2.475 766 893 181	0.144 963 642 847
H	−0.561 588 596 647	−1.379 174 759 529	0.942 429 827 259
H	0.759 115 178 693	−1.141 644 751 226	2.123 623 244 636
C	−0.762 742 085 591	1.401 603 587 394	1.386 829 676 492
C	−2.107 685 847 850	1.119 795 404 876	0.715 202 457 100
C	−2.026 586 776 491	1.322 893 340 457	−0.799 407 465 769
C	−0.978 903 464 894	0.385 440 511 357	−1.401 919 643 815
H	−1.308 675 961 370	−0.666 225 001 124	−1.234 451 432 896
H	−0.919 625 082 118	0.507 252 948 882	−2.493 284 916 517
H	−3.003 165 851 000	1.108 856 107 636	−1.258 270 344 331
H	−1.776 701 428 285	2.374 022 467 387	−1.030 247 194 138
H	−2.868 116 169 197	1.781 847 068 040	1.152 606 916 284
H	−2.452 405 979 085	0.084 066 785 580	0.918 661 031 028
H	−0.508 198 176 328	2.471 939 869 769	1.291 411 275 420
H	−0.806 475 224 738	1.190 393 728 059	2.465 316 005 780
H	1.354 571 148 142	1.082 199 877 141	1.094 367 208 690
H	0.824 618 244 103	1.587 668 272 439	−1.145 608 123 115

Table A.17: B3LYP/aug-cc-pVDZ geometry (Ångströms) of (*S*)-3-methylcyclopentanone, ground state.

Atomic Symbol	X	Y	Z
C	0.000 000 00	0.000 000 00	0.000 000 00
C	0.516 082 00	1.356 344 00	0.540 220 00
C	2.034 648 00	1.315 857 00	0.306 456 00
C	2.401 849 00	−0.169 031 00	0.387 854 00
O	3.527 554 00	−0.616 975 00	0.429 311 00
C	1.110 111 00	−0.987 092 00	0.405 661 00
H	1.198 902 00	−1.880 546 00	−0.224 565 00
H	0.959 293 00	−1.333 568 00	1.442 964 00
H	2.636 581 00	1.902 992 00	1.010 847 00
H	2.296 642 00	1.659 867 00	−0.707 250 00
H	0.301 645 00	1.422 109 00	1.618 632 00
H	0.023 250 00	2.209 632 00	0.056 563 00
C	−1.399 868 00	−0.374 869 00	0.481 189 00
H	−1.425 998 00	−0.456 345 00	1.578 491 00
H	−2.137 788 00	0.383 575 00	0.182 159 00
H	−1.723 048 00	−1.339 250 00	0.064 447 00
H	−0.013 483 00	0.061 272 00	−1.101 315 00

Table A.18: EOM-CCSD/aug-cc-pVDZ geometry (Ångströms) of (*S*)-3-methylcyclopentanone, ground state.

Atomic Symbol	X	Y	Z
C	−1.164 025 595 261	−0.062 697 218 307	−0.372 038 144 698
C	−0.651 133 232 836	1.285 899 904 555	0.192 706 656 919
C	0.866 791 670 659	1.254 246 226 700	−0.075 384 266 904
C	1.234 291 222 435	−0.235 243 000 352	0.015 496 366 709
O	2.364 153 733 515	−0.685 335 086 485	0.049 361 304 980
C	−0.061 834 277 860	−1.054 854 502 171	0.052 992 311 611
H	0.020 590 633 565	−1.961 360 862 458	−0.564 916 305 754
H	−0.219 643 952 293	−1.372 131 719 303	1.102 007 941 233
H	1.481 814 756 538	1.850 826 082 049	0.614 401 721 624
H	1.096 401 563 682	1.585 435 347 797	−1.104 463 653 189
H	−0.842 697 918 970	1.314 846 175 357	1.281 581 385 001
H	−1.159 146 330 118	2.152 199 410 423	−0.259 870 891 013
C	−2.570 817 106 849	−0.439 437 819 820	0.098 413 673 067
H	−2.598 922 845 178	−0.520 888 166 158	1.199 593 776 315
H	−3.308 278 122 245	0.322 820 454 584	−0.206 182 209 735
H	−2.889 687 266 168	−1.407 720 664 761	−0.322 884 271 457
H	−1.159 185 730 626	0.007 460 106 877	−1.477 088 074 498

Table A.19: B3LYP/aug-cc-pVDZ geometry (Ångströms) of (*S*)-3-methylcyclopentanone, first excited state.

Atomic Symbol	X	Y	Z
C	0.000 000 00	0.000 000 00	0.000 000 00
C	−0.516 740 00	1.353 041 00	−0.522 354 00
C	−2.037 928 00	1.302 617 00	−0.300 788 00
C	−2.344 416 00	−0.157 152 00	−0.609 327 00
O	−3.524 557 00	−0.647 020 00	−0.391 911 00
C	−1.109 081 00	−1.025 014 00	−0.366 841 00
H	−1.284 554 00	−1.760 169 00	0.438 373 00
H	−0.866 976 00	−1.603 418 00	−1.274 642 00
H	−2.611 270 00	1.988 039 00	−0.940 006 00
H	−2.302 023 00	1.535 188 00	0.752 187 00
H	−0.296 695 00	1.456 661 00	−1.594 794 00
H	−0.058 086 00	2.203 894 00	0.000 960 00
C	1.386 385 00	−0.393 929 00	−0.511 614 00
H	1.391 516 00	−0.465 830 00	−1.609 437 00
H	2.140 059 00	0.350 409 00	−0.216 777 00
H	1.700 715 00	−1.366 173 00	−0.106 699 00
H	0.035 981 00	0.059 332 00	1.099 222 00

Table A.20: EOM-CCSD/aug-cc-pVDZ geometry (Ångströms) of (*S*)-3-methylcyclopentanone, first excited state.

Atomic Symbol	X	Y	Z
C	−1.153 300 912 459	−0.055 474 162 939	−0.377 661 730 854
C	−0.647 695 023 084	1.299 536 827 963	0.160 490 896 685
C	0.874 646 309 256	1.255 780 368 133	−0.082 607 168 909
C	1.191 492 795 459	−0.206 287 625 449	0.252 630 140 447
O	2.366 938 784 960	−0.703 322 618 235	−0.057 983 640 859
C	−0.061 539 117 777	−1.076 732 665 987	0.048 024 845 700
H	0.115 897 027 859	−1.853 873 629 255	−0.717 493 130 401
H	−0.322 954 453 187	−1.590 796 107 324	0.990 582 528 406
H	1.454 338 188 540	1.958 567 686 186	0.535 843 459 311
H	1.117 040 634 498	1.450 933 321 285	−1.148 436 258 990
H	−0.852 641 093 600	1.374 140 539 206	1.243 067 874 732
H	−1.126 005 829 818	2.156 756 019 624	−0.341 125 591 591
C	−2.559 098 446 104	−0.437 951 960 774	0.097 577 516 701
H	−2.591 559 369 645	−0.487 550 378 040	1.200 178 881 593
H	−3.305 118 207 594	0.303 904 004 910	−0.234 747 541 057
H	−2.860 747 617 298	−1.422 532 723 309	−0.297 989 471 219
H	−1.146 817 219 030	−0.001 189 348 718	−1.481 919 154 568

Table A.21: B3LYP/aug-cc-pVDZ geometry (Ångströms) of (*S*)-3-methylcyclopentanone, second excited state.

Atomic Symbol	X	Y	Z
C	0.000 000 00	0.000 000 00	0.000 000 00
C	0.533 458 00	1.338 356 00	0.531 243 00
C	2.053 608 00	1.292 202 00	0.315 057 00
C	2.375 786 00	−0.207 824 00	0.368 968 00
O	3.474 751 00	−0.680 165 00	0.431 676 00
C	1.079 889 00	−1.032 931 00	0.390 162 00
H	1.170 375 00	−1.922 162 00	−0.252 559 00
H	1.002 312 00	−1.350 868 00	1.446 492 00
H	2.684 627 00	1.839 251 00	1.031 519 00
H	2.345 412 00	1.575 992 00	−0.713 378 00
H	0.299 930 00	1.468 856 00	1.594 953 00
H	0.115 494 00	2.194 427 00	−0.027 015 00
C	−1.390 185 00	−0.405 921 00	0.490 230 00
H	−1.431 384 00	−0.465 165 00	1.586 935 00
H	−2.125 525 00	0.338 594 00	0.149 589 00
H	−1.685 754 00	−1.379 802 00	0.071 692 00
H	−0.013 403 00	0.051 711 00	−1.100 464 00

Table A.22: EOM-CCSD/aug-cc-pVDZ geometry (Ångströms) of (*S*)-3-methylcyclopentanone, second excited state.

Atomic Symbol	X	Y	Z
C	−1.160 876 712 767	−0.040 434 171 232	−0.381 027 898 256
C	−0.645 574 146 161	1.294 095 791 613	0.187 125 272 101
C	0.876 053 910 364	1.285 135 204 783	−0.050 623 636 800
C	1.233 220 334 648	−0.235 037 438 987	0.004 603 457 347
O	2.333 154 219 211	−0.695 300 120 494	0.058 014 435 166
C	−0.085 513 767 594	−1.074 622 269 431	0.021 850 641 161
H	0.035 858 493 346	−1.957 935 732 995	−0.628 011 494 041
H	−0.148 724 886 184	−1.374 781 872 029	1.088 741 370 425
H	1.513 351 341 012	1.820 350 817 135	0.672 186 940 025
H	1.158 489 288 694	1.548 128 849 155	−1.091 502 001 327
H	−0.864 522 896 620	1.373 209 170 693	1.262 763 331 775
H	−1.085 005 035 095	2.163 416 076 172	−0.333 977 714 064
C	−2.549 070 084 785	−0.462 483 386 885	0.122 335 682 214
H	−2.568 678 572 389	−0.522 829 722 661	1.222 964 682 876
H	−3.299 526 756 787	0.277 152 421 077	−0.203 408 438 049
H	−2.838 496 863 792	−1.442 871 843 748	−0.289 619 841 878
H	−1.167 722 295 781	0.022 664 695 142	−1.480 950 129 139

Table A.23: B3LYP/aug-cc-pVDZ geometry (Ångströms) of (1*R*,4*R*)-norbornenone, ground state.

Atomic Symbol	X	Y	Z
C	0.581 186 635 214	0.885 953 859 622	−0.316 674 314 066
C	0.581 186 635 214	0.885 953 859 622	1.213 742 985 934
C	0.581 186 635 214	−0.393 936 234 880	1.622 848 061 561
C	0.560 809 848 835	−1.280 525 055 239	0.377 132 419 217
C	−0.858 100 824 943	−1.111 601 329 598	−0.245 514 049 283
C	−0.839 562 180 042	0.374 593 113 818	−0.656 025 991 594
O	−1.745 808 940 792	1.007 077 673 541	−1.148 610 002 441
H	−1.685 190 500 752	−1.327 221 805 244	0.440 285 316 081
H	−0.994 791 130 713	−1.723 002 183 540	−1.149 482 124 446
H	0.886 127 741 122	−2.317 313 798 170	0.510 108 915 473
C	1.398 838 767 119	−0.403 014 164 098	−0.592 973 253 532
H	1.346 329 441 326	−0.742 214 413 205	−1.637 613 657 580
H	2.446 514 935 613	−0.302 216 595 047	−0.284 694 491 347
H	0.496 569 586 437	−0.754 127 956 810	2.646 724 186 588
H	0.481 431 287 538	1.779 902 343 201	1.825 703 600 576
H	0.850 576 548 505	1.816 914 146 814	−0.821 511 667 621

Table A.24: CAM-B3LYP/aug-cc-pVDZ geometry (Ångströms) of (1*R*,4*R*)-norbornenone, ground state.

Atomic Symbol	X	Y	Z
C	0.000 000 00	0.000 000 00	0.000 000 00
C	1.525 470 98	0.000 000 00	0.000 000 00
C	1.932 080 38	−1.273 771 95	0.000 000 00
C	0.690 406 32	−2.156 821 84	0.018 884 53
C	0.071 166 53	−1.989 007 46	1.431 023 80
C	−0.338 041 87	−0.510 829 68	1.410 764 68
O	−0.831 652 99	0.117 174 40	2.313 514 54
H	0.756 687 65	−2.200 582 61	2.257 754 79
H	−0.831 341 51	−2.599 573 29	1.568 141 64
H	0.823 190 84	−3.192 280 14	−0.306 939 01
C	−0.274 276 81	−1.282 566 62	−0.814 556 74
H	−1.317 766 36	−1.621 398 65	−0.761 366 59
H	0.033 972 25	−1.181 696 76	−1.860 797 66
H	2.955 545 42	−1.633 030 21	0.082 846 09
H	2.138 858 83	0.892 452 03	0.094 928 01
H	−0.505 512 99	0.929 927 61	−0.267 655 70

Table A.25: EOM-CCSD/aug-cc-pVDZ geometry (Ångströms) of (1R,4R)-norbornenone, ground state.

Atomic Symbol	X	Y	Z
C	−0.077 326 143 898	−0.891 255 663 788	0.656 071 190 228
C	0.841 279 390 362	−1.283 626 231 018	−0.511 015 462 735
C	1.530 625 736 219	−0.177 376 109 057	−0.877 764 862 744
C	1.074 312 339 257	0.975 026 967 322	0.026 729 663 825
C	−0.383 153 455 732	1.313 033 033 709	−0.414 513 081 704
C	−1.128 081 516 315	0.013 692 197 866	−0.028 901 026 786
O	−2.301 327 274 609	−0.236 541 245 310	−0.220 267 409 470
H	−0.494 099 836 941	1.532 741 366 931	−1.486 079 482 421
H	−0.812 839 508 650	2.147 997 478 179	0.164 605 711 090
H	1.750 885 800 880	1.836 961 079 214	0.098 622 993 061
C	0.796 161 061 994	0.193 857 276 587	1.343 665 393 513
H	0.243 982 499 997	0.792 001 341 505	2.089 362 243 095
H	1.707 632 292 054	−0.228 736 415 927	1.792 993 358 638
H	2.205 253 341 906	−0.076 540 707 725	−1.730 300 766 717
H	0.830 575 408 356	−2.256 615 398 469	−1.004 734 315 486
H	−0.506 205 398 629	−1.700 588 941 040	1.258 172 688 578

Table A.26: B3LYP/aug-cc-pVDZ geometry (Ångströms) of (1*R*,4*R*)-norbornenone, first excited state.

Atomic Symbol	X	Y	Z
C	0.626 714 038 347	0.875 607 658 200	−0.372 809 768 102
C	0.626 714 038 347	0.875 607 658 200	1.123 280 841 898
C	0.626 714 038 347	−0.418 046 730 368	1.538 994 154 358
C	0.585 816 774 292	−1.282 060 503 963	0.304 283 795 379
C	−0.872 762 023 102	−1.125 087 596 119	−0.285 025 314 250
C	−0.850 338 569 856	0.336 153 242 252	−0.811 185 895 646
O	−1.844 442 071 140	1.107 800 782 588	−0.670 057 264 518
H	−1.659 055 485 801	−1.237 730 123 606	0.476 732 180 627
H	−1.060 767 621 323	−1.841 340 396 892	−1.096 316 887 873
H	0.875 243 193 871	−2.332 259 055 566	0.430 159 332 577
C	1.396 653 364 249	−0.426 751 434 847	−0.693 773 109 447
H	1.296 860 741 775	−0.740 007 157 810	−1.739 016 945 404
H	2.455 354 462 742	−0.346 309 139 608	−0.415 829 835 433
H	0.521 267 183 945	−0.778 891 509 292	2.560 218 301 011
H	0.497 547 324 621	1.759 304 459 384	1.745 400 861 174
H	0.871 385 537 986	1.802 057 834 361	−0.897 340 604 998

Table A.27: CAM-B3LYP/aug-cc-pVDZ geometry (Ångströms) of (1*R*,4*R*)-norbornenone, first excited state.

Atomic Symbol	X	Y	Z
C	0.000 000 00	0.000 000 00	0.000 000 00
C	1.501 717 99	0.000 000 00	0.000 000 00
C	1.909 030 73	−1.282 243 72	0.000 000 00
C	0.673 226 43	−2.147 201 81	0.039 027 21
C	0.086 460 33	−1.990 585 29	1.482 063 52
C	−0.421 189 53	−0.526 675 33	1.456 684 98
O	−0.257 969 61	0.236 297 51	2.451 188 39
H	0.842 560 53	−2.112 811 81	2.269 227 18
H	−0.739 696 76	−2.687 014 27	1.672 098 23
H	0.799 018 32	−3.193 944 52	−0.257 381 15
C	−0.312 431 30	−1.291 508 34	−0.773 918 19
H	−1.357 367 11	−1.606 777 40	−0.683 115 69
H	−0.026 754 37	−1.206 444 07	−1.828 542 17
H	2.929 350 78	−1.645 831 30	0.097 655 32
H	2.122 866 32	0.884 400 64	0.120 319 89
H	−0.521 063 05	0.924 477 65	−0.255 903 51

Table A.28: EOM-CCSD/aug-cc-pVDZ geometry (Ångströms) of (1*R*,4*R*)-norbornenone, first excited state.

Atomic Symbol	X	Y	Z
C	−0.077 985 478 396	−0.869 067 921 654	0.731 728 717 425
C	0.770 344 690 405	−1.263 125 338 247	−0.471 425 073 196
C	1.465 360 541 193	−0.162 039 978 092	−0.855 826 574 897
C	1.058 003 241 720	0.980 008 179 618	0.068 877 927 355
C	−0.413 522 305 836	1.356 384 813 681	−0.336 234 593 601
C	−1.190 347 872 425	0.097 910 410 022	0.149 090 459 800
O	−2.121 988 574 360	−0.402 688 951 555	−0.599 873 682 950
H	−0.536 293 091 464	1.489 644 365 979	−1.424 194 609 920
H	−0.775 652 538 906	2.258 753 957 334	0.182 586 087 193
H	1.735 260 311 472	1.845 253 224 559	0.106 629 340 358
C	0.816 537 099 856	0.210 202 365 889	1.391 805 570 278
H	0.287 768 211 294	0.799 381 220 857	2.157 345 649 036
H	1.740 249 045 022	−0.225 034 473 001	1.803 290 933 762
H	2.094 134 511 756	−0.055 836 392 726	−1.741 861 362 136
H	0.709 297 164 850	−2.220 847 310 894	−0.991 157 646 160
H	−0.491 687 762 941	−1.670 983 728 559	1.354 766 759 484

Table A.29: B3LYP/aug-cc-pVDZ geometry (Ångströms) of (1*R*,4*R*)-norbornenone, second excited state.

Atomic Symbol	X	Y	Z
C	0.000 000 00	0.000 000 00	0.000 000 00
C	1.477 724 17	0.000 000 00	0.000 000 00
C	1.801 672 18	−1.408 744 96	0.000 000 00
C	0.554 885 60	−2.193 844 28	−0.271 809 39
C	−0.237 902 62	−2.356 509 67	1.074 030 49
C	−0.464 602 42	−0.853 881 74	1.358 324 41
O	−0.993 514 08	−0.366 370 10	2.310 732 70
H	0.338 919 52	−2.792 471 61	1.895 791 72
H	−1.218 348 01	−2.882 801 24	0.987 882 60
H	0.688 866 80	−3.169 899 49	−0.760 138 02
C	−0.354 684 82	−1.157 840 94	−0.978 629 38
H	−1.417 336 54	−1.434 546 04	−0.997 204 11
H	−0.004 822 05	−0.888 198 65	−1.981 555 40
H	2.791 125 91	−1.852 094 25	0.076 738 32
H	2.068 304 01	0.793 899 11	0.447 879 40
H	−0.557 026 63	0.940 262 92	−0.023 746 35

Table A.30: CAM-B3LYP/aug-cc-pVDZ geometry (Ångströms) of (1*R*,4*R*)-norbornenone, second excited state.

Atomic Symbol	X	Y	Z
C	0.000 000 00	0.000 000 00	0.000 000 00
C	1.442 497 35	0.000 000 00	0.000 000 00
C	1.792 436 04	−1.405 044 93	0.000 000 00
C	0.551 272 88	−2.204 690 64	−0.215 653 11
C	−0.183 920 52	−2.359 476 19	1.144 794 12
C	−0.428 251 42	−0.870 917 02	1.450 685 65
O	−0.881 352 29	−0.357 113 67	2.408 974 76
H	0.425 313 68	−2.774 390 30	1.954 536 57
H	−1.153 564 97	−2.899 217 02	1.083 035 68
H	0.696 132 89	−3.177 405 83	−0.703 498 74
C	−0.387 942 94	−1.191 544 07	−0.909 036 39
H	−1.449 078 73	−1.463 187 03	−0.864 141 20
H	−0.087 742 41	−0.970 107 89	−1.938 480 54
H	2.793 983 31	−1.825 055 48	0.023 942 60
H	2.062 106 90	0.820 985 58	0.344 147 34
H	−0.571 824 50	0.929 424 36	0.002 741 73

Table A.31: EOM-CCSD/aug-cc-pVDZ geometry (Ångströms) of (1R,4R)-norbornenone, second excited state.

Atomic Symbol	X	Y	Z
C	−0.192 864 345 164	1.080 442 927 670	−0.568 866 032 020
C	1.249 185 782 038	1.037 101 676 704	−0.431 100 864 190
C	1.591 654 203 039	−0.350 617 027 205	−0.450 465 210 242
C	0.349 120 538 375	−1.151 391 234 719	−0.756 639 692 793
C	−0.441 564 282 198	−1.337 667 954 759	0.575 430 840 113
C	−0.671 853 410 137	0.151 501 747 922	0.935 352 550 154
O	−1.064 116 698 941	0.695 167 923 100	1.907 359 119 600
H	0.134 930 926 861	−1.789 449 667 427	1.398 459 285 858
H	−1.434 620 614 761	−1.836 922 949 599	0.452 311 216 593
H	0.510 373 794 103	−2.114 922 918 850	−1.265 973 715 729
C	−0.555 108 931 687	−0.111 503 071 944	−1.479 432 348 821
H	−1.625 528 380 535	−0.370 474 836 407	−1.477 541 969 403
H	−0.208 022 265 212	0.105 947 963 907	−2.502 495 917 890
H	2.586 539 156 056	−0.781 314 673 887	−0.334 178 146 807
H	1.866 698 078 829	1.859 985 146 129	−0.072 619 984 127
H	−0.761 116 549 702	2.016 372 538 002	−0.563 199 806 274

Table A.32: B3LYP/aug-cc-pVDZ geometry (Ångströms) of (1*R*,4*R*)-norbornenone, third excited state.

Atomic Symbol	X	Y	Z
C	0.000 000 00	0.000 000 00	0.000 000 00
C	1.479 271 18	0.000 000 00	0.000 000 00
C	1.886 594 90	−1.325 370 62	0.000 000 00
C	0.665 806 58	−2.178 116 89	0.144 788 75
C	0.119 998 18	−1.952 668 43	1.607 575 81
C	−0.381 860 93	−0.506 296 81	1.505 215 29
O	−0.964 150 39	0.148 358 81	2.309 489 30
H	0.883 071 40	−2.010 276 59	2.399 798 18
H	−0.708 899 02	−2.616 030 14	1.876 957 45
H	0.795 399 58	−3.240 926 42	−0.101 583 23
C	−0.360 342 56	−1.364 617 81	−0.670 553 11
H	−1.406 682 27	−1.668 150 17	−0.510 065 88
H	−0.135 189 81	−1.338 439 56	−1.746 046 12
H	2.911 775 84	−1.701 814 36	−0.053 925 60
H	2.103 440 04	0.889 491 05	0.076 498 31
H	−0.551 067 19	0.916 837 10	−0.238 218 68

Table A.33: CAM-B3LYP/aug-cc-pVDZ geometry (Ångströms) of (1*R*,4*R*)-norbornenone, third excited state.

Atomic Symbol	X	Y	Z
C	0.000 000 00	0.000 000 00	0.000 000 00
C	1.463 029 78	0.000 000 00	0.000 000 00
C	1.876 048 96	−1.321 757 29	0.000 000 00
C	0.663 270 81	−2.172 672 59	0.150 216 18
C	0.138 593 13	−1.943 445 64	1.607 687 68
C	−0.355 858 95	−0.500 318 65	1.518 693 68
O	−0.906 098 91	0.166 184 44	2.321 874 43
H	0.904 722 78	−1.999 953 65	2.394 805 14
H	−0.688 215 27	−2.606 905 44	1.877 418 25
H	0.794 506 02	−3.232 671 33	−0.094 815 25
C	−0.365 262 57	−1.361 413 77	−0.654 562 05
H	−1.408 283 08	−1.657 820 39	−0.472 876 68
H	−0.155 020 06	−1.345 015 07	−1.729 733 53
H	2.906 538 26	−1.681 531 59	−0.033 970 17
H	2.094 826 80	0.884 466 81	0.068 596 50
H	−0.551 710 42	0.918 132 33	−0.223 844 12

Table A.34: EOM-CCSD/aug-cc-pVDZ geometry (Ångströms) of (1R,4R)-norbornenone, third excited state.

Atomic Symbol	X	Y	Z
C	−0.137 803 550 726	1.049 750 343 170	−0.440 502 558 433
C	1.323 044 760 978	0.943 961 588 290	−0.265 011 583 450
C	1.669 957 774 222	−0.385 482 392 054	−0.555 352 823 908
C	0.394 415 356 113	−1.159 627 485 953	−0.752 741 718 659
C	−0.329 923 183 176	−1.266 052 059 496	0.640 088 074 177
C	−0.741 628 149 476	0.209 728 414 283	0.861 634 396 834
O	−1.386 377 490 694	0.704 801 168 555	1.729 461 598 188
H	0.321 828 799 434	−1.567 888 961 577	1.476 497 685 834
H	−1.233 020 329 923	−1.896 800 661 503	0.636 961 131 756
H	0.508 929 988 154	−2.133 970 326 869	−1.250 057 029 807
C	−0.491 021 887 444	−0.096 298 574 806	−1.451 302 322 935
H	−1.569 193 765 571	−0.337 408 642 311	−1.462 294 869 244
H	−0.132 371 618 853	0.161 285 207 411	−2.459 595 629 365
H	2.677 938 862 410	−0.810 635 491 197	−0.611 460 744 454
H	1.971 727 457 479	1.751 145 123 081	0.080 583 466 086
H	−0.630 332 150 477	2.031 215 259 569	−0.483 095 037 001

Table A.35: B3LYP/aug-cc-pVDZ geometry (Ångströms) of (*S*,*S*)-*trans*-β-hydrindanone, ground state.

Atomic Symbol	X	Y	Z
C	−0.042 740 821 812	0.110 798 657 435	−0.772 752 521 666
C	−0.042 740 821 812	0.110 798 657 435	0.772 751 908 334
C	−0.042 740 821 812	−1.382 554 711 644	1.124 384 794 533
C	0.781 387 242 594	−2.025 660 694 589	0.000 000 493 311
C	0.960 136 429 765	−0.995 700 933 231	−1.124 385 721 307
H	0.830 348 154 891	−1.462 649 871 255	−2.108 373 540 072
H	1.996 781 962 742	−0.621 454 834 195	−1.071 227 751 781
O	1.217 576 427 036	−3.156 426 021 864	0.000 001 879 935
H	0.367 007 088 930	−1.641 379 984 891	2.108 373 872 694
H	−1.062 171 603 992	−1.801 427 697 152	1.071 223 005 955
C	−1.147 317 139 066	1.009 330 340 834	1.325 946 630 017
C	−0.984 969 472 230	2.436 497 862 664	0.768 900 667 223
C	−0.906 443 961 664	2.466 788 727 454	−0.768 900 984 598
C	0.172 276 443 068	1.518 355 311 202	−1.325 947 207 741
H	1.174 041 851 798	1.875 049 419 315	−1.032 948 994 725
H	0.144 324 565 547	1.517 655 811 213	−2.425 787 281 313
H	−0.718 029 206 088	3.494 940 548 795	−1.110 721 041 942
H	−1.884 364 208 757	2.173 799 436 657	−1.185 370 304 532
H	−1.815 041 178 438	3.071 775 078 388	1.110 720 884 857
H	−0.063 619 478 625	2.876 139 659 810	1.185 370 003 582
H	−2.129 116 676 830	0.600 876 946 957	1.032 948 223 198
H	−1.126 136 569 319	1.027 583 209 110	2.425 786 709 509
H	0.927 251 420 850	0.531 556 127 846	1.095 342 611 242
H	−1.044 020 424 932	−0.228 849 635 913	−1.095 343 110 818

Table A.36: B3LYP/aug-cc-pVDZ geometry (Ångströms) of (*S*,*S*)-*trans*-β-hydrindanone, first excited state.

Atomic Symbol	X	Y	Z
C	−0.023 419 831 207	0.114 930 994 800	−0.752 319 118 084
C	−0.023 419 831 207	0.114 930 994 800	0.783 544 941 916
C	−0.023 419 831 207	−1.381 644 893 422	1.134 033 521 128
C	0.934 736 482 204	−1.933 037 575 184	0.070 708 801 348
C	0.981 348 698 837	−0.986 069 639 650	−1.144 973 788 745
H	0.705 962 692 611	−1.510 589 038 970	−2.073 943 056 606
H	2.005 459 778 352	−0.599 171 954 977	−1.281 183 720 353
O	1.034 670 103 016	−3.211 491 347 147	−0.111 594 893 382
H	0.317 751 632 922	−1.611 974 005 530	2.152 764 268 211
H	−1.032 957 215 098	−1.824 318 887 535	1.010 312 799 245
C	−1.148 329 598 204	0.991 065 111 650	1.335 383 958 617
C	−0.989 101 479 479	2.423 169 636 785	0.784 931 806 655
C	−0.900 078 721 685	2.461 887 375 674	−0.751 064 768 245
C	0.189 471 147 887	1.523 858 820 255	−1.309 196 019 160
H	1.187 439 626 438	1.886 776 950 397	−1.013 179 833 933
H	0.161 083 608 854	1.523 244 238 121	−2.408 765 688 614
H	−0.712 376 523 279	3.492 737 200 194	−1.085 686 761 430
H	−1.873 078 437 562	2.166 840 722 150	−1.176 807 648 758
H	−1.828 000 459 534	3.048 785 213 544	1.123 458 518 509
H	−0.074 846 510 620	2.867 079 449 416	1.211 665 378 434
H	−2.122 873 143 941	0.577 356 436 687	1.028 660 912 943
H	−1.136 603 653 892	1.004 483 633 785	2.435 115 129 852
H	0.937 885 555 320	0.536 973 638 359	1.122 613 156 160
H	−1.022 634 259 384	−0.228 439 528 745	−1.072 450 073 041

Table A.37: B3LYP/aug-cc-pVDZ geometry (Ångströms) of *trans*-bicyclo[3.3.0]octane-3,7-dione, ground state.

Atomic Symbol	X	Y	Z
C	0.000 000 00	0.000 000 00	0.000 000 00
C	1.545 964 10	0.000 000 00	0.000 000 00
C	1.891 756 37	−1.487 569 47	0.000 000 00
C	0.772 982 09	−2.084 227 88	−0.887 051 38
C	−0.345 792 24	−1.031 307 72	−1.072 038 80
H	−0.252 451 85	−0.612 649 55	−2.087 761 93
H	−1.332 599 17	−1.501 852 46	−0.993 176 79
O	0.772 982 18	−3.196 805 95	−1.360 566 91
H	1.798 415 90	−1.929 316 32	1.005 896 51
H	2.878 563 31	−1.756 957 46	−0.393 778 70
C	1.891 756 40	1.031 307 74	1.072 038 82
C	0.772 982 17	2.084 227 99	0.887 051 18
C	−0.345 792 26	1.487 569 45	0.000 000 00
H	−1.332 599 18	1.756 957 43	0.393 778 74
H	−0.252 451 87	1.929 316 31	−1.005 896 54
O	0.772 982 39	3.196 806 31	1.360 566 08
H	2.878 563 36	1.501 852 46	0.993 176 90
H	1.798 415 91	0.612 649 50	2.087 761 89
H	1.865 661 58	0.414 232 63	−0.973 286 91
H	−0.319 697 49	−0.414 232 65	0.973 286 89

Table A.38: B3LYP/aug-cc-pVDZ geometry (Ångströms) of *trans*-bicyclo[3.3.0]octane-3,7-dione, first excited state.

Atomic Symbol	X	Y	Z
C	0.000 000 00	0.000 000 00	0.000 000 00
C	1.536 661 77	0.000 000 00	0.000 000 00
C	1.884 838 07	−1.486 759 97	0.000 000 00
C	0.764 895 70	−2.077 218 40	−0.895 742 59
C	−0.352 129 41	−1.018 899 88	−1.083 721 86
H	−0.245 849 73	−0.595 836 97	−2.096 295 20
H	−1.341 071 45	−1.486 294 08	−1.013 994 08
O	0.761 151 31	−3.188 790 91	−1.366 529 73
H	1.779 208 49	−1.936 997 91	1.000 674 52
H	2.872 888 64	−1.757 239 66	−0.389 663 37
C	1.875 521 28	1.006 069 46	1.102 298 60
C	0.814 569 43	2.090 406 05	0.798 381 91
C	−0.379 853 39	1.483 571 00	0.009 092 41
H	−1.336 590 62	1.694 044 76	0.509 306 35
H	−0.425 060 93	1.925 389 28	−1.000 234 76
O	0.595 735 48	3.033 147 86	1.654 745 61
H	2.892 159 21	1.418 563 61	1.064 930 92
H	1.716 214 88	0.577 412 08	2.111 434 11
H	1.874 234 75	0.428 776 61	−0.958 211 62
H	−0.318 190 79	−0.420 940 08	0.969 308 50

Table A.39: B3LYP/aug-cc-pVDZ geometry (Ångströms) of *trans*-bicyclo[3.3.0]octane-3,7-dione, second excited state.

Atomic Symbol	X	Y	Z
C	0.000 000 00	0.000 000 00	0.000 000 00
C	1.535 572 90	0.000 000 00	0.000 000 00
C	1.898 003 49	−1.487 567 16	0.000 000 00
C	0.767 787 30	−2.055 558 90	−0.883 457 98
C	−0.362 431 55	−1.023 692 19	−1.079 309 92
H	−0.314 546 17	−0.606 454 31	−2.101 447 03
H	−1.348 310 98	−1.493 470 45	−0.959 299 93
O	0.767 787 16	−3.201 353 76	−1.375 906 87
H	1.850 114 39	−1.942 055 38	1.006 127 13
H	2.883 884 31	−1.723 778 51	−0.423 433 08
C	1.898 004 75	1.023 693 27	1.079 308 69
C	0.767 787 96	2.055 561 43	0.883 453 50
C	−0.362 433 12	1.487 566 63	0.000 003 68
H	−1.348 311 34	1.723 775 80	0.423 443 89
H	−0.314 552 46	1.942 055 44	−1.006 123 58
O	0.767 788 36	3.201 356 18	1.375 902 43
H	2.883 885 25	1.493 469 46	0.959 299 61
H	1.850 116 75	0.606 457 09	2.101 446 41
H	1.859 872 32	0.416 523 54	−0.969 138 34
H	−0.324 298 34	−0.416 525 73	0.969 137 77

A.2 Adiabatic Excitation Energies

Table A.40: Adiabatic excitation energies (in eV) for (1*R*,4*R*)-norbornenone at the B3LYP/aug-cc-pVDZ geometries.

Transition	EOM-CCSD	B3LYP	CAM-B3LYP
1	3.78	3.62	3.80
2	5.01	4.80	5.33
3	5.40	5.30	5.88

Table A.41: Adiabatic excitation energies (in eV) for (*S*)-3-methylcyclopentanone at the B3LYP/aug-cc-pVDZ geometries.

Transition	EOM-CCSD	B3LYP	CAM-B3LYP
1	3.86	3.83	3.95
2	6.21	5.58	6.21

Table A.42: Adiabatic excitation energies (in eV) for (1*R*,4*R*)-α-fenchocampherone at the B3LYP/aug-cc-pVDZ geometries.

Transition	EOM-CCSD	B3LYP	CAM-B3LYP
1	3.82	3.79	3.91
2	6.18	5.45	6.21
3	6.66	5.88	6.68

Table A.43: Adiabatic excitation energies (in eV) for (1*R*,5*S*)-*cis*-β-hydrindanone at the B3LYP/aug-cc-pVDZ geometries.

Transition	EOM-CCSD	B3LYP	CAM-B3LYP
1	3.85	3.82	3.95
2	6.21	5.52	6.22
3	6.62	5.86	6.61

Table A.44: Adiabatic excitation energies (in eV) for (*S*,*S*)-*trans*-β-hydrindanone at the B3LYP/aug-cc-pVDZ geometries.

Transition	EOM-CCSD	B3LYP	CAM-B3LYP
1	3.85	3.82	3.95

Table A.45: Adiabatic excitation energies (in eV) for (1*R*)-7-methylenebicyclo[2.2.1]heptan-2-one at the B3LYP/aug-cc-pVDZ geometries.

Transition	EOM-CCSD	B3LYP	CAM-B3LYP
1 (E1)	3.83	3.76	3.90
1 (E2)	3.88	3.79	3.94
2	6.51	4.91	5.92

Table A.46: Adiabatic excitation energies (in eV) for (1*S*)-2-methylenebicyclo[2.2.1]heptan-7-one at the B3LYP/aug-cc-pVDZ geometries.

Transition	EOM-CCSD	B3LYP	CAM-B3LYP
1 (E1)	3.74	3.50	3.73
1 (E2)	3.68	3.56	3.71
2	6.01	4.44	5.43

Table A.47: Adiabatic excitation energies (in eV) for *trans*-bicyclo[3.3.0]octane-3,7-dione at the B3LYP/aug-cc-pVDZ geometries.

Transition	EOM-CCSD	B3LYP	CAM-B3LYP
1	3.86	3.82	3.96
2	4.12	4.06	4.17

A.3 Velocity-gauge Transition Strengths and Dissymmetry Factors

Table A.48: Electronic transition data for the ground and first three excited states of (1*R*,4*R*)-norbornenone obtained using EOM-CCSD, B3LYP, and CAM-B3LYP with the aug-cc-pVDZ basis set. Reported rotational strengths were obtained using the velocity representation of the electric dipole operator.

Method	Transition	Energy (eV)	RS (10^{-40} cgs)	DS (10^{-40} cgs)	g (10^{-3} cgs)
EOM-CCSD	G →1	4.29	22.22	713.0	124.7
B3LYP	G →1	4.03	55.98	4248	52.72
CAM-B3LYP	G →1	4.18	43.71	2467	70.89
EOM-CCSD	G ←1	2.94	13.79	1102	50.07
B3LYP	G ←1	2.74	30.53	4048	30.17
CAM-B3LYP	G ←1	2.86	26.24	2916	35.99
EOM-CCSD	G →2	6.00	-12.58	395.9	-127.1
B3LYP	G →2	5.27	-0.1498	2315	-0.2588
CAM-B3LYP	G →2	5.87	11.67	14290	3.267
EOM-CCSD	G ←2	4.93	26.64	4175	25.53
B3LYP	G ←2	4.09	21.80	14110	6.180
CAM-B3LYP	G ←2	4.55	34.86	22150	6.296
EOM-CCSD	G →3	6.33	30.34	15100.	8.038
B3LYP	G →3	5.51	-3.077	7074	-1.740
CAM-B3LYP	G →3	6.09	-12.48	1921	-2.599
EOM-CCSD	G ←3	5.76	21.05	13030	6.464
B3LYP	G ←3	5.06	-7.010	9236	-3.036
CAM-B3LYP	G ←3	5.61	-16.72	10330	-6.475

Table A.49: Electronic transition data for the ground and first two excited states of (*S*)-3-methylcyclopentanone obtained using EOM-CCSD, B3LYP, and CAM-B3LYP with the aug-cc-pVDZ basis set. Reported rotational strengths were obtained using the velocity representation of the electric dipole operator.

Method	Transition	Energy (eV)	RS (10^{-40} cgs)	DS (10^{-40} cgs)	g_x (10^{-3} cgs)
EOM-CCSD	G $\rightarrow$ 1	4.28	-7.009	48.86	-573.8
B3LYP	G $\rightarrow$ 1	4.15	-11.11	112.7	-394.4
CAM-B3LYP	G $\rightarrow$ 1	4.23	-8.480	62.91	-539.2
EOM-CCSD	G $\leftarrow$ 1	3.21	-6.820	798.8	-34.15
B3LYP	G $\leftarrow$ 1	3.14	-9.389	896.8	-41.88
CAM-B3LYP	G $\leftarrow$ 1	3.23	-7.728	918.9	-33.64
EOM-CCSD	G $\rightarrow$ 2	6.32	8.953	9891	3.620
B3LYP	G $\rightarrow$ 2	5.66	12.02	8159	5.893
CAM-B3LYP	G $\rightarrow$ 2	6.33	10.15	9802	4.143
EOM-CCSD	G $\leftarrow$ 2	6.11	8.5588	9196	3.723
B3LYP	G $\leftarrow$ 2	5.48	13.28	8204	6.474
CAM-B3LYP	G $\leftarrow$ 2	6.12	9.915	9057	4.379

Table A.50: Electronic transition data for the ground and first three excited states of (1*R*,4*R*)-α-fenchocampherone obtained using EOM-CCSD, B3LYP, and CAM-B3LYP with the aug-cc-pVDZ basis set. Reported rotational strengths were obtained using the velocity representation of the electric dipole operator.

Method	Transition	Energy (eV)	RS (10^{-40} cgs)	DS (10^{-40} cgs)	g_x (10^{-3} cgs)
EOM-CCSD	G $\rightarrow$1	4.31	4.419	87.80	201.3
B3LYP	G $\rightarrow$1	4.17	7.236	190.1	152.2
CAM-B3LYP	G $\rightarrow$1	4.26	5.249	127.6	164.6
EOM-CCSD	G $\leftarrow$1	3.04	-3.493	703.4	-19.86
B3LYP	G $\leftarrow$1	2.96	2.181	1308	6.668
CAM-B3LYP	G $\leftarrow$1	3.03	1.344	1303	4.127
EOM-CCSD	G $\rightarrow$2	6.32	6.501	8131	3.198
B3LYP	G $\rightarrow$2	5.57	-4.414	3993	-4.421
CAM-B3LYP	G $\rightarrow$2	6.36	6.048	7328	3.301
EOM-CCSD	G $\leftarrow$2	6.01	5.940	8220.	2.891
B3LYP	G $\leftarrow$2	5.30	-5.416	4863	-4.455
CAM-B3LYP	G $\leftarrow$2	6.06	5.615	7401	3.035
EOM-CCSD	G $\rightarrow$3	6.82	-0.1332	712.9	-0.7474
B3LYP	G $\rightarrow$3	6.00	1.690	785.8	8.604
CAM-B3LYP	G $\rightarrow$3	6.84	0.4995	876.8	2.279
EOM-CCSD	G $\leftarrow$3	6.48	0.04157	1211	0.1373
B3LYP	G $\leftarrow$3	5.72	2.180	986.8	8.837
CAM-B3LYP	G $\leftarrow$3	6.52	0.8691	1164	2.988

Table A.51: Electronic transition data for the ground and first three excited states of (1*R*,5*S*)-*cis*-β-hydrindanone obtained using EOM-CCSD, B3LYP, and CAM-B3LYP with the aug-cc-pVDZ basis set. Reported rotational strengths were obtained using the velocity representation of the electric dipole operator.

Method	Transition	Energy (eV)	RS (10^{-40} cgs)	DS (10^{-40} cgs)	g_x (10^{-3} cgs)
EOM-CCSD	G $\rightarrow$1	4.26	6.544	68.20	383.8
B3LYP	G $\rightarrow$1	4.14	11.38	136.0	334.7
CAM-B3LYP	G $\rightarrow$1	4.22	8.252	75.27	438.5
EOM-CCSD	G $\leftarrow$1	3.23	6.623	715.3	37.04
B3LYP	G $\leftarrow$1	3.17	9.307	848.5	43.88
CAM-B3LYP	G $\leftarrow$1	3.25	7.702	808.7	38.09
EOM-CCSD	G $\rightarrow$2	6.32	0.01386	8955	0.006191
B3LYP	G $\rightarrow$2	5.61	-4.156	5364	-3.099
CAM-B3LYP	G $\rightarrow$2	6.34	0.1944	8520.	0.09127
EOM-CCSD	G $\leftarrow$2	6.09	0.1444	8022	0.07202
B3LYP	G $\leftarrow$2	5.41	-5.404	5195	-4.161
CAM-B3LYP	G $\leftarrow$2	6.11	-0.08290	7566	-0.04383
EOM-CCSD	G $\rightarrow$3	6.78	6.941	3152	8.808
B3LYP	G $\rightarrow$3	5.98	6.180	3135	7.885
CAM-B3LYP	G $\rightarrow$3	6.77	6.846	3585	7.640
EOM-CCSD	G $\leftarrow$ 3	6.48	5.751	3049	7.545
B3LYP	G $\leftarrow$ 3	5.72	8.879	4454	7.974
CAM-B3LYP	G $\leftarrow$ 3	6.49	6.428	3812	6.746

Table A.52: Electronic transition data for the ground and first excited state of (*S*,*S*)-*trans*-β-hydrindanone obtained using EOM-CCSD, B3LYP, and CAM-B3LYP with the aug-cc-pVDZ basis set. Reported rotational strengths were obtained using the velocity representation of the electric dipole operator.

Method	Transition	Energy (eV)	RS (10^{-40} cgs)	DS (10^{-40} cgs)	g_x (10^{-3} cgs)
EOM-CCSD	G $\rightarrow$1	4.27	9.906	88.41	448.2
B3LYP	G $\rightarrow$1	4.14	15.11	201.3	300.3
CAM-B3LYP	G $\rightarrow$1	4.23	11.66	113.2	412.0
EOM-CCSD	G $\leftarrow$1	3.20	6.746	684.9	39.40
B3LYP	G $\leftarrow$1	3.13	10.86	951.7	45.63
CAM-B3LYP	G $\leftarrow$1	3.21	8.513	878.6	38.76

Table A.53: Electronic transition data for the ground and first two excited states of *trans*-bicyclo[3.3.0]octane-3,7-dione obtained using EOM-CCSD, B3LYP, and CAM-B3LYP with the aug-cc-pVDZ basis set. Reported rotational strengths were obtained using the velocity representation of the electric dipole operator.

Method	Transition	Energy (eV)	RS (10^{-40} cgs)	DS (10^{-40} cgs)	g_x (10^{-3} cgs)
EOM-CCSD	G $\rightarrow$1	4.26	—	300.5	—
B3LYP	G $\rightarrow$1	4.07	—	955.4	—
CAM-B3LYP	G $\rightarrow$1	4.20	—	396.8	—
EOM-CCSD	G $\leftarrow$1	3.23	-8.316	648.0	-51.34
B3LYP	G $\leftarrow$1	3.14	-16.63	1087	-61.16
CAM-B3LYP	G $\leftarrow$1	3.24	-10.79	927.5	-46.54
EOM-CCSD	G $\rightarrow$2	4.31	—	—	—
B3LYP	G $\rightarrow$2	4.19	—	—	—
CAM-B3LYP	G $\rightarrow$2	4.26	—	—	—
EOM-CCSD	G $\leftarrow$2	4.02	—	—	—
B3LYP	G $\leftarrow$2	3.92	—	—	—
CAM-B3LYP	G $\leftarrow$2	4.00	—	—	—

Table A.54: Electronic transition data for the ground and first two excited states of (1R)-7-methylenebicyclo[2.2.1]heptan-2-one obtained using EOM-CCSD, B3LYP, and CAM-B3LYP with the aug-cc-pVDZ basis set. Reported rotational strengths were obtained using the velocity representation of the electric dipole operator.

Method	Transition	Energy (eV)	RS (10^{-40} cgs)	DS (10^{-40} cgs)	g_x (10^{-3} cgs)
EOM-CCSD	G $\rightarrow$1	4.31	12.68	752.1	67.43
B3LYP	G $\rightarrow$1	4.13	29.29	2788	42.02
CAM-B3LYP	G $\rightarrow$1	4.24	21.30	1459	58.42
EOM-CCSD	G $\leftarrow$1 (E1)	2.99	2.021	740.1	10.92
B3LYP	G $\leftarrow$1 (E1)	2.87	17.49	1394	50.17
CAM-B3LYP	G $\leftarrow$1 (E1)	2.96	12.08	1338	36.11
EOM-CCSD	G $\leftarrow$1 (E2)	3.01	-0.1513	1429	-0.4236
B3LYP	G $\leftarrow$1 (E2)	2.88	-0.8213	4356	-0.7543
CAM-B3LYP	G $\leftarrow$1 (E2)	2.97	-1.920	3313	-2.319
EOM-CCSD	G $\rightarrow$2	6.25	-39.04	4648	-33.59
B3LYP	G $\rightarrow$2	5.59	-22.33	3918	-22.80
CAM-B3LYP	G $\rightarrow$2	6.25	-49.30	7211	-27.35
EOM-CCSD	G $\leftarrow$2	5.14	6.454	694.4	37.18
B3LYP	G $\leftarrow$2	3.49	1.909	451.3	16.92
CAM-B3LYP	G $\leftarrow$2	4.41	5.496	894.7	24.57

Table A.55: Electronic transition data for the ground and first two excited states of (1*S*)-2-methylenebicyclo[2.2.1]heptan-7-one obtained using EOM-CCSD, B3LYP, and CAM-B3LYP with the aug-cc-pVDZ basis set. Reported rotational strengths were obtained using the velocity representation of the electric dipole operator.

Method	Transition	Energy (eV)	RS (10^{-40} cgs)	DS (10^{-40} cgs)	g_x (10^{-3} cgs)
EOM-CCSD	G $\rightarrow$1	4.34	-10.80	617.5	-69.98
B3LYP	G $\rightarrow$1	4.10	-25.89	2963	-34.95
CAM-B3LYP	G $\rightarrow$1	4.23	-18.55	1383	-53.67
EOM-CCSD	G $\leftarrow$1 (E1)	2.42	2.109	378.6	22.28
B3LYP	G $\leftarrow$1 (E1)	2.15	-13.51	1561	-34.62
CAM-B3LYP	G $\leftarrow$1 (E1)	2.30	-9.560	1844	-20.74
EOM-CCSD	G $\leftarrow$1 (E2)	2.60	4.022	1229	13.09
B3LYP	G $\leftarrow$1 (E2)	2.43	2.445	4451	2.197
CAM-B3LYP	G $\leftarrow$1 (E2)	2.52	3.149	3589	3.508
EOM-CCSD	G $\rightarrow$2	6.10	28.94	7769	14.90
B3LYP	G $\rightarrow$2	5.45	25.20	7342	13.73
CAM-B3LYP	G $\rightarrow$2	6.07	57.25	3.650×10^4	6.274
EOM-CCSD	G $\leftarrow$2	4.55	0.3311	262.7	5.042
B3LYP	G $\leftarrow$2	2.89	-11.68	905.3	-51.62
CAM-B3LYP	G $\leftarrow$2	3.82	-0.9734	751.5	-5.181